

ROBOTIC METHODS FOR INSTALLING BATT INSULATION INTO WOOD-FRAME  
WALL PANELS IN BUILDING PREFABRICATION

by  
Xiao Han

A thesis submitted in partial fulfillment of the requirements for the degree of  
Master of Science  
in  
Civil (Cross-disciplinary)

Department of Civil and Environmental Engineering  
University of Alberta

© Xiao Han, 2024

## **Abstract**

In the light-frame building prefabrication construction industry, the utilization of robot arms is increasingly trending. In exterior wood-frame wall panels, which contain components such as wood frame, insulation and sheathing, automation has streamlined the construction of structural elements. In building construction, batt thermal insulation is extensively used due to its cost-effectiveness in achieving high thermal resistance. However, the automation of batt insulation installation in prefabricated building construction remains underdeveloped due to its deformable characteristics and currently relies solely on manual methods, which expose workers to various health risks. This thesis introduces two novel robotic methods, V-GLITPP and H-GLPPR, designed to automate the installation of batt thermal insulation into wood-frame wall frames without requiring complex modeling and simulation of its actual deformation. These methods ensure a tight fit within the frame cavity, eliminating visible gaps and deficiencies that could compromise thermal resistance.

Each method utilizes a single 6-degree-of-freedom robot arm and a custom-built end-effector and is carefully engineered to overcome the non-linear and non-rigid mechanical characteristics of batt insulation during installation, which poses major challenges in robotic manipulation. Furthermore, both methods incorporate collision avoidance to prevent any potential collisions.

The V-GLITPP method was initially developed under hardware constraints, with the goal of minimizing costs and utilizing existing equipment that was available in our lab. This method was tested on a scaled wood frame to demonstrate the feasibility of robotic insulation installation and employed a vertical pickup strategy with six major steps: (1) Grasp, (2) Lift, (3) Insert, (4) Tilt, (5) Push, and (6) Press. The necessary physical operating parameters for the insertion process,

such as angles, offset, and force requirements, were identified to ensure the precision, efficiency, and repeatability of insertion. A prototype of the designed end-effector was used to demonstrate and validate the robotic method, which achieved a high success rate of 93.3%. Given its success in the scaled setup, the method faced several challenges when scaled up to full-size frames, thus leading to the second robotic method.

The H-GLPPR method was developed for full size implementation and employed a horizontal pickup strategy through five key steps: (1) Grasp, (2) Lift, (3) Place, (4) Press and (5) Roll. The main operational parameters such as grasp location, clearances, angle, and displacements were identified and tuned to ensure repeatability, accuracy, and reliability of the installation process. Within our trials, the prototype end-effector, incorporating larger stroke dual parallel grippers and a roller, demonstrated a high success rate of 92.5%. Hence, demonstrating the effectiveness of the H-GLPPR for installation of batt insulation into full-size frames.

The development of our V-GLITPP and H-GLPPR methods not only facilitates the expansion of the thermal insulation options available during automated prefabrication but also improves efficiency and safety for workers by reducing labor intensity. By filling a significant gap in the current construction practices, our methods facilitate ways toward the complete automation of wood-frame wall panel prefabrication.

## Preface

- Chapter 2 of this thesis has been published as Xiao Han, Cheng-Hsuan Yang, Alejandra Hernandez Sanchez, and Yuxiang Chen, “A ROBOTIC METHOD TO INSERT BATT INSULATION INTO LIGHT - FRAME WOOD WALL FOR PANEL PREFABRICATIONS”. CONVR 2023 - Proceedings of the 23rd International Conference on Construction Applications of Virtual Reality, Florence, Italy. <https://doi.org/10.36253/979-12-215-0289-3.58>
- Chapter 3 of this thesis will be submitted as Xiao Han, Cheng-Hsuan Yang, and Yuxiang Chen, “RIMBI: Robotic Installation Method for Batt Insulation” to journal Automation in Construction.
- Appendix A and B of this thesis (original work by Xiao Han) were included in RoBIM Technology Progress Reports which has been submitted to Alberta Innovates to demonstrate project progress.

We advise readers that this thesis presents dimensional data in both metric and imperial units to accommodate the diverse standards applicable to the equipment and materials described. For instance, the robotic equipment is manufactured in European countries, which utilizes metric units. Meanwhile, timber and insulation materials in North America utilize imperial units. Therefore, all the dimensions have been converted and are reported in both measurement systems throughout this thesis.

## **Acknowledgements**

First, I would like to express my sincere thanks and gratitude to my supervisor, Dr. Yuxiang Chen, who introduced me to the fields of building science and robotic in construction. His consistent support, guidance and time throughout my research have been invaluable. Working under his mentorship was a profoundly influential experience. His commitment to his students and dedication to research have influenced both my academic journey and my future career in engineering.

Furthermore, I am deeply grateful to Cheng-Hsuan Yang for expanding my knowledge of robotic in construction and for the many hours he spent engaging in valuable discussions and providing suggestions. The research would not have gone smoothly without his kind help.

I wish extend my thanks to all the group members of the IDOBE lab for their encouragement and friendship; it was a pleasure to have shared this academic journey together.

Additionally, I would like to acknowledge the financial and in-kind support from our industrial project partner RoBIM Technologies Inc. through a Mitacs project (IT32540) titled Design of Prefabricated Exterior Wall Panels for Robotic Building Retrofit.

Last but not the least, words cannot fully express my appreciation to my dear parents and my beloved husband for their unwavering support and love. Special thanks to my father for manufacturing the machinery hardware, and to my husband, Jiang Lin Li, for his invaluable help with everything.

# Contents

Abstract.....	ii
Preface.....	iv
Acknowledgements.....	v
Contents .....	vi
List of Figures.....	ix
List of Tables .....	xiii
Chapter 1 : Introduction.....	1
1.1 Background and Literature Survey .....	2
1.1.1 Prefabrication for Wood-frame Wall Panels .....	2
1.1.2 Techniques for Handling Deformable Objects.....	4
1.2 Research Objectives and Scope.....	6
1.3 Thesis Outline .....	7
Chapter 2 : Vertical Pickup Strategy .....	8
2.1 Methodology .....	8
2.1.1 In-lab Robotic Cell Setup.....	9
2.1.2 End-Effector Design.....	10
2.1.3 End-effector Prototype .....	11
2.1.4 Installation Process.....	13
2.1.5 Parameter Results .....	15
2.1.5.1 Insertion angle ( $\alpha$ ) & Insertion offset ( $d$ ) & Tilt angle ( $\theta$ ).....	15
2.1.5.2 Press spacing ( $s$ ).....	18
2.1.5.3 Pressing force ( <b><math>F_{Press}</math></b> ) .....	19
2.1.6 Robot Simulation and Control.....	19
2.2 Validation .....	20
2.2.1 Overview .....	21
2.2.2 Results and Discussion.....	21
2.3 Chapter Conclusion.....	26
Chapter 3 : Horizontal Pickup Strategy .....	27
3.1 Methodology .....	27

3.1.1 Installation Process .....	28
3.1.2 End-Effector Design .....	30
3.1.3 In-lab Robotic Cell Setup .....	32
3.1.4 End-effector Prototype .....	33
3.1.5 Parameter Results .....	35
3.1.5.1 Grasp location ( $\mathbf{xg}$ ) .....	36
3.1.5.2 Gripper closure ( $lc$ ) .....	37
3.1.5.3 Clearance ( $\mathbf{c}$ ) .....	38
3.1.5.4 Rolling depth ( $\mathbf{dr}$ ) .....	39
3.1.5.5 Pressing depth ( $\mathbf{dp}$ ) and Tilt angle ( $\varphi$ ) .....	40
3.1.5.6 Pressing interval ( $\mathbf{i}$ ) .....	41
3.1.6 Robot Simulation and Control .....	41
3.2 Validation .....	48
3.2.1 Overview .....	48
3.2.2 Results and Discussion .....	51
3.3 Chapter Conclusion .....	55
Chapter 4 : Conclusion and Future Work .....	57
4.1 Conclusion .....	57
4.2 Future Work .....	58
Bibliography .....	60
Appendix A .....	68
Appendix B .....	71
B.1 Case Study - NRCan PEER Project .....	71
B.1.1 PEER Wall – 2x4 Framed Panel Wall System .....	71
B.1.2 PEER Wall – I-Joist Framed Panel Wall System .....	73
B.1.3 Section Summary .....	75
B.2 Building Codes .....	75
B.3 Proposed Light-frame Panel Thermal Analysis .....	77
B.3.1 Clear Field Thermal Performance .....	77
B.3.2 Thermal Bridges .....	79
B.3.3 Effective Thermal Performance of Proposed Panel .....	81

B.3.4 Dew Point of Proposed Panel .....	81
Appendix C .....	82
Appendix D.....	86

## List of Figures

Figure 1.1: Building prefabrication process.....	3
Figure 2.1: Overview of proposed methodology for vertical pickup configuration.....	9
Figure 2.2: The in-lab robotic cell setup.....	10
Figure 2.3: The proposed robotic end-effector in open and close positions.....	11
Figure 2.4: The prototyped robotic end-effector at fully open position (left) and at fully closed position (right) .....	12
Figure 2.5: The V-GLITPP insertion process.....	13
Figure 2.6: Illustration of the variables in Eq.1 .....	16
Figure 2.7: Combination of insertion angle and insertion offset .....	18
Figure 2.8: Simulation environment in RoBIM software .....	20
Figure 2.9: Two scenarios.....	21
Figure 2.10: V-GLITPP process for Scenario 1 with mineral wool insulation (Grasp, Lift, Insert, Tilt, Push, Press, front and back completion views).....	23
Figure 2.11: V-GLITPP process for Scenario 2.1 with fiberglass insulation (Grasp, Lift, Insert, Tilt, Push, Press, front and back completion views).....	24
Figure 2.12: V-GLITPP process for Scenario 2.2 with fiberglass insulation (Grasp, Lift, Insert, Tilt, Push, Press, front and back completion views).....	25
Figure 3.1: Overview of proposed methodology for horizontal pickup configuration.....	28
Figure 3.2: H-GLPPR process .....	30
Figure 3.3: End-effector design in isometric, top, side, front views.....	32
Figure 3.4: In-lab robotic cell setup.....	33
Figure 3.5: End-effector prototype .....	34
Figure 3.6: Overhanging beam with uniform load and symmetrical end supports.....	37
Figure 3.7: RoboDK robotic cell setup in isometric view (1 <sup>st</sup> ) and top view (2 <sup>nd</sup> ).....	42
Figure 3.8: Three scenarios.....	50
Figure 3.9: H-GLPPR process and completion with 15 x 5.5-inch (381 x 140 mm) fiberglass insulation size for Scenario 1 (Grasp 1st piece, Lift 1st piece, Place 1st piece, Press, Roll, Completion) .....	53

Figure 3.10: H-GLPPR process and completion with 15 x 3.5-inch (381 x 89 mm) mineral wool insulation size for Scenario 2 (Grasp 1st piece, Lift 1st piece, Place 1st piece, Grasp 2nd piece, Lift 2nd piece, Place 2nd piece, Press, Roll, Completion) .....	54
Figure 3.11: H-GLPPR process and completion after modifying the lifting speed with 23 x 3.5-inch (584 x 89 mm) fiberglass insulation size for Scenario 3 (Grasp 1 <sup>st</sup> piece, Lift 1 <sup>st</sup> piece, Place 1 <sup>st</sup> piece, Grasp 2 <sup>nd</sup> piece, Lift 2 <sup>nd</sup> piece, Place 2 <sup>nd</sup> piece, Grasp 3 <sup>rd</sup> piece, Lift 3 <sup>rd</sup> piece, Place 3 <sup>rd</sup> piece, Press, Roll, Completion).....	55
Figure B.1: Exploded view of partial retrofit light-framed panel components at floor line transition .....	72
Figure B.2: Exploded view of partial retrofit I-joint framed panel components at floor line transition .....	74
Figure B.3: Left: 3D modeling - Heat flux output of CW; Right: 3D modeling – Temperature output of CW.....	78
Figure B.4: Left: 3D modeling - Heat flux output of Expanding foam; Right: 3D modeling – Temperature output of Expanding foam .....	79
Figure B.5: Left: 3D modeling - Heat flux output of mid-level; Middle: 3D modeling – Temperature output of mid-level; Right: 3D modeling – Temperature output of Upper Bracket Detail view .....	80
Figure B.6: Left: 3D modeling - Heat flux output of bottom-level; Middle: 3D modeling – Temperature output of bottom-level; Right: 3D modeling – Temperature output of Bottom Bracket Detail view.....	81
Figure B.7: Illustration of dew point locations on the mid-level panel .....	81
Figure C.1: V-GLITPP process for Scenario 1 with fiberglass insulation .....	83
Figure C.2: V-GLITPP process for Scenario 2.1 with mineral wool insulation.....	84
Figure C.3: V-GLITPP process for Scenario 2.2 with mineral wool insulation.....	85
Figure D.1: H-GLPPR process for Scenario 1 with 15 x 3.5-inch (381 x 89 mm) fiberglass insulation.....	87
Figure D.2: H-GLPPR process for Scenario 2 with 15 x 3.5-inch (381 x 89 mm) fiberglass insulation.....	88
Figure D.3: H-GLPPR process for Scenario 3 with 15 x 3.5-inch (381 x 89 mm) fiberglass insulation.....	90

Figure D.4: H-GLPPR process for Scenario 1 with 15 x 3.5-inch (381 x 89 mm) mineral wool insulation.....	90
Figure D.5: H-GLPPR process for Scenario 3 with 15 x 3.5-inch (381 x 89 mm) mineral wool insulation.....	92
Figure D.6: H-GLPPR process for Scenario 1 with 23 x 3.5-inch (584 x 89 mm) fiberglass insulation.....	92
Figure D.7: H-GLPPR process for Scenario 2 with 23 x 3.5-inch (584 x 89 mm) fiberglass insulation.....	94
Figure D.8: H-GLPPR process for Scenario 1 with 23 x 3.5-inch (584 x 89 mm) mineral wool insulation.....	94
Figure D.9: H-GLPPR process for Scenario 2 with 23 x 3.5-inch (584 x 89 mm) mineral wool insulation.....	95
Figure D.10: H-GLPPR process for Scenario 3 with 23 x 3.5-inch (584 x 89 mm) mineral wool insulation.....	97
Figure D.11: H-GLPPR process for Scenario 2 with 15 x 5.5-inch (381 x 140 mm) fiberglass insulation.....	98
Figure D.12: H-GLPPR process for Scenario 3 with 15 x 5.5-inch (381 x 140 mm) fiberglass insulation.....	99
Figure D.13: H-GLPPR process for Scenario 1 with 15 x 5.5-inch (381 x 140 mm) mineral wool insulation.....	100
Figure D.14: H-GLPPR process for Scenario 2 with 15 x 5.5-inch (381 x 140 mm) mineral wool insulation.....	101
Figure D.15: H-GLPPR process for Scenario 3 with 15 x 5.5-inch (381 x 140 mm) mineral wool insulation.....	103
Figure D.16: H-GLPPR process for Scenario 1 with 23 x 5.5-inch (584 x 140 mm) fiberglass insulation.....	103
Figure D.17: H-GLPPR process for Scenario 2 with 23 x 5.5-inch (584 x 140 mm) fiberglass insulation.....	105
Figure D.18: H-GLPPR process for Scenario 3 with 23 x 5.5-inch (584 x 140 mm) fiberglass insulation.....	106

Figure D.19: H-GLPPR process for Scenario 1 with 23 x 5.5-inch (584 x 140 mm) mineral wool insulation..... 107

Figure D.20: H-GLPPR process for Scenario 2 with 23 x 5.5-inch (584 x 140 mm) mineral wool insulation..... 108

Figure D.21: H-GLPPR process for Scenario 3 with 23 x 5.5-inch (584 x 140 mm) fiberglass insulation..... 109

## List of Tables

Table 2.1: Specifications of the end-effector prototype.....	12
Table 2.2: Six steps of the V-GLITPP insertion process.....	14
Table 2.3: A list of trialed tilt angles with success rate .....	17
Table 2.4: A list of trialed combination of insertion angle and insertion offset with success rate	18
Table 2.5: A list of trialed press spacing with success rate .....	19
Table 2.6: A list of trialed pressing force with success rate .....	19
Table 2.7: Summarized selected parameter values obtained from Subsection 2.1.5.....	20
Table 2.8: Experiment results for entire V-GLITPP insertion process.....	22
Table 3.1: Specifications of the end-effector prototype.....	34
Table 3.2: Grasp location validation with success rate.....	37
Table 3.3: Gripper closure for various insulation types and sizes .....	38
Table 3.3: A list of trialed top-bottom clearance with success rate .....	39
Table 3.5: A list of trialed side clearance with success rate .....	39
Table 3.6: A list of trialed rolling depth with success rate .....	40
Table 3.7: A list of trialed combination of pressing depth and tile angle.....	40
Table 3.8: A list of trialed pressing interval with success rate .....	41
Table 3.9: A list of obtained parameter results.....	48
Table 3.10: Specification of wall frames .....	50
Table 3.11: Insulation length for each scenario .....	51
Table 3.12: Experiment results for entire H-GLPPR process.....	51

## **Chapter 1 : Introduction**

In the competitive industry of light-frame wood building construction, off-site prefabrication has emerged as an efficient process compared to on-site stick-built. Prefabrication is characterized as the assembly of building components such as wood frame, sheathing and insulation into a panelized or modularized system within a factory setting and subsequently transported on-site for installation [1]. This method has demonstrated remarkable potential in reducing construction time [2], errors [3], and waste [4], thereby minimizing overall project costs [5]. The hallmarks of prefabrication are its ability to facilitate construction within a controlled and purpose-built manufacturing environment; streamline high-volume production through specialized machinery and standardized processes; and offer better support to workers' health and safety through reduced workplace uncertainties and hazards [6,7].

In countries like Canada, United States, and Australia, light-frame construction is the dominant method for residential housing and various other buildings types [8]. However, current prefabrication processes still rely heavily on skilled-labour, making operations strongly dependent on the labour market, worker's skill level and physical conditions [2]. According to Statistics Canada [9], at the time of writing, there is a persistent skilled-labour shortage within the building construction industry in Canada. These factors limit scalability and productivity in response to growing construction demands [10].

The integration of automation technologies, particularly robot arms, offers a promising solution to these challenges and is capable of adapting to the demand for faster and higher-quality construction [11–13]. Robotic arms support mass production by efficiently performing repetitive tasks and adapting to production demands through scalable operations [14]. They also provide a flexible approach to automating work steps, capable of absorbing production delays and adapting to various tasks through quick end-effector changes [15]. Their implementation in prefabrication settings has resulted in increased production efficiency by 15%, production speed up by 38%, and reduce waste by 30%, according to [16].

In prefabrication, assembling structural components such as wood frame and sheathing have already been streamlined through automation solutions [17,18]. However, the automation of insulation installation processes remains underdeveloped. Insulation is a crucial component in enhancing occupant comfort and improving building energy performance by reducing heat

transfer through building envelopes. Common commercial insulation options in light-frame wood construction include blow-in, spray foam and batt thermal insulation [19]. Among these, batt thermal insulation is particularly favoured for its cost-effectiveness in achieving and maintaining high thermal resistance [20]. While established automated solutions already exist for blow-in and spray foam insulations, a viable automated method for installing batt insulation into light-frame wood wall panels, which will be referred as wood-frame wall panels in this thesis, remains notably absent. This represents a significant gap in the field of automated prefabrication. The primary challenges in this regards stem from the deformable characteristics of batt insulation and the need to achieve a tight fit within frame cavities without any imperfections.

Inspired by this gap, this research aims to develop a novel robotic method for installing batt thermal insulation into prefabricated wood-frame wall panels. This method is designed to leverage the precision, efficiency and flexibility of robotic arms and be compatible with existing prefabrication processes for seamless integration and minimal initial investments. Furthermore, automating batt installation not only enhances efficiency but also significantly improves worker health and safety. For the latter, this is accomplished by eliminating the risks of developing chronic respiratory diseases from exposure to airborne dust and fibers, carcinogens, and volatile organic compounds [21,22], and mitigating ergonomic injuries associated with repetitive motions during manual insulation installation [23].

## **1.1 Background and Literature Survey**

This section presents a literature survey that outlines current automated solutions for prefabricated panel production lines. The survey also reviews existing methods for simulating and handling deformable objects and exploring their applicability to batt insulation. The survey highlights the complexity and limitations of current technologies, including modelling methods and commonly used grippers. These findings underscore the need for developing a novel robotic process and a custom-built end-effector tailored specifically for the automated installation of batt insulation to wood-frame wall panels.

### **1.1.1 Prefabrication for Wood-frame Wall Panels**

Each prefabricated wall manufacturer [7,24,25], possesses proprietary processes based on their own unique operational setup, material selection, and desired production volume.

Generally, prefabrication operations for wood-frame wall panels can be described by the stages illustrated in Figure 1.1. The first stage involves designing and defining the specifications and dimension of the wall panel to be prefabricated, typically via architectural drawings and CAD models. Subsequently, raw building materials are cut, shaped, and processed to the required sizes and quantities in batches or on-demand. The cut-to-size studs and sheathings are then joined through nailing to construct the basic structural system of the wall panel, forming a canvas to support additional building elements. Insulation, whether blow-in, spray foam, or batt insulation, is installed into the wall panels. Finally, windows, doors, and building wraps are incorporated as dictated by design and building codes. At the end of the production line, the completed wall panels are stored and await transport to the construction site.

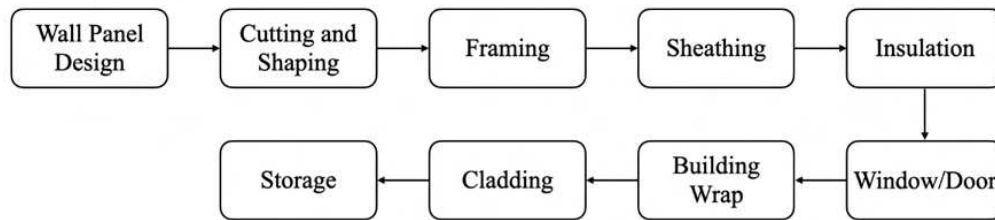


*Figure 1.1: Building prefabrication process*

Various automated industrial solutions currently exist to support the aforementioned prefabrication process [17,18,26,27]. These solutions vary in degree of automation from semi-automated to fully automated, and addressing single processes to complete production line. It is well established that automation enhances accuracy and quality of the final product without sacrificing production speed thanks to the inherent precision of machines and their capability to interpret CAD models.

For cutting and shaping, automation solutions incorporate CNC machining and horizontal and vertical saws available in a table feed [7,28], and tool feed configurations [15]. Joining of studs and sheathing is generally performed in dedicated static framing stations [7], or in multi-functional bridges [6]. The installation of windows, doors, building wraps, siding, and subsequent storage of wall panels incorporate a combination of semi-automated solutions involving material handling systems, namely cranes and turning machines, buffer stations, and multi-functional bridges [6]. The recent incorporation of robot arms equipped with specialized end-effectors into the prefabrication process has been trending [29], as they offer an extended degree of freedom and flexibility beyond traditional machinery. The range of specialized end-

effectors includes parallel grippers and vacuum grippers for material handling, nailer and adhesive application head for joining, and CNC spindle and saws for cutting and shaping [15,30–33].

However, automated insulation installation is currently limited to spray foam [34–36], and blow-in insulation [37,38], both using robotic arms or multi-functional bridges. This is due to their loose form and inherent void-conforming properties, which make the aforementioned insulations suitable for automated application. A comparative study [24] examined systems for installing blow-in insulation that highlighted existing cross-compatibility issues and high investment cost, which deterred widespread adoption of these technologies. The installation of batt insulation still remains completely manual due to its deformable and non-linear material characteristics that complicate the automation implementation. This challenge must be overcome in order to realize automation of batt insulation installation.

### **1.1.2 Techniques for Handling Deformable Objects**

Manipulation for rigid objects only involves changing the pose of the object. The robotic insertion methods of rigid objects, such as the classical peg-in-hole problem in which a robot must align and insert a peg into a hole with tight tolerances, has been well studied in literature over the past three decades, see [39–41]. Meanwhile, the manipulation of deformable or non-rigid objects not only considers changing of pose but also the effects on its shape. The process of detecting and recognizing the deformable object's state during manipulation remains a significant challenge and presents an additional layer of complexity for automation [42].

Various conventional methods for detecting and recognizing the deformation involve approximating a model. Two prevalent approaches to modelling, specifically for 3D objects, are the mass-spring system [42–45], and the finite element method [46]. However, both methods rely on assumptions or approximations of the material's mechanical properties, which can lead to inaccuracies in the models to represent real world deformation behaviors [47,48]. Many researches have applied modern techniques like machine learning [49], sensor-feedback [50], and tactile or visual servoing [45,50], to learn from real data about the forces experienced by the robot in relation to the material's deformation during the material handling process. By leveraging real data on these interactions, appropriate control measures can be implemented to effectively account for the deformation experienced. Existing examples of manipulation of

deformable objects through modeling and validation testing can be found in [51,52]. In those examples, modeling was a complex process and consumed a significant amount of computational resources. In addition, the model obtained through the modeling process is specific for an object and may not be extendable across similar objects or adaptable if there is a large standard deviation in material's properties.

Batt insulation, which exhibits non-static and localized behavior can be classified as a 3D non-rigid to semi-rigid deformable object. The variability caused by its random internal fiber orientation complicates accurate modeling, as mechanical properties and degrees of deformation vary significantly between batts [53–55]. Consequently, considering the approach from [51] which seeks to achieve an interference fit with a deformable ring, utilizing a simplified version of Young's modulus to model insulation as a mass-spring system may not accurately capture the appropriate response curves across different insulation pieces or even localized areas from the same insulation piece. Therefore, developing a robust method that bypasses the need to model the actual deformation, while leveraging the non-rigidity of the insulation, merits further investigation.

When manipulating and handling the deformable materials, the performance and capabilities of a robot are primarily influenced by its end-effector. Five types of basic grippers are prevalent for such purpose, each with distinct features and applications. They are:

1. Clamping grippers: These are the most common off-the-shelf grippers, and are well-established for their precision, scalability, versatility, and ease of modification. They are suitable for handling various deformable materials, such as elastic band [51], ropes [52], plastic bags [56], 3D flexible beam [57]. Their effectiveness typically depends on the object's resistance to permanent deformation when being manipulated. As a consequence, these grippers may fail to provide a consistent grip without damaging the object, such as with batt.

2. Needle grippers: Known for their precision and scalability [58], needle grippers are typically used for handling fabrics [58] and foams [59]. The risk with needle grippers is that the needles may penetrate and damage the batt insulation, which can compromise its thermal resistance.

3. Vacuum grippers: Commonly employed for non-porous deformable materials like sheet metal [60], they are unsuitable for batt insulation due to its porous nature. That is because the

suction-based mechanism fails to create a vacuum seal with porous materials, leading to ineffective force generation [58].

4. Soft grippers: Made from soft materials that accommodate the shape of irregular objects, soft grippers are ideal for sensitive applications like food handling [61], and medical applications [62]. However, they require a complex control system with accompanying sensors and are task-tailored, which lack the versatility required for handling the wide array of sizes of batt insulation.

5. Multi-fingered robotic hands: These anthropomorphic devices mimic the natural movement of a human hand and are equipped with tactile sensors, offering a high degree of freedom and dexterity [63]. However, their complexity and high cost restrict their general adoption and implementation, particularly with large deformable objects [46], such as batt insulation.

The aforementioned grippers are often integrated with other tools to become multipurpose end-effectors, capable of addressing more complicated tasks such as fabric layup [58] and gaskets insertion [64]. To address these challenges and simplify the control process, this research aims to design an end-effector that possesses the necessary features to reliably handle batt insulation for installation into wall frames.

## **1.2 Research Objectives and Scope**

The overarching objective of this research is to develop an efficient and reliable robotic system that automates the installation of batt thermal insulation into wood-frame wall panels. The goal is to achieve successful installation without the need for complex modeling and simulation. The system utilizes only one robot arm in order to minimize initial investment costs. In accordance with industry standards [65,66] for insulation installation, the success is defined by the following criteria: 1) the insulation fits tightly within the frame cavity; 2) there are no visible voids or gaps between the insulation and wood frame; 3) there is no unwanted deformation of the insulation.

To achieve the overarching objective, the research has the following four activities:

1. Developing a robotic process for installing batt thermal insulation into light-frame cavities to mitigate the influence from uncertainties due to deformation and non-linear mechanical properties.

2. Identifying and tuning variable parameters of the developed robotic process to ensure the integrity and repeatable success of batt insertion and to avoid robot collisions.

3. Designing a custom robotic end-effector tailored to proficiently manipulate batt thermal insulation.

4. Implementing and validating the proposed robotic installation process and end-effector within an in-lab robotic cell to confirm functionality and effectiveness.

Our scope is limited to a standardized configuration of the wood-frame wall panel, which is a typical straight wall without any internal obstructions such as any piping or wiring. The wood studs used are pre-selected to ensure minimal warping and twisting, contributing to the consistency of the robotic installation process. Additionally, the wood frames are set on a flat working platform, and the insulation is assumed to be pre-cut prior to the installation process.

This research is part of a broader collaboration with RoBIM Technologies Inc., focusing on the development of prefabricated exterior wall panels for robotic building retrofits. Interested readers are referred to Appendices A and B for additional information on two original works during the collaboration with RoBIM. Appendix A provides information on the fire safety provisions for timber framing construction, while Appendix B covers the thermal analysis required to ensure compliance with Canadian building codes.

### **1.3 Thesis Outline**

The structure of the remainder of this thesis is outlined as follows.

Following the introduction (background information, literature survey, objectives and scope) in Chapter 1, Chapter 2 presents a proof of concept for a robotic batt insulation installation method that was designed and tested through vertical pickup strategy for a scaled wall frame. Applying the lessons learned from Chapter 2, Chapter 3 investigates an alternate robotic insertion method via horizontal pickup strategy for full-scale wall frames. Chapter 4 concludes the thesis findings and provides potential future directions related to this work.

## **Chapter 2 : Vertical Pickup Strategy**

In this chapter, we introduce a robotic method for installing batt insulation into a scaled wall frame via a vertical pickup strategy. A scaled wall frame was used due to hardware limitations related to the size and capacity of our existing robot arm at the time. However, this chapter serves as a foundation and substantiation for further investments to extend the method to full-size wall panels, which is investigated in our subsequent chapter.

This chapter is organized as followings: Section 2.1 describes the methodology that was used to obtain the robotic method, including the end-effector and installation process. Section 2.2 demonstrates the effectiveness of our designed robotic method through experiment trials. Lastly, Section 2.3 concludes the chapter.

### **2.1 Methodology**

The methodology in this chapter was designed to address the research objective previously outlined in Section 1.2, with a focus on developing a robotic method that comprises two main components: the robotic installation process and the end-effector. The chapter begins by introducing the existing in-lab robotic cell which includes a platform setup, a robot arm, and a parallel gripper. Given the limitations of conventional grippers and the unique challenges posed by batt insulation, such as its deformation and non-linear mechanical properties, an end-effector was designed to utilize the existing parallel gripper while incorporating additional features to handle batt insulation effectively. To address these challenges, a six-step robotic process termed V-GLITPP was developed. This process avoids the need for complex modeling by focusing on practical manipulation strategies. The operational parameters for the V-GLITPP method were identified through the robotic process, and their values were experimentally tuned and determined to ensure the functionality and effectiveness of the process while avoiding robot collisions. Following parameter tuning, robotic simulations in a digital twin environment were performed to model and implement the process. These simulations were crucial for ensuring a seamless transition from the digital environment to the actual robot arm for validation purposes. The validation involved additional experiments to confirm the accuracy and repeatability of the process. Figure 2.1 illustrates the flow chart of the methodology.

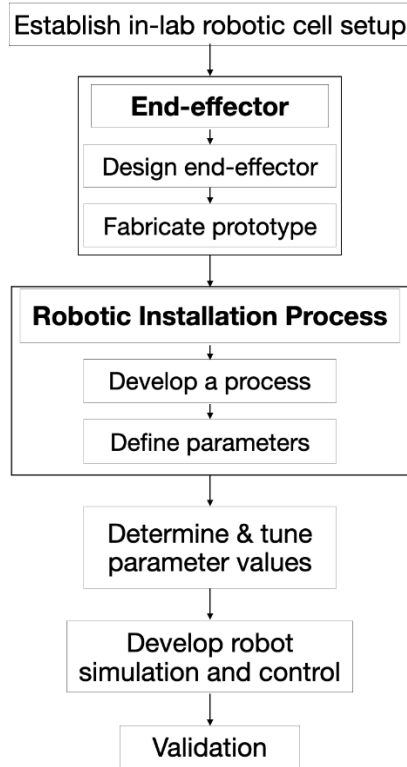


*Figure 2.1: Overview of proposed methodology for vertical pickup configuration*

### 2.1.1 In-lab Robotic Cell Setup

The setup of the in-lab robotic cell is illustrated by Figure 2.2. A Universal Robot UR5e was utilized as the robotic manipulator. The UR5e is a robot arm with 6 degree-of-freedom. Its operational capacity is 11 lbs (5 kg) for payloads and accompanied by a maximum reach span of 33.5 inches (850 mm). The robot arm was mounted on a 46 by 34 inches (1168 x 864 mm) table platform. The platform's upper surface is constructed from plastic, providing a smooth texture that minimizes friction effects between the insulation and the surface. Ultimately, the prototyped end-effector was affixed to the 6<sup>th</sup> axis of UR5e.

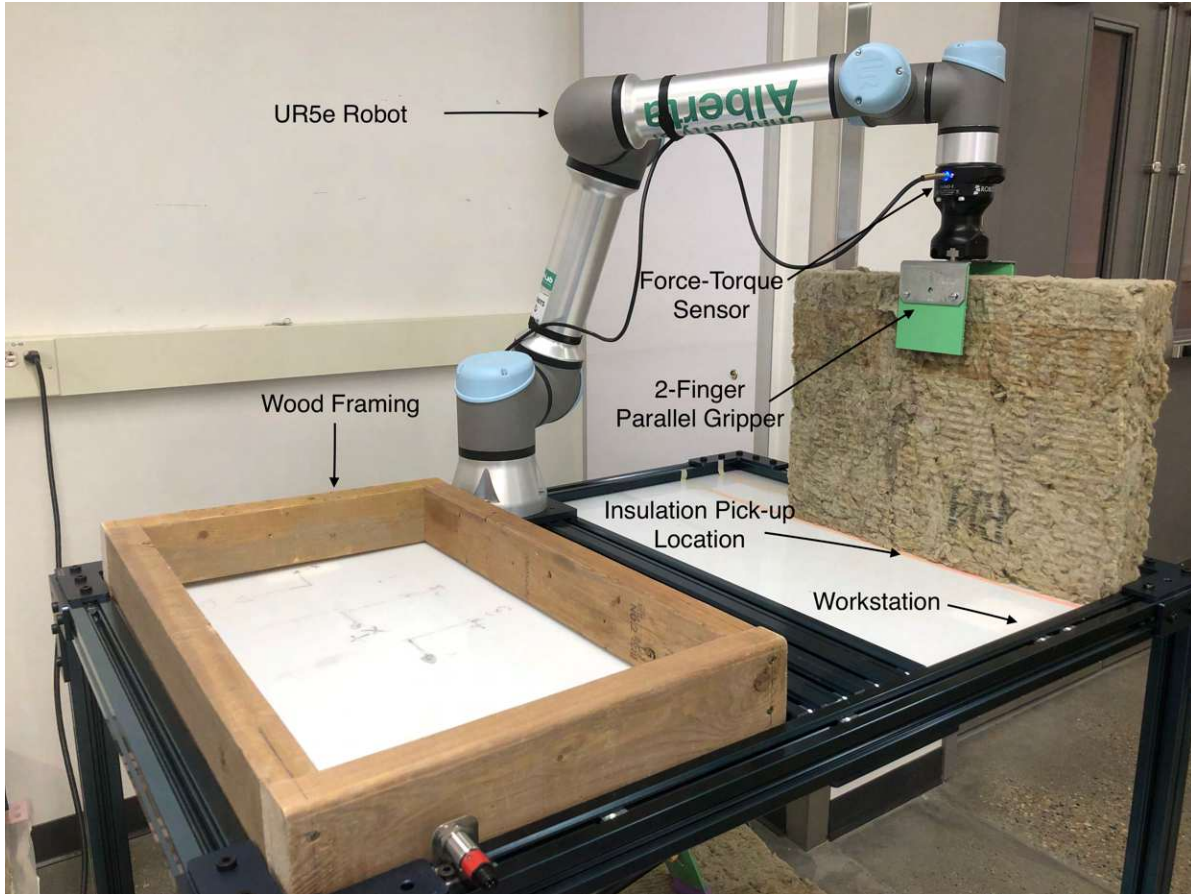


*Figure 2.2: The in-lab robotic cell setup*

The scaled wall frame utilized in this chapter is constructed using four 2-by-4 SPF Dimensional Lumber. This lumber dimension is representative of a most common type of wood-frame wall used in light-frame construction. The spacing between wood studs is set at 16 inches (406 mm) on-center, a standard stud spacing commonly employed in building construction, which results in a cavity width of 14.5 inches (368 mm). Due to hardware constraints, specifically the reach of the robotic arm, the height of the wall cavity has been scaled to 26 inches (660 mm), instead of a typical 8-foot (2438 mm) wall. Hence, the overall dimensions of the wood cavity are 14.5 inches (368 mm) in width, 26 inches (660 mm) in height, and 3.5 inches (89 mm) in depth.

### **2.1.2 End-Effector Design**

Illustrated in Figure 2.3, the end-effector comprises four components: a two-finger gripper, a force-torque sensor, an adaptor, and a pair of gripping jaws. The two-finger gripper with linear

stroke is an off-the-shelf product. For standard batt insulation, its width is slightly larger than the width of the cavity so that a tight-fit can be achieved once inserted. This dimensional difference requires the robot arm to apply compressive force to insert the batt insulation into the cavity. Therefore, a force-torque sensor that allows control of the applied force is mounted atop of the two-finger gripper. The gripping jaw adaptors are designed to connect the off-the-shelf gripper to the gripping jaws. The last component of the end-effector is the custom-built gripping jaws. The inside surface of the jaw is textured to increase friction between the jaw and the insulation, which with all else being equal, reduces the grasping force. The size of the jaws can vary but should consider the dimensions and weight of the insulation, as well as its degree of elasticity. The jaw dimension is crucial to minimize the permanent deformation during manipulation.

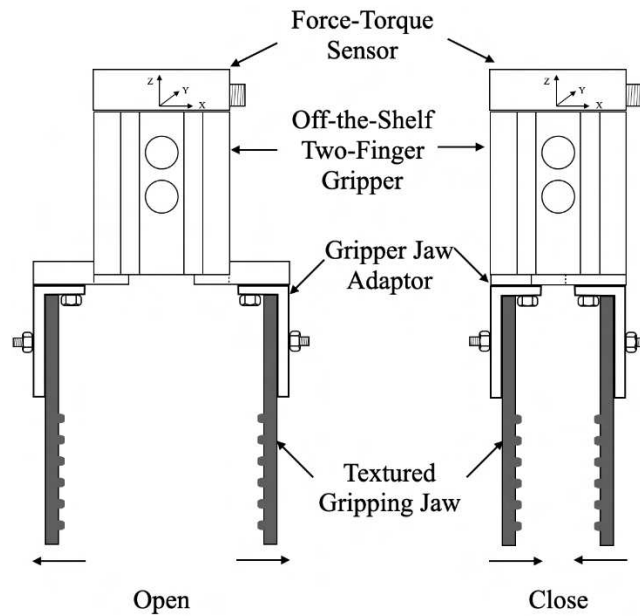


*Figure 2.3: The proposed robotic end-effector in open and close positions*

### 2.1.3 End-effector Prototype

For the implementation, a prototype of the robotic end-effector was developed, see Figure 2.4. Detailed specifications of the end-effector components are listed under Table 2.1. The Robotiq FT 300-S Force Torque sensor, capable of measuring forces up to  $\pm 67.4$  lbf ( $\pm 300$  N) was utilized. Additionally, the Robotiq Hand-e gripper, with a maximum stroke length of 2 inches (50 mm), served as the parallel gripper. The custom adaptor was designed, in accordance

with the Hand-e gripper specifications, to incorporate M3 screws for attachment onto the gripper's mounting interface. The gripping jaws, with dimensions designed as 4 by 4-1/2 inches (102 x 114 mm) and a thickness of 3/16 inch (4.76 mm), were 3D printed with a textured interior surface at the lower section. The final assembly of the end-effector provides an opening for objects of 3-3/4 inches (95 mm) when the gripper is open and reduces to 1-3/4 inches (44 mm) when closed.



Figure 2.4: The prototyped robotic end-effector at fully open position (left) and at fully closed position (right)

Table 2.1: Specifications of the end-effector prototype

Component	QTY	Material	Weight [lbs (kg)]	Specifications
Force torque sensor	1	-	0.97 (0.44)	<ul style="list-style-type: none"> <li>• Manufacturer: Robotiq</li> <li>• Model: FT 300-S</li> <li>• Measuring range: <math>\pm 67.4</math> lbf (<math>\pm 300</math>N)</li> </ul>
Parallel gripper	1	-	2 (1)	<ul style="list-style-type: none"> <li>• Manufacturer: Robotiq</li> <li>• Model: Hand-e</li> <li>• Stroke per finger: 1 in (25mm)</li> <li>• Grip payload: 15.4 lbs (7 kg)</li> </ul>

				<ul style="list-style-type: none"> <li>Gripping force: 4.5 to 41.6 lbf (20 to 185 N)</li> </ul>
Adaptor	2	Steel	0.67 (0.3)	Machined
Gripping finger	2	PLA	0.08 (0.04)	<ul style="list-style-type: none"> <li>3D printed</li> <li>Size (W x L x T): 4 x 4-1/2 x 3/16 inch (102 x 114 x 4.76 mm)</li> </ul>

### 2.1.4 Installation Process

The proposed process for inserting batt insulation in this section is inspired by both the manual insertion process [65,66] and the research conducted by Kim et al. [40]. The latter research focused on the insertion of rigid objects into shallow cavities, incorporating primitive operations such as grasping, tilting, and tucking. In the context of batt insulation insertion, the proposed robotic insertion process, termed as V-GLITPP, contains six major steps: (1) Grasp, (2) Lift, (3) Insert, (4) Tilt, (5) Push, and (6) Press (as illustrated in Figure 2.5).

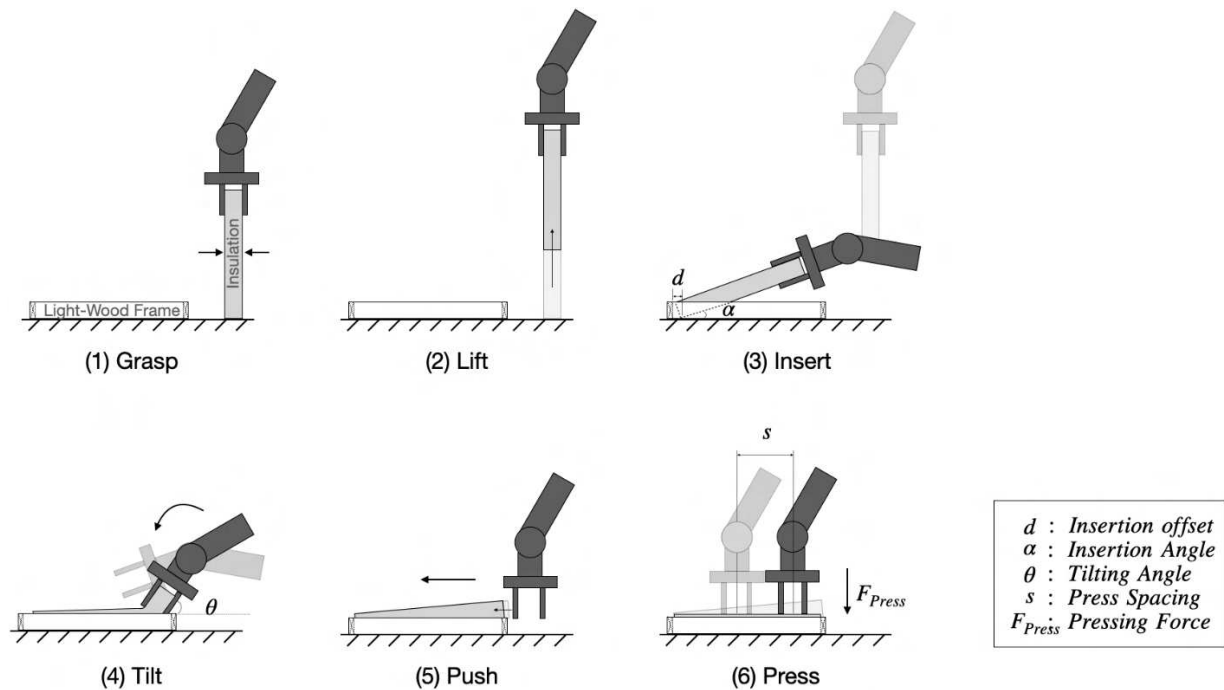


Figure 2.5: The V-GLITPP insertion process

The initial step is to grasp the insulation from an initialized position. The robot arm moves to the top of the insulation using a point-to-point motion (PTP motion). Subsequently, the robot arm descends linearly (LIN motion) until the gripper reaches the insulation’s top edge. Upon reaching the edge, the gripper closes to securely grasp the insulation. The second step is lifting. After grasping the insulation, a LIN motion is utilized to lift up the insulation linearly. This is followed by a PTP motion to position the insulation in proximity of the frame cavity. In the third step, a combination of PTP and LIN motions is programmed to insert one edge of the insulation into the frame cavity with consideration of an insertion angle ( $\alpha$ ) and offset ( $d$ ). For the fourth step, the end-effector is tilted. This ensures that when the grippers open, they avoid collisions with the frame and release the insulation without shearing. Achieving this involves a PTP motion, tilting the end-effector to a specific angle ( $\theta$ ), and then releasing the insulation. To align the insulation accurately with the frame, pushing operations are employed along the uninserted edges. For this, the robot arm utilizes LIN motions to enable the gripping jaws to gently push the insulation until it aligns flush with the cavity. In the final step, the gripping jaws are employed to press the uninserted edges of the insulation into the frame cavity, using defined press spacing ( $s$ ) and pressing force ( $F_{Press}$ ) parameters. The pressing pattern initiates from the corners of the inserted edge and proceeds along the edges perpendicular to the inserted edge and before finally pressing along the uninserted edge, that is parallel to the inserted edge. The task description and associated robot motions outlined above are summarized in Table 2.2.

*Table 2.2: Six steps of the V-GLITPP insertion process*

<b>Steps</b>	<b>Task Description</b>	<b>Related robot motions</b>
Grasp	From the initial position, the insulation is securely grasped by robotic gripper for pick up and manipulating.	<ol style="list-style-type: none"> <li>1. PTP motion to the top of the insulation</li> <li>2. LIN motion down till the gripper reaches the insulation’s edge</li> <li>3. Close the gripper</li> </ol>
Lift	The robot arm picks up the insulation and moves it close to the frame cavity.	<ol style="list-style-type: none"> <li>1. LIN motion to lift the insulation</li> <li>2. PTP motion to move the insulation close the frame cavity</li> </ol>
Insert	The robot arm inserts the insulation into the cavity with an insertion angle	<ol style="list-style-type: none"> <li>1. PTP motion to rotate the insulation.</li> <li>2. LIN motion to insert the insulation into</li> </ol>

---

	( $\alpha$ ) and offset ( $d$ ).	the cavity
Tilt	The robot arm tilts the insulation to a tilting angle ( $\theta$ ).	<ol style="list-style-type: none"> <li>1. PTP motion to tilt the insulation</li> <li>2. Open the gripper</li> </ol>
Push	The robot arm uses its gripping jaw to push the insulation along the uninserted edges of the insulation until it is flushed with the cavity.	<ol style="list-style-type: none"> <li>1. LIN motion down till tip of the gripping jaw reaches the limit</li> <li>2. LIN motions parallel to the frame's direction to push the insulation into the cavity</li> </ol>
Press	The robot arm uses its gripping jaws to press the insulation into the frame cavity.	<ol style="list-style-type: none"> <li>1. PTP motion to the pressing location</li> <li>2. LIN motions descend till the force reaches the pressing force</li> <li>3. LIN motion up</li> <li>4. LIN motion to the section pressing location</li> <li>5. Repeat step 2 to 4 until the insulation is fully inserted.</li> </ol>

---

### 2.1.5 Parameter Results

The V-GLITPP insertion process involves five key parameters: insertion angle ( $\alpha$ ), insertion offset ( $d$ ), tilt angle ( $\theta$ ), press spacing ( $l$ ) and pressing force ( $F_{Press}$ ). These parameter values were determined through a series of individual robotic trials. All the trials were tested on 26 inches (660 mm) length of mineral wool insulation. Once a set of feasible parameter values was ascertained, they were integrated to illustrate and formalize the entire robotic insertion process for both mineral wool and fiberglass, the results of which is presented within Section 2.2.

#### 2.1.5.1 Insertion angle ( $\alpha$ ) & Insertion offset ( $d$ ) & Tilt angle ( $\theta$ )

There exists an interdependency among the insertion angle ( $\alpha$ ), insertion offset ( $d$ ), and tilt angle ( $\theta$ ). Changes in the values of one parameter affect the other, as demonstrated by Eq.1. This equation represents an affine function that defines all points ( $x, y$ ) on the outer surface of the fully opened gripper jaw in its tilted position. Most importantly, the parameter values must satisfy the condition that the affine function (hyperplane) is positioned to the left of the boundary

point (P). This arrangement ensures collisions-free between the frame and the gripper. Figure 2.6 illustrates the variables used in Eq.1 where: L represents the distance from the tool center point (TCP) to the end of the insulation; H is the wood stud width, which is equal to the insulation thickness; W denotes the frame cavity width; E stands for the distance from the TCP to end of the gripper; G represents the distance between the center line and the outer surface of the gripper jaw in its fully open position; P corresponds to the inner edge of the wood stud, serving as the boundary point.

$$y = \frac{2x * \sin(\theta) - 2L * \sin(\theta - \alpha) + H * \cos(\theta - \alpha) - 2 * d * \sin(\theta) - 2G}{2 \cos(\theta)} \quad (\text{Eq. 1})$$

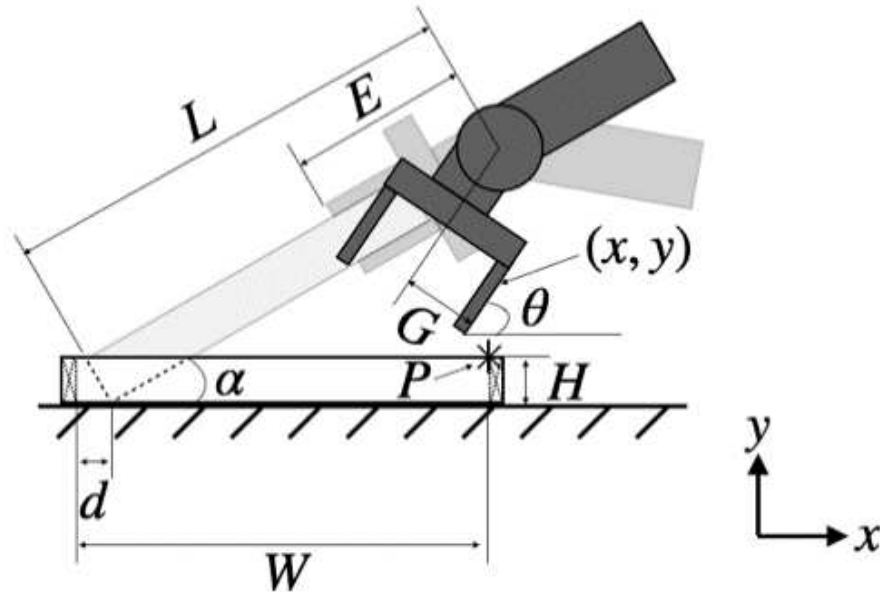


Figure 2.6: Illustration of the variables in Eq.1

As a consequence of the texturing on the gripper, a tilt operation is employed to facilitate the release of insulation from the gripper jaws after insertion into the frame cavity. This approach reduces disruptions to the insulation's intended position, prevents damage to its fibers by eliminating shearing, and allows for maintaining a minimal insertion angle. Obtaining the minimum tilt angle is essential for the effective release of insulation. The determination of the minimum tilt angle needed allows for subsequent calculation of the insertion angle and offset. Moreover, tilting indirectly contributes to the insertion process by leading more edges of the insulation into the frame cavity. The minimum tilt angle is determined to be 55°, given the

insulation’s nominal weight and frictional forces. Through trials, a list of tilt angles and their corresponding outcomes are presented under Table 2.3.

*Table 2.3: A list of trialed tilt angles with success rate*

$\theta$ (°)	Success Rate	Failure Mode
30	0/5	Insulations were pulled out of the frame cavity.
45	0/5	Insulations were first pulled, followed by shearing of the insulation fibers
55	5/5	N/A

The insertion offset is defined as the distance between the insulation’s inserted edge and the frame. When the offset is either too small or too large, the risk of collision increases during the insertion or pressing steps, respectively. This necessitates finding a balance between within the feasible range of offsets. Regarding the insertion angle, a smaller angle results in a longer length of edge of the insulation being inserted into the frame cavity. This minimizes the likelihood for the insulation’s edges to catch or snag during the subsequent titling and pressing steps, thus, ensuring proper seating of the insulation within the frame cavity. The lower limit of the insertion angle depends on the tilt angle in order to prevent collisions after titling, when the grippers open to release the insulation. The insertion angle for a specific insertion offset, utilizing the minimum tilt angle obtained earlier, can be determined from Figure 2.7. This figure is generated by computing the solution pairs that satisfy Eq.1. Three combinations were selected for testing and the results are presented in Table 2.4. The tested minimum feasible combination of insertion angle and insertion offset is achieved at 30° with an offset of 0.75 inches (19 mm).

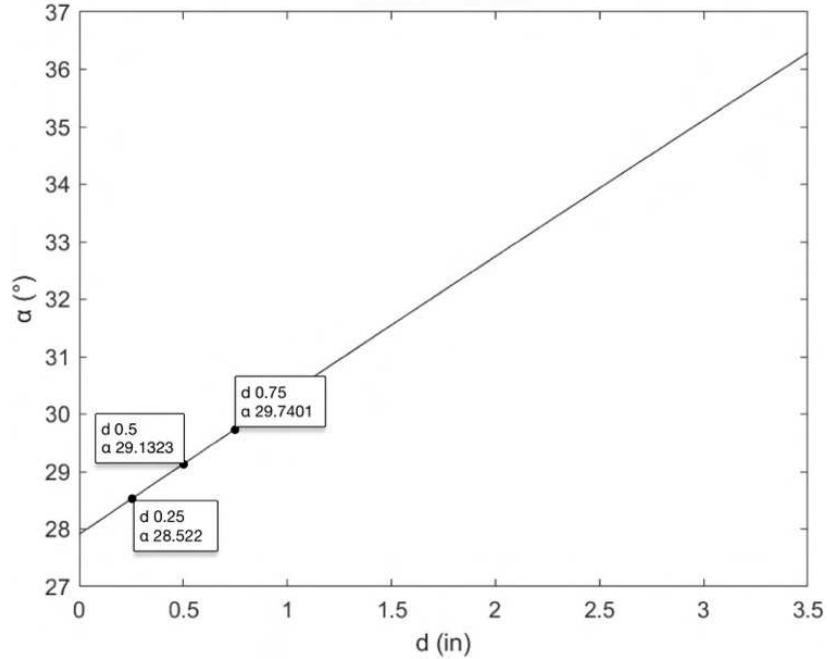


Figure 2.7: Combination of insertion angle and insertion offset

Table 2.4: A list of trialed combination of insertion angle and insertion offset with success rate

$\alpha$ (°)	d [in (mm)]	Success Rate	Failure Mode
28.5	0.25	0/5	Collision warning during insertion due to excessive compression of insulation.
29	0.5	0/5	Collision warning during insertion due to excessive compression of insulation.
30	0.75	5/5	N/A

### 2.1.5.2 Press spacing (s)

The press spacing signifies the positions where the gripper will apply pressure along the uninserted edge of the insulation, facilitating its complete insertion into the frame cavity while ensuring no insulation edges remain exposed. While there are no explicit limitations on the quantity of presses, minimizing press count contributes to time efficiency. In the conducted trials, the center-to-center distance of the press spacing varies from 15 to 5 inches (381 to 127 mm), with the initial press initiated from a corner of an inserted edge. The outcomes of the trials are compiled in Table 2.5. It was noted that a 5-inch (127 mm) press spacing effectively accomplishes the insulation's insertion into the frame cavity, without any conspicuous convexity.

Table 2.5: A list of trialed press spacing with success rate

<b>s [in (mm)]</b>	<b>Success Rate</b>	<b>Failure Mode</b>
15 (381)	0/5	Evident convexity noticeable between each press point.
10 (254)	3/5	Evident convexity noticeable between certain press points.
5 (127)	5/5	N/A

### 2.1.5.3 Pressing force ( $F_{Press}$ )

Once the press spacing is determined, it becomes crucial to apply the minimum amount of force necessary to press the insulation into the frame cavity. This approach ensures that the insulation avoids permanent deformation, which could lead to a loss of effective R-value. The lower and upper bounds for the pressing force are 18 lbf (80 N) and 27 lbf (120 N), respectively. The results of the trials are listed in Table 2.6. It was determined that a pressing force of 22.5 lbf (100 N) fully and reliably presses the insulation into the frame cavity each time without unwanted deformation to the insulation.

Table 2.6: A list of trialed pressing force with success rate

<b><math>F_{Press}</math> [lbf (N)]</b>	<b>Success Rate</b>	<b>Failure Mode</b>
18 (80)	2/5	There were instances that the insulation was not fully pressed in.
22.5 (100)	5/5	N/A
27 (120)	4/5	There was an instance where the insulation had permanent deformation.

### 2.1.6 Robot Simulation and Control

The model and control of the UR5e’s robotic process employs the RoBIM software, illustrated in Figure 2.8. The software is a robotic simulator solution that provides a digital twin environment for controlling the robotic arm and provides trajectory simulation with collision avoidance capabilities. It is worth mentioning that the collision avoidance algorithm assumes the handle object is a rigid body. During grasping and lifting operations, the insulation can be treated as rigid body for the purpose of collision avoidance as minimal deformation occurs. During insertion, tilt, and pressing operations, the collision warning is ignored as significant deformation is required to achieve a tight insertion of the insulation into the frame cavity.

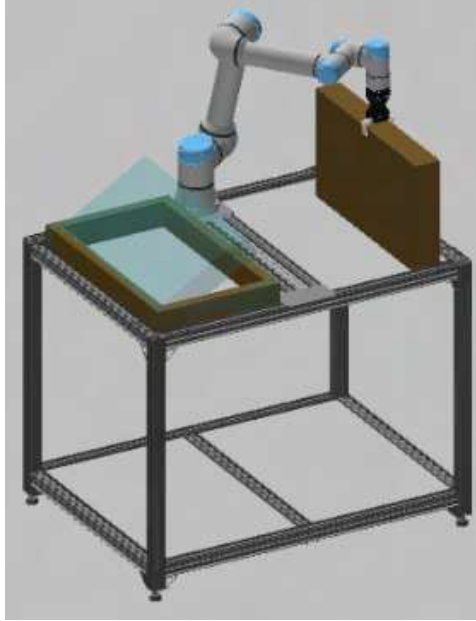


Figure 2.8: Simulation environment in RoBIM software

## 2.2 Validation

The designed V-GLITPP process was tested using the parameters values obtained in Subsection 2.1.5 and listed in Table 2.7. Tests were conducted on both mineral wool and fiberglass batt insulations at the robot arm’s maximum linear TCP speed of 39.4 in/s (1000 mm/s). These tests included ten trials for each insulation configuration under two distinct scenarios. Each test was performed using new insulation to simulate the actual application in construction.

Table 2.7: Summarized selected parameter values obtained from Subsection 2.1.5

Parameter	Value
Tilt Angle ( $\theta$ )	55°
Insertion Angle ( $\alpha$ )	30°
Insertion Offset (d)	0.75 in (19 mm)
Press Spacing (s)	5 in (127 mm)
Pressing Force ( $F_{Press}$ )	22.5 lbf (100 N)

### 2.2.1 Overview

Two scenarios were designed to represent the actual configurations of insulation installation in construction, as illustrated in Figure 2.9:

Scenario 1 (S1): A single piece of insulation fills the entire 26 inches (660 mm) length of the frame cavity.

Scenario 2 (S2): Two pieces of insulation places in tandem within the frame cavity.

S2.1: The first step involves inserting a 20-inch (508 mm) piece to contact three sides of the frame.

S2.2: The Second step involves inserting a 6-inch (152 mm) piece to complete the fill of the frame cavity. During the insertion of the 6-inch (152 mm) piece, an additional 1-inch (25.4 mm) offset was applied between the two insulations to avoid the interaction of large frictional forces between the mating surfaces.

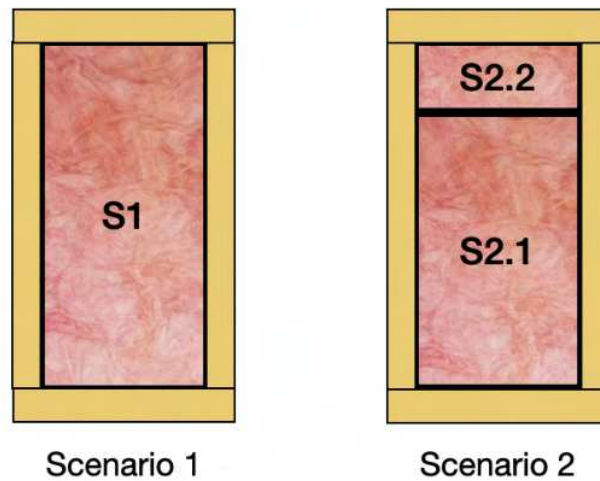


*Figure 2.9: Two scenarios*

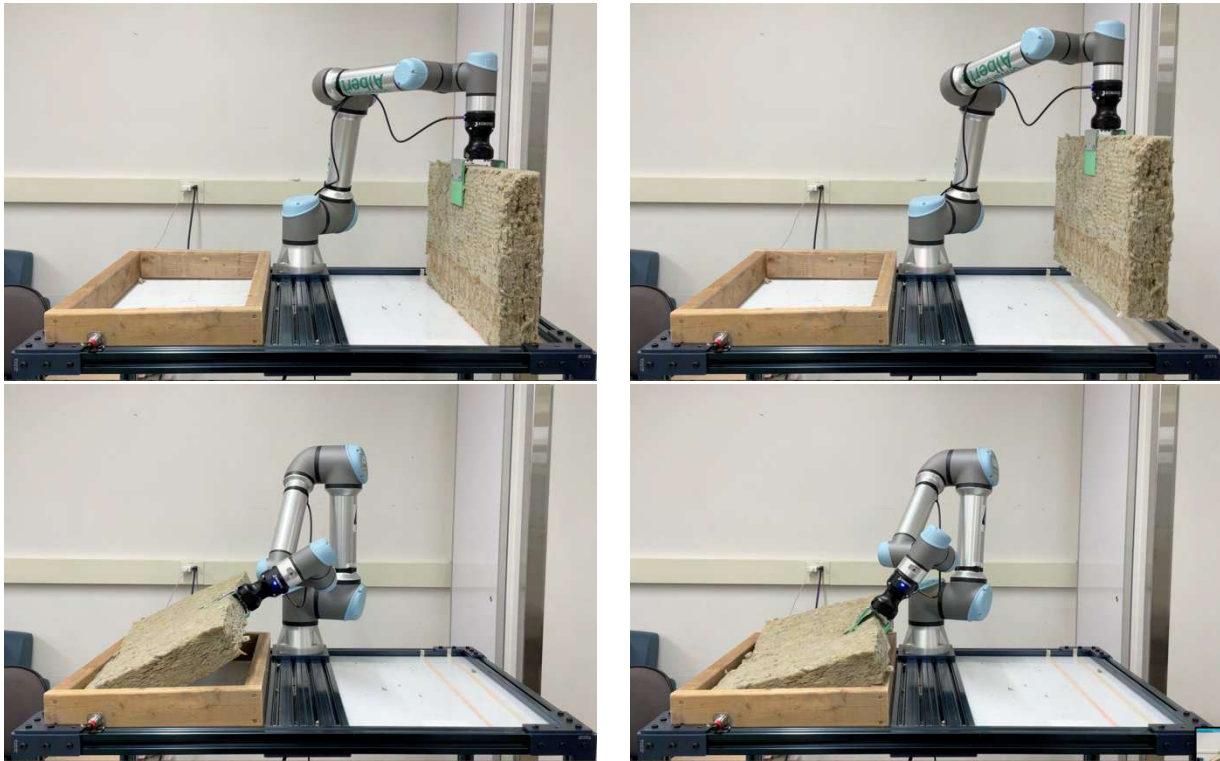
### 2.2.2 Results and Discussion

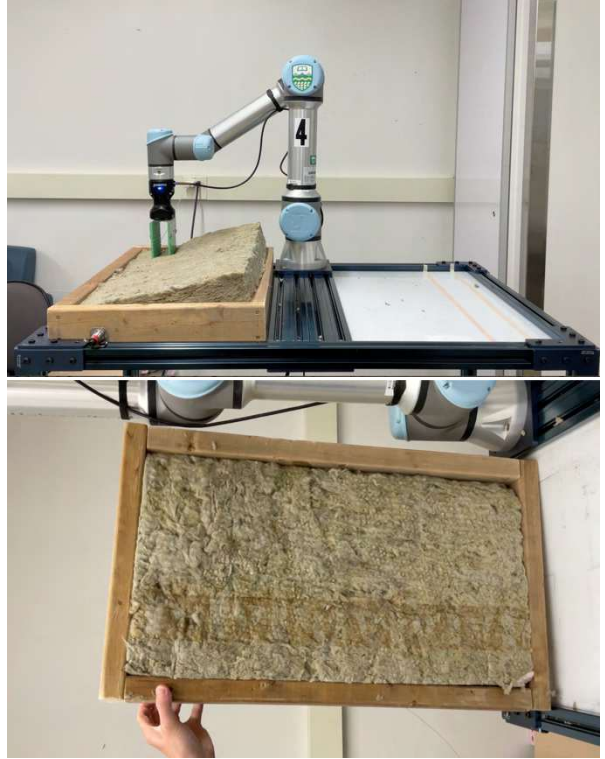
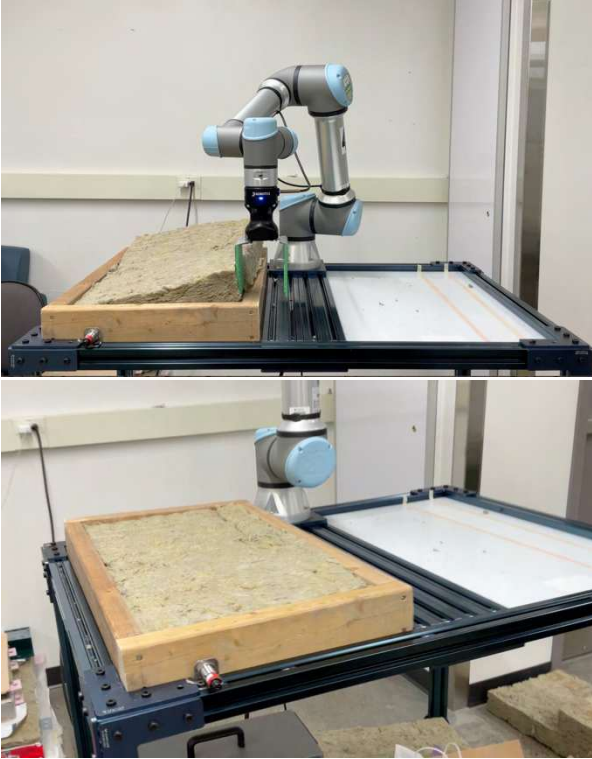
Table 2.8 summarizes the experiment results using the selected parameters obtained in Subsection 2.1.5. Figure 2.10, Figure 2.11, and Figure 2.12 illustrate the progress throughout the experiments and the final results of the insertion with the front and back views of the insulation for S1 in mineral wool and S2 in fiberglass. Additional experiment figures are presented in Appendix C. The success of the entire V-GLITPP insertion process is defined by the insulation

fitting tightly within the frame cavity, the absence of visible voids and gaps between the insulation and wood frame, and the insulation having no shearing or permanent deformation. Given the success criteria, the overall success rate of the V-GLITPP stands at 93.3%.

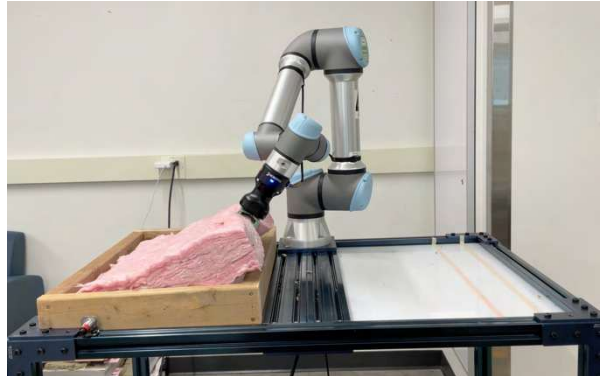
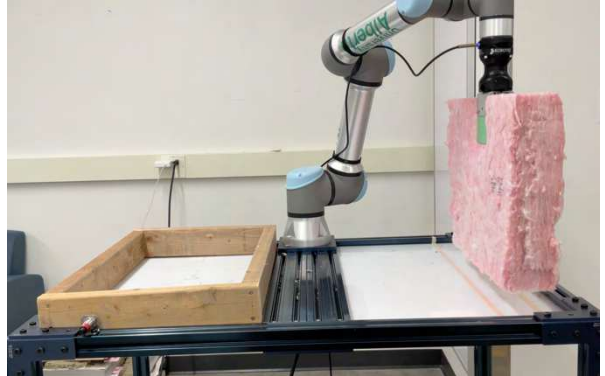
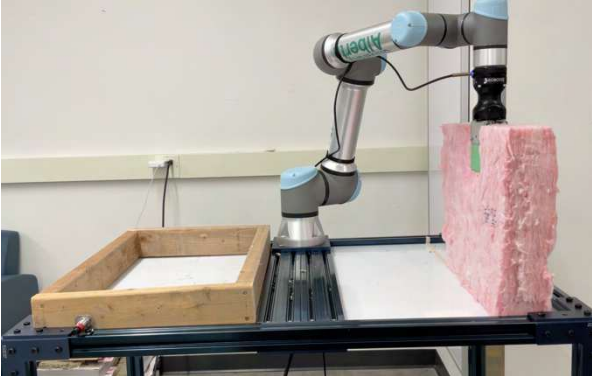
*Table 2.8: Experiment results for entire V-GLITPP insertion process*

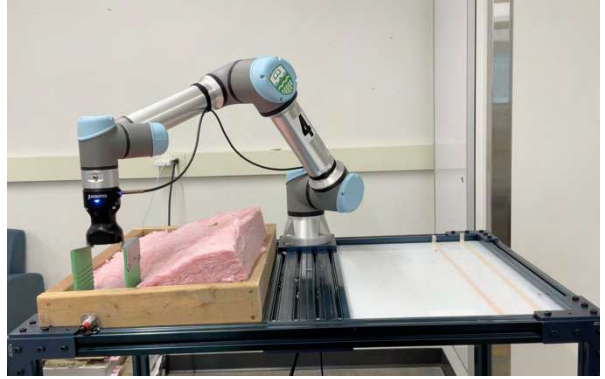
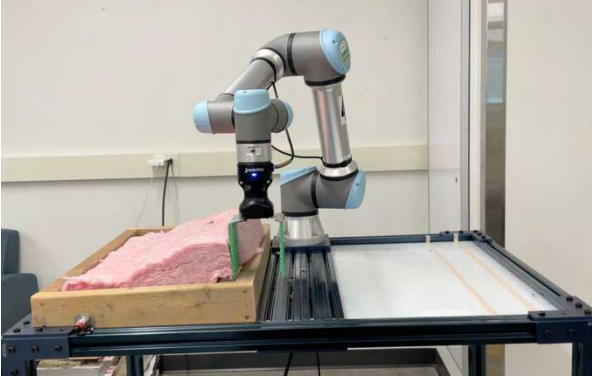
Scenario	Insulation Length [in (mm)]	Batt Insulation Type	Success Rate
1	26 (660)	Mineral Wool	9/10
1	26 (660)	Fiberglass	10/10
2.1	20 (508)	Mineral Wool	10/10
2.1	20 (508)	Fiberglass	9/10
2.2	6 (152)	Mineral Wool	8/10
2.2	6 (152)	Fiberglass	10/10



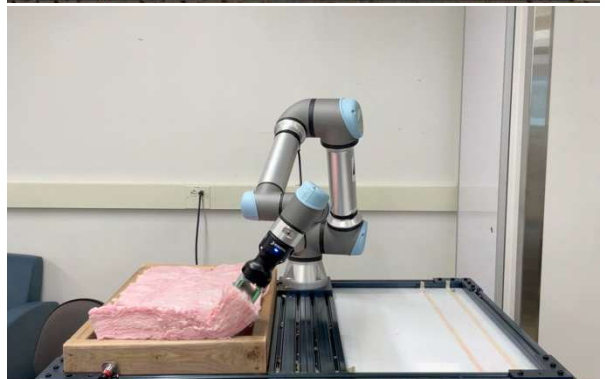
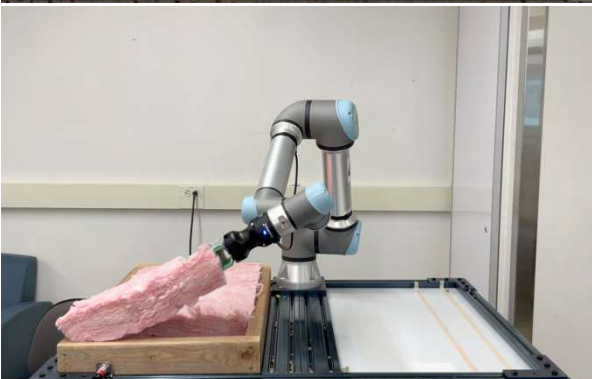
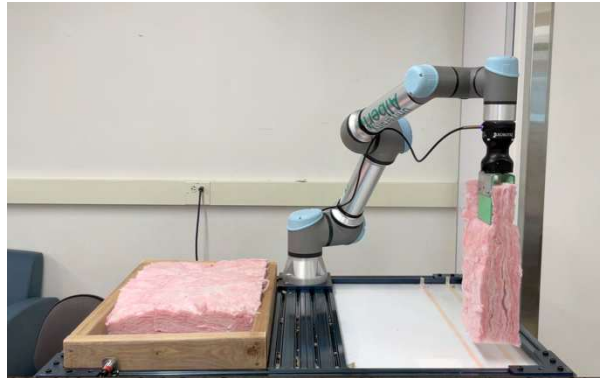
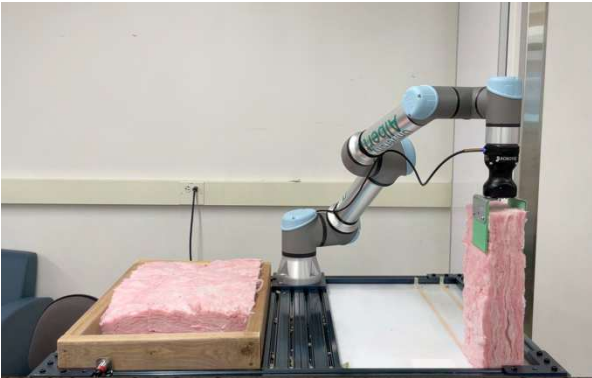


*Figure 2.10: V-GLITPP process for Scenario 1 with mineral wool insulation (Grasp, Lift, Insert, Tilt, Push, Press, front and back completion views)*





*Figure 2.11: V-GLITPP process for Scenario 2.1 with fiberglass insulation (Grasp, Lift, Insert, Tilt, Push, Press, front and back completion views)*



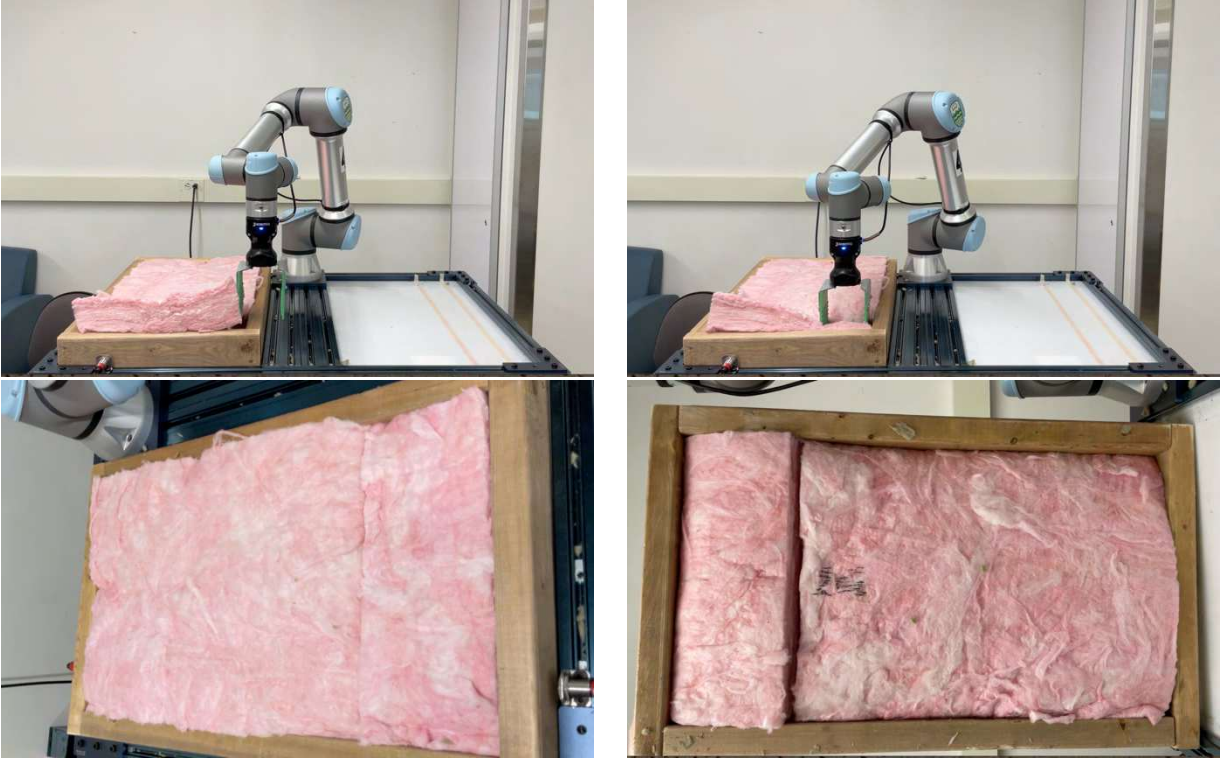


*Figure 2.12: V-GLITPP process for Scenario 2.2 with fiberglass insulation (Grasp, Lift, Insert, Tilt, Push, Press, front and back completion views)*

The high success rates, as showed in Table 2.8, were achieved by mitigating the negative effects of deformation and uncertainties in mechanical properties while leveraging the non-rigidity of the insulation through each step of the V-GLITPP insertion process. The integration of individual parameter selection into a single continuous process, facilitated by a custom-built gripper, is seamless and repeatable. The results demonstrate that the manipulation of batt insulation using the designed grasping, lifting, and inserting steps are capable of achieving high positional accuracy. The tilting step reduces the risk of shearing of the insulation during release, while the pushing step guides the insulation into an orientation where uncertainties and random disturbances are minimized before pressing. Ultimately, the pressing step ensures a tight-fitted insulation within the frame cavity, without any discernible gaps and deficiencies.

There were four instances in which the V-GLITPP process did not succeed. In Scenario 2.1, the failure was an outlier, as no defects were observed in the insulation. For Scenarios 1 and 2.2, the lack of success resulted from pre-existing creases and pockets of low-density in the insulation. Notably, the insulations used in validation were all chosen randomly from the

packaging without any rejection of unideal pieces of insulation. Incorporating insulation pre-inspection, selection, and rejection would raise the success rate.

## **2.3 Chapter Conclusion**

This chapter introduces a robotic method to insert batt thermal insulation into wall frame. The method comprises two major components: a custom-built end-effector and a corresponding robotic insertion process. The end-effector seamlessly integrates a force-torque sensor, a two-finger gripper, an adaptor, and a pair of gripping jaws. The proposed robotic insertion process, named V-GLITPP, encompasses a sequence of six major steps: Grasp, Lift, Insert, Tilt, Push, and Press. To identify the variable parameters within the V-GLITPP insertion process, an in-lab robotic cell equipped with a prototyped end-effector was utilized. Through a series of individual robotic trials and iterative refinements, these parameter values were determined. The effectiveness and feasibility of the proposed robotic method were evaluated using two common batt thermal insulations: mineral wool and fiberglass. Test scenarios encompassed both a single insulation piece filling the entire frame cavity and the tandem placement of two insulation pieces within the cavity. The results exhibited a remarkable 93.3% success rate for the V-GLITPP insertion process. As our objective is to develop a robotic method for the installation of batt insulation in wall panel prefabrication, we look to expand the V-GLITPP method to full-size frames.

## **Chapter 3 : Horizontal Pickup Strategy**

Chapter 2 was initially developed and tested on a scaled wood frame, which has demonstrated that robotic insulation installation is viable. As a result, we made significant financial investments to support the insulation installation process for full-scale frames, such as: a larger capacity and reach robot arm, longer stroke grippers, and commissioned custom fabrications. However, directly scaling up the V-GLITPP method to full size implementation presents a key challenge. While the method is effective with smaller-sized insulation, the handling of large-sized insulation introduces more difficulties due to potential shape distortions as a result of its own weight. The flexibility and weight of larger insulation batts also add greater uncertainties and complexities during the installation process, especially during the tilt step of V-GLITPP. In addition, when batt insulation is fed in a vertical configuration, it necessitates an additional step to separate the insulation from a stack and additional support to prevent falling during vertical pickup. Nonetheless, we apply the research, techniques, lessons learned from V-GLITPP to facilitate full-size implementation in horizontal pickup configuration to reduce the aforementioned additional step and support.

In this chapter, we introduce a robotic method to install batt insulation into full size wall frames through a horizontal pickup strategy. The outcomes of this chapter include the design, development, and testing of both the installation process and end-effector. Similar to the outline of the previous chapter, Section 3.1 describes the methodology used to obtain the robotic method including the end-effector and installation process. Section 3.2 demonstrates the effectiveness of our designed robotic method through experiment trials. Lastly, Section 3.3 concludes the chapter.

### **3.1 Methodology**

The methodology for this horizontal pickup strategy builds on the insights gained from Chapter 2, with a focus on full-size batt insulation installation. This section outlines the development of the H-GLPPR process, a five-step robotic method tailored to overcome the challenges identified with the vertical pickup strategy, such as the need to accommodate the size, weight and orientation of the full-size batt insulation. To ensure efficiency of the installation process, the key operational parameters were identified, and a dedicated multi-purpose end-effector was engineered to enhance the functionality of the end-effector used in Chapter 2. A

prototype of this end-effector was fabricated and tested within an established in-lab robotic cell setup. The parameter values were tuned and determined through experimentation with the prototype to prevent material damage and collisions while ensuring a tight-fit. Additionally, robotic simulations and control algorithms were developed to model and implement the H-GLPPR process. These simulations facilitated a smooth transition from theoretical models to practical robot operations. Validation involved conducting further experiments to verify the accuracy and repeatability of the process. Figure 3.1 illustrates the flow chart of the methodology.

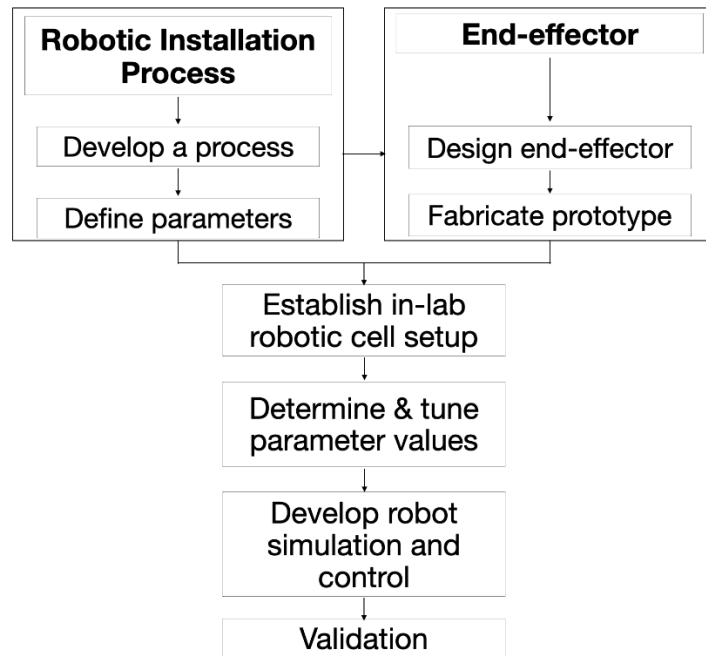


*Figure 3.1: Overview of proposed methodology for horizontal pickup configuration*

### 3.1.1 Installation Process

The proposed robotic process for installing batt insulation, draws inspiration from both traditional manual installation techniques [65,66], as well as insights from the existing V-GLITPP method. The process addresses the main challenges outlined in the introduction section, such as the deformable nature of batt insulation and achieving an interference fit. The process is structured around two subprocesses: pick-and-place and insertion, which are further divided into five major steps: (1) Grasp (2) Lift (3) Place (4) Press, and (5) Roll, hence is termed H-GLPPR. Initially, the pick-and-place subprocess, which comprises of the Grasp, Lift, and Place steps, is completed for each piece of insulation. This is followed by the insertion subprocess, which

includes the Press and Roll steps, that is performed for all the insulation pieces in the same cavity. The following details each step in the process (Figure 3.2):

**Grasp:** The robot initiates the process by activating its end-effector to securely grasp the pre-cut batt insulation from an initialized position. This action requires precise control of the end-effector's gripper closure ( $l_c$ ) to avoid material damage while ensuring a firm hold.

**Lift:** Once securely grasped, the insulation is lifted from the initialized position. This step is crucial to maintaining stability and preventing further deformation of the insulation under gravitational forces. The grasp location ( $x_g$ ) on the insulation is carefully considered to minimize drooping.

**Place:** The robot maneuvers the insulation so its center point aligns with the longitudinal center axis of the designated cavity of the wood frame. It then positions the insulation atop the wood frame, ensuring correct alignment for the subsequent steps.

**Press:** The robot gently presses the insulation's edges into the cavity. Even if the wood frame is slightly non-straight, this step helps properly constrain the insulation within the cavity. This step considers the top-bottom clearance ( $c_{tb}$ ), side clearance ( $c_s$ ), pressing depth ( $d_p$ ), tilt angle ( $\varphi$ ), and interval ( $i$ ) to ensure the insulation's edges insert snugly without robotic collision or excessive compression.

**Roll:** Finally, the end-effector performs a rolling operation which takes into consideration the rolling depth ( $d_r$ ) and rolling path, in order to smooth out the insulation within the frame cavity. This step eliminates any trapped air pockets and ensures uniformity of the installed insulation.

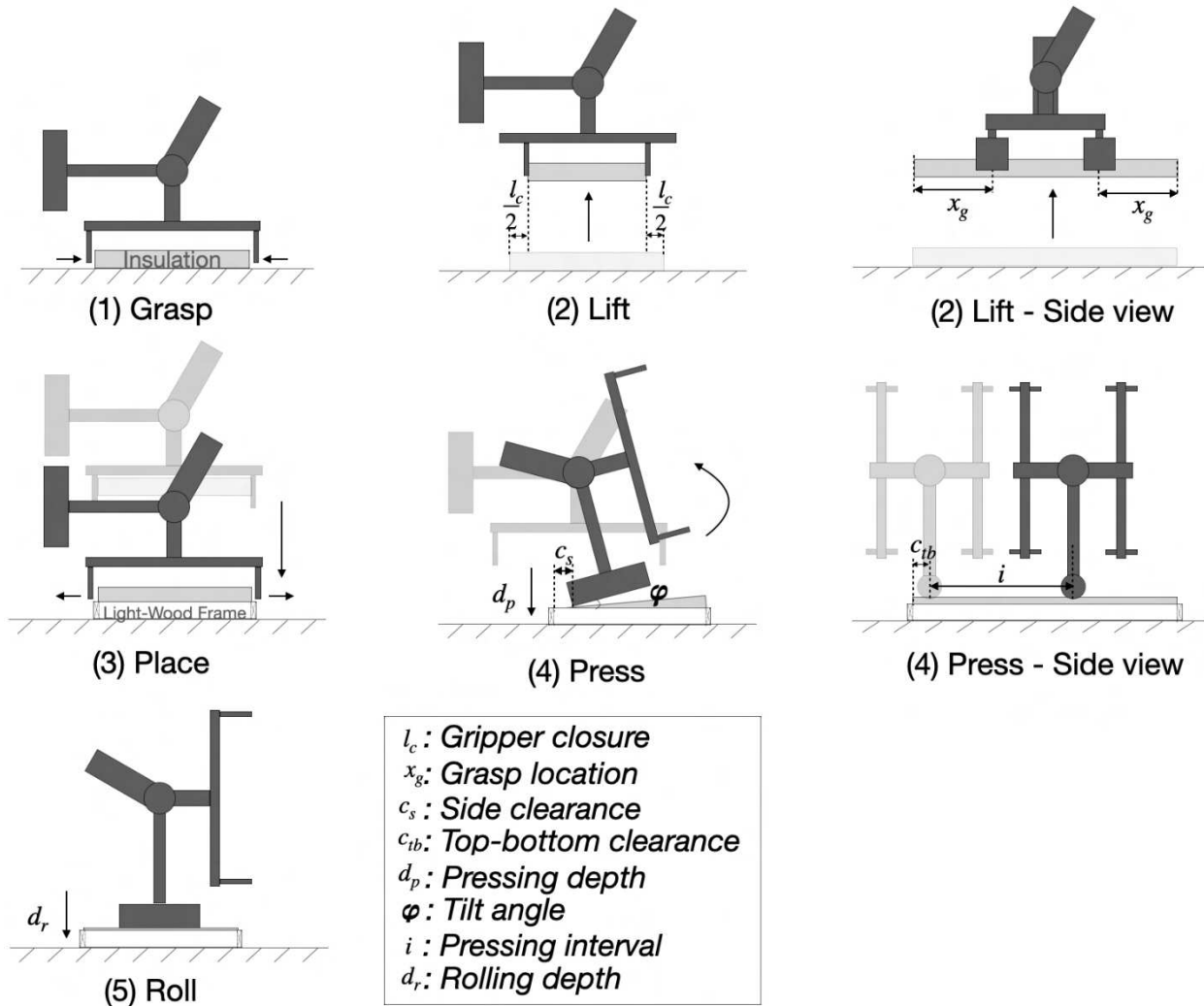


Figure 3.2: H-GLPPR process

### 3.1.2 End-Effector Design

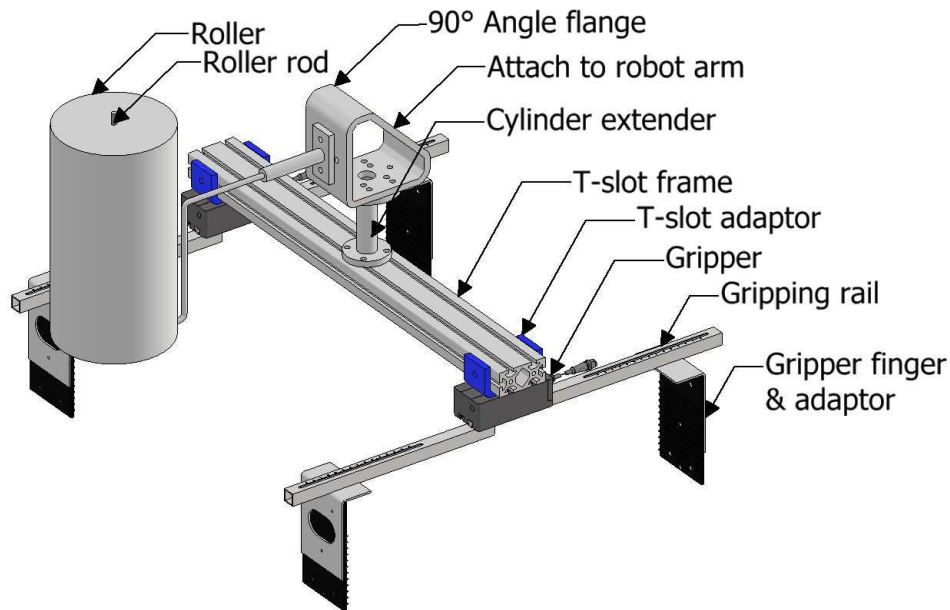
The proposed end-effector for the H-GLPPR process consists of two robot tools: a dual parallel gripper assembly and a roller assembly, as illustrated in Figure 3.3.

The dual parallel gripper assembly is utilized during pick-and-place subprocess. The parallel grippers are off-the-shelf products enhanced with custom-built gripping fingers. The selected electric parallel grippers are from Zimmer Group, featuring a maximum stroke length of 4.72 inches (120 mm), providing sufficient range to securely grasp the insulation materials. The gripper fingers, inspired by the fingers developed in V-GLITPP method, measure 4 by 7 inches (102 x 178 mm) with a thickness of 3/16-inch (4.76 mm), and are fabricated using 3D printing

technology. These fingers are crucial for the subprocess, featuring a textured inner surface at the lower section that increases gripping friction to ensure a secure and effective grip. The gripper finger adaptors provide rigid support and enable the fingers to be mounted onto the gripping rails which are equipped with ticks for easy position adjustment. This setup offers a material width handling range of 14 to 28 inches (356 to 711 mm), accommodating various insulation widths without the need for longer stroke grippers. The grippers are mounted onto a 30-inch (762 mm) long T-slot frame via T-slot adaptors, allowing movement along the T-slot frame to target specific grasp locations of the insulation. The entire gripper assembly is mounted onto a cylinder extender to ensure adequate clearance and avoid interference with the roller. This gripper assembly is highly flexible and adaptive to a range of insulation sizes.

The roller set is utilized during the insertion subprocess to minimize friction, sticking, and snagging when rolling the insulation. The roller, with a 3-3/8 inches (85.7 mm) radius, is designed to account for insulation deformation, ensuring that the central roller rod does not collide with the insulation or the wood frame during pressing and rolling actions.

The final assembly is completed with a custom-designed 90-degree angle flange, serving as the dual tool mount adaptor, to affix both the gripper assembly and roller assembly onto the end of the robot arm, facilitating an integrated multi-purpose system.



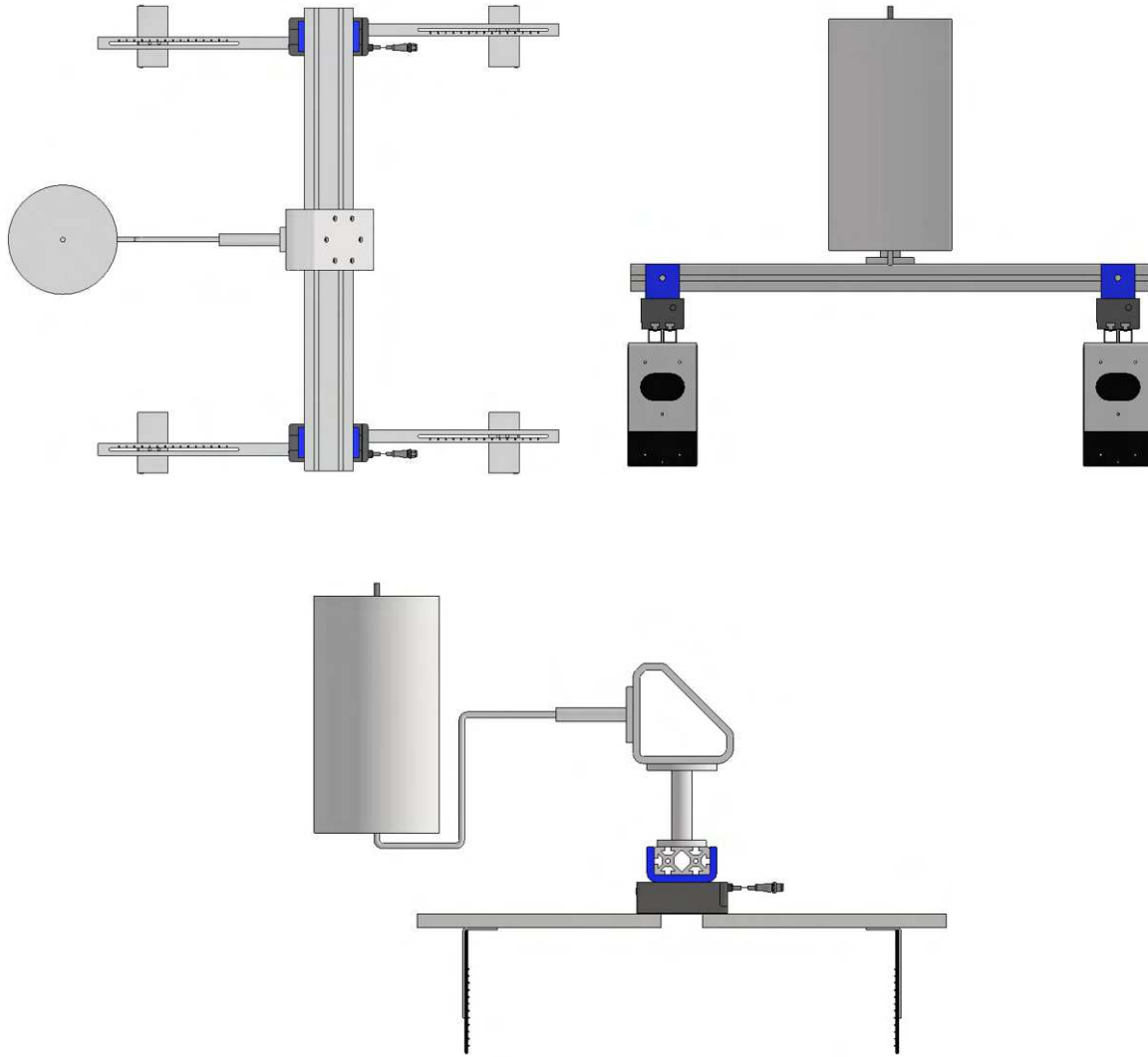


*Figure 3.3: End-effector design in isometric, top, side, front views*

### **3.1.3 In-lab Robotic Cell Setup**

As illustrated in Figure 3.4, a Universal Robot UR20 was utilized as the robotic arm, mounted on a standalone platform. The UR20 is a six degrees of freedom robot arm, capable of handling payloads up to 44.1 lbs (20 kg). It operates at a maximum speed of 78.7 in/s (2000 mm/s) and has a maximum reach of 68.9 inches (1750 mm). The working platform was a custom-built, L-shaped table with a flat surface, designed for facilitating the entire insulation installation process. The lines drawn on the table's surface serve as referencing datums for insulation pickup, while wood frame acts as datums for insulation installation, which

geometrically link the physical setup with the digital simulation. The prototyped end-effector, detailed in Subsection 3.1.4, was attached to the sixth axis of the UR20.

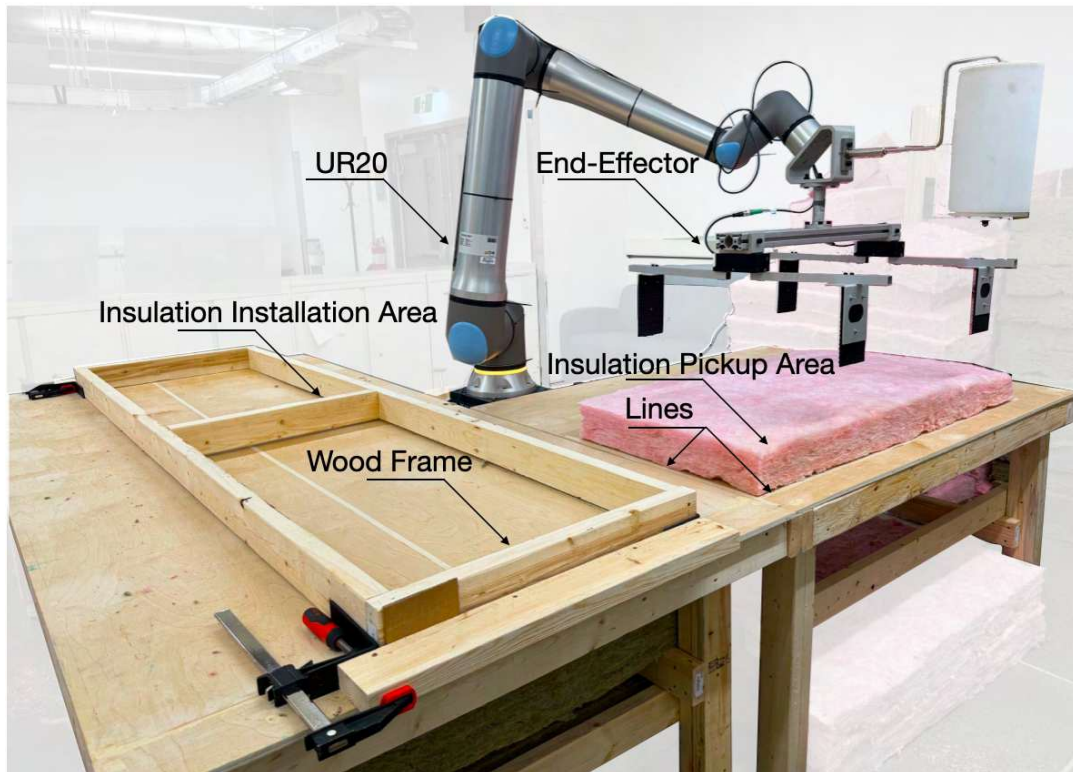


*Figure 3.4: In-lab robotic cell setup*

### **3.1.4 End-effector Prototype**

The end-effector prototype, as illustrated in Figure 3.5, was specifically developed for this robotic setup. Detailed specifications of its main components are listed in Table 3.1. These components not only follow the guidelines established in Subsection 3.1.2 on End-effector Design, but are also engineered to minimize weight. This was achieved by selecting lightweight materials such as aluminum alloy, incorporating weight-saving features in the CNC machined adaptors, and choosing other lightweight parts to comply with the payload limitations of the UR20. The overall weight of this prototype is 20.25 lbs (9.2 kg).

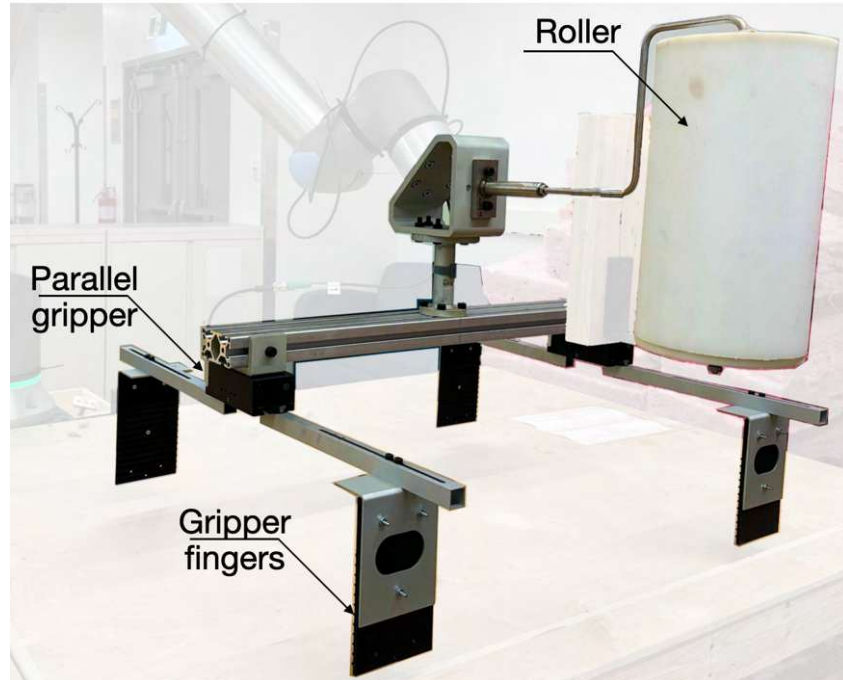


Figure 3.5: End-effector prototype

Table 3.1: Specifications of the end-effector prototype

Component	QTY	Material	Dimension [in (mm)]	Weight [lbs (kg)]	Specifications
Parallel gripper	2	-	-	1.78 (0.8)	<ul style="list-style-type: none"> <li>Manufacturer: Zimmer Group</li> <li>Model: GEH6060IL-03-B</li> <li>Type: Electric</li> <li>Stroke per finger: 2.36 in (60 mm)</li> <li>Gripping force: 22.5 – 225 lbf (100N -1000N)</li> </ul>
Gripping finger	4	PLA	W: 4 (102) L: 7 (178) T: 3/16	0.13 (0.06)	3D printed

---

			(4.76)		
Roller	1	PP	R: 3-3/8 (85.7)	2.42 (1.1)	CNC machined
			L: 12-1/2 (318)		
Gripping finger adaptor	4	Al Alloy	-	0.27 (0.12)	CNC machined
Gripping rail	4	Al Alloy	-	0.18 (0.08)	CNC machined
T-slot frame	1	Al Alloy	H: 3.15 (80) W: 1.57 (40) L: 30 (762)	5.72 (2.6)	• Rail profile: Hollow; Double
T-slot adaptor	2	Al Alloy	-	0.53 (0.24)	CNC machined
Cylinder extender	1	Al Alloy	-	0.77 (0.35)	CNC machined
Roller rod	1	SS	-	1.76 (0.8)	CNC machined
90° angle flange	1	Al Alloy	Angle: 90°	2.64 (1.2)	CNC machined

---

### 3.1.5 Parameter Results

The H-GLPPR process is governed by six key parameters, which are previously defined in Subsection 3.1.1 on the Installation Process: grasp location ( $\mathbf{x}_g$ ), gripper closure ( $l_c$ ), clearance ( $\mathbf{c}$ ), rolling depth ( $\mathbf{d}_r$ ), pressing depth ( $\mathbf{d}_p$ ) and tilt angle ( $\varphi$ ), and pressing interval ( $\mathbf{i}$ ). These parameter values were determined through a series of individual robotic trials. The trials utilized two types of batt insulation representing the extremes in terms of both weight and dimensions: Type A, the lightest, is fiberglass insulation measuring 15 by 3.5 inches (381 by 89 mm) and

Type B, the heaviest, is mineral wool insulation measuring 23 by 5.5 inches (584 by 140 mm). Both types are of a standard 47-inch (1194 mm) length, as packaged. For each type of insulation, three trials were conducted to determine the values for each parameter, and only a parameter value that completed all three trials was considered successful. After iterating these trials to identify a set of feasible parameter values, they were unified to formalize and illustrate the complete robotic installation process. The results of this unification are presented in Section 3.2 on Validation.

### 3.1.5.1 Grasp location ( $x_g$ )

To determine the optimal grasp locations of batt insulation during pickup, we consulted the adapted Euler-Bernoulli beam theory, traditionally applied to predict deflection in rigid beams. Considering the deformability of batt insulation, applying this theory to non-rigid and semi-rigid objects is unconventional. However, for the purposes of robotic manipulation, which involves pickup without damaging the insulation and effective trajectory planning, it is critical to minimize deflection. Therefore, approximating the insulation as a rigid beam provides a useful initial estimate of relative deflection, without knowing the mechanical properties and using complicated FEA modeling.

In our model, the pickup of insulation using two parallel grippers is conceptualized as an overhanging beam, uniformly loaded and symmetrically supported at both ends, as illustrated in Figure 3.6. We derived an expression for deflection occurs at the ends,  $\Delta_{ends}$  (in Eq.2) and at the midpoint between supports,  $\Delta_{mid}$  (in Eq.3). In these equations,  $\frac{wL^4}{EI}$  represents a normalizing term comprising of the self-weight per unit length ( $w$ ) multiplied by quadruple the length of the insulation ( $L^4$ ), divided by Young's modulus ( $E$ ) and moment of inertia ( $I$ ), which are assumed consistent throughout the entire piece of the batt insulation to justify the use of beam theory. We define the variable  $x_g$  to represent, as a percentage of  $L$ , the distance from the end of the insulation to the grasp location. Minimum deflection throughout the entire beam, is achieved when  $\Delta_{ends}$  is equal to  $\Delta_{mid}$ . After solving the equations and isolating for  $x_g$ , we obtained a value of approximately 0.22, suggesting that the grippers should be positioned at 0.22 times the length of the batt insulation from both ends.

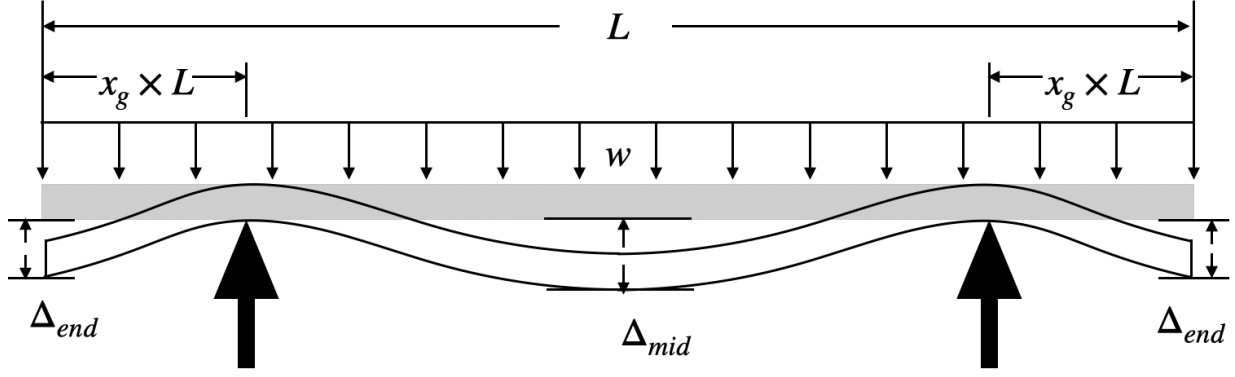


Figure 3.6: Overhanging beam with uniform load and symmetrical end supports

$$\Delta_{ends} = \frac{wL^4}{EI} * \frac{(x_g^4 + 6x_g^3 - 6x_g^2 + x_g)}{24} \quad (Eq. 2)$$

$$\Delta_{mid} = \frac{wL^4}{EI} * \frac{(16x_g^4 + 64x_g^3 - 96x_g^2 + 40x_g - 5)}{384} \quad (Eq. 3)$$

This theoretical approach was then validated through experimental tests, which confirmed the predicted deflection behavior of the insulation and the effectiveness of the identified grasp locations to minimize drooping.

Table 3.2: Grasp location validation with success rate

$x_g$	Success Rate:		Failure Mode
	Type A	Type B	
0.22	3/3	3/3	N/A

### 3.1.5.2 Gripper closure ( $l_c$ )

For consistency, we define the gripper closure in terms of the deformation caused to the insulation rather than the absolute displacement of the gripper. As a result, the gripper closure can be described as the difference between the insulation's original form and the compressed state after gripper closure. We have conducted extensive testing of gripper closure settings across eight different configurations of batt insulation, instead of focusing on just two extreme cases.

By iteratively varying the gripper closure values on the batts and assessing both grip efficacy and material condition, we obtained a dataset of gripper closure settings for our end-effector. These settings are detailed in Table 3.3.

*Table 3.3: Gripper closure for various insulation types and sizes*

<b>Batt Insulation Type</b>	<b>Insulation Size (W x T) [in (mm)]</b>	<b><math>l_c</math> [in (mm)]</b>	<b>Success Rate</b>
Mineral Wool	15 x 3.5 (381 x 89)	1-5/8 (40)	3/3
Mineral Wool	15 x 5.5 (381 x 140)	1 (25)	3/3
Mineral Wool	23 x 3.5 (584 x 89)	1-3/4 (45)	3/3
Mineral Wool	23 x 5.5 (584 x 140)	1-3/8 (35)	3/3
Fiberglass	15 x 3.5 (381 x 89)	3 (75)	3/3
Fiberglass	15 x 5.5 (381 x 140)	1-3/4 (45)	3/3
Fiberglass	23 x 3.5 (584 x 89)	4-3/4 (120)	3/3
Fiberglass	23 x 5.5 (584 x 140)	3-3/4 (95)	3/3

Note: All gripper closure measurements were initially obtained in millimeter. The values in inches were rounded from millimeters to the nearest 1/8 inch.

### 3.1.5.3 Clearance ( $c$ )

Clearances are critical for preventing collisions between the roller and the wood frame during the insulation insertion process, at the top-bottom( $c_{tb}$ ) and side( $c_s$ ) positions. In our experimental trials, we tested top-bottom clearances of 0, 0.5, and 1 inch (0, 12.7, and 25.4 mm) and side clearances of 0.5, 1 and 1.5 inches (12.7, 25.4 and 38.1 mm), as presented in Table 3.4 and Table 3.5. Our findings indicated that a top-bottom clearance of 0.5 inches (12.7 mm) is optimal, while a slightly larger side clearance of 1 inch (25.4 mm) is necessary. The increased side clearance is required due to cumulative effects of deviations from straightness in longer length of wood studs. Smaller clearances, such as 0 inches (0 mm) for top-bottom and 0.5 inches (12.7 mm) for side, frequently resulted in collisions, due to these deviations of the studs from straightness and tolerances of the roller. Conversely, clearance of 1 inch (25.4 mm) for top-bottom and 1.5 inches (38.1mm) for side were found to be excessive, resulting in edges lifting up that led to insufficient insertion of the insulation.

Table 3.4: A list of trialed top-bottom clearance with success rate

$c_{tb}$ [in (mm)]	Success Rate: Type A	Success Rate: Type B	Failure Mode
0 (0)	0/3	0/3	Collision between roller and frame
0.5 (12.7)	3/3	3/3	N/A
1 (25.4)	1/3	2/3	Insufficient insertion

Table 3.5: A list of trialed side clearance with success rate

$c_s$ [in (mm)]	Success Rate: Type A	Success Rate: Type B	Failure Mode
0.5 (12.7)	0/3	0/3	Collision between roller and frame
1 (25.4)	3/3	3/3	N/A
1.5 (38.1)	1/3	3/3	Insufficient insertion for Type A Insulation

#### 3.1.5.4 Rolling depth ( $d_r$ )

The rolling depth is defined as the distance the roller travels below the frame’s surface to smoothly roll the insulation into the cavity, ensuring that there are no gaps and unwanted deformation that could potentially reduce the effective R-value of the insulation. In our trials, we tested rolling depths of 0, 0.75, and 1.5 inches (0, 19.1, and 38.1 mm), which are listed in Table 3.6. A depth of 0.75 inch (19.1 mm) was found to consistently roll both fiberglass and mineral wool insulation into the frame cavity, however, it was insufficient along the edges. This later led to the introduction of a pressing step, detailed in Subsubsection 3.1.5.5 and 3.1.5.6, for the proper insertion of the edges. At a depth of 0 inches (0 mm), the roller’s inadequate depth resulted in only partial insertion of the insulation body, not just the edges, leaving noticeable gaps within the frame cavity. Conversely, a depth of 1.5 inches (38.1 mm) led to interference between the roller and the insulation. This excessive depth caused the roller to embed too deeply, constraining its ability to move smoothly along the insulation’s surface, which led to catching and compressing the insulation. Such over-compression not only caused fracture in the fibrous structure leading to permanent deformation but also obstructed effective rolling.

Table 3.6: A list of trialed rolling depth with success rate

$d_r$ [in (mm)]	Success Rate: Type A	Success Rate: Type B	Failure Mode
0 (0)	2/3	0/3	Only partial insulations were inserted
0.75 (19.1)	3/3	3/3	N/A, but insufficient insertion along the edges
1.5 (38.1)	2/3	0/3	Interference between the roller and insulations

### 3.1.5.5 Pressing depth ( $d_p$ ) and Tilt angle ( $\varphi$ )

The introduction of tilt angles in conjunction with the pressing depth, prior to rolling, is essential to overcome the insufficiency of solely the rolling step when it comes to the edges. The tilt angle is defined as the angle between the roller's longitudinal axis and the insulation surface. Similarly, the pressing depth is the distance the roller travels below the frame's surface to press the insulation's edge flush into the cavity. In our trials, pressing depths of 0.75 inches (19.1 mm) and 1 inch (25.4 mm) were evaluated, in combination with tilt angles of 15 degrees and 30 degrees. The combination of a 1-inch (25.4 mm) depth with a 15-degree tilt angle consistently pressed the edges of both fiberglass and mineral wool insulation fully into the frame cavity. However, a depth of 0.75 inches (19.1 mm), although optimal for the main body of the insulation during the rolling phase, was less effective at the edges regardless of the tilt angle used, particularly for mineral wool. This ineffectiveness is due to its higher density and fiber rigidity, which resist compression under the applied press. Conversely, any combination involving a 30-degree tilt angle diminished effective side clearance, which is intended to accommodate the slight non-straightness of the studs, and led to collision between the roller and the frame. The obtained results are detailed in Table 3.7.

Table 3.7: A list of trialed combination of pressing depth and tile angle with success rate

$d_p$ [in (mm)]	$\varphi$ [°]	Success Rate: Type A	Success Rate: Type B	Failure Mode
0.75 (19.1)	15	3/3	0/3	Insufficient insertion for Type B
0.75 (19.1)	30	0/3	0/3	Collision between the roller and frame
1 (25.4)	15	3/3	3/3	N/A

1 (25.4)	30	0/3	0/3	Collision between the roller and frame
----------	----	-----	-----	--

### 3.1.5.6 Pressing interval ( $i$ )

The pressing interval specifies the locations along the insulation’s longitudinal edges where the roller applies pressure, ensuring that no insulation edges remain uninserted after rolling. Although there are no limits on the number of presses, minimizing the press count shortens insulation installation time. In our trials, the center-to-center distance of the pressing interval were tested at 20, 15, and 10 inches (508, 381, and 254 mm), starting from the bottom of the frame and concluding at the top, and also including a press at the junction between insulation pieces. It was observed that a 10-inch (254 mm) pressing interval ensures complete insertion of the insulation’s edge into the frame cavity, without any noticeable convexity after rolling. In contrast, intervals of 20-inch (508 mm) and 15-inch (381 mm) resulted in visible convexities between the press points along the edges, indicating inadequate coverage application. The results are shown in Table 3.8.

*Table 3.8: A list of trialed pressing interval with success rate*

$i$ [in (mm)]	Success Rate:		Failure Mode
	Type A	Type B	
20 (508)	0/3	1/3	Visible convexities along the edges
15 (381)	1/3	3/3	Visible convexities along the edges for Type A
10 (254)	3/3	3/3	N/A

### 3.1.6 Robot Simulation and Control

An offline programming was developed within a digital twin environment implemented in RoboDK, as shown in Figure 3.7, to enable virtual testing of interaction before physical implementation. The offline program automates the calculation of the target points and the generation of the toolpath. As detailed in Algorithm 1, a series of target points for pick-and-place and insertion tasks are calculated in relation to the robot’s tool center points (TCPs). These target points are fundamental for the subsequent generation of the robotic toolpath, as executed Algorithm 2. The TCP of the dual gripper assembly is located at the midpoint between the two grippers and is flush with the bottom of the gripper fingers. Meanwhile, the TCP for the roller assembly is centrally located on the roller.

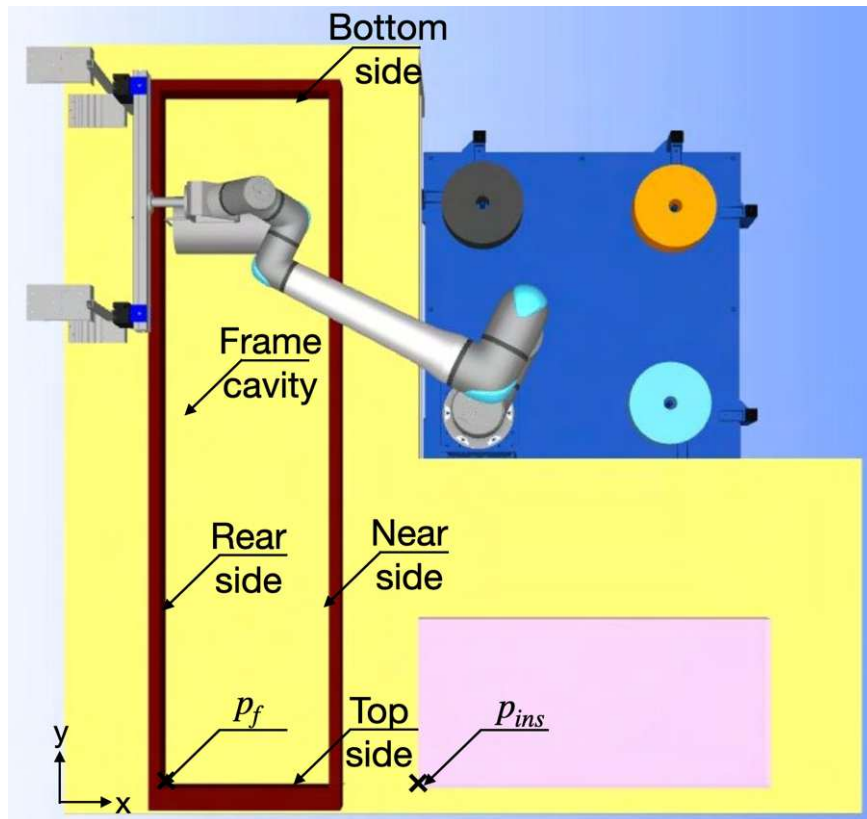
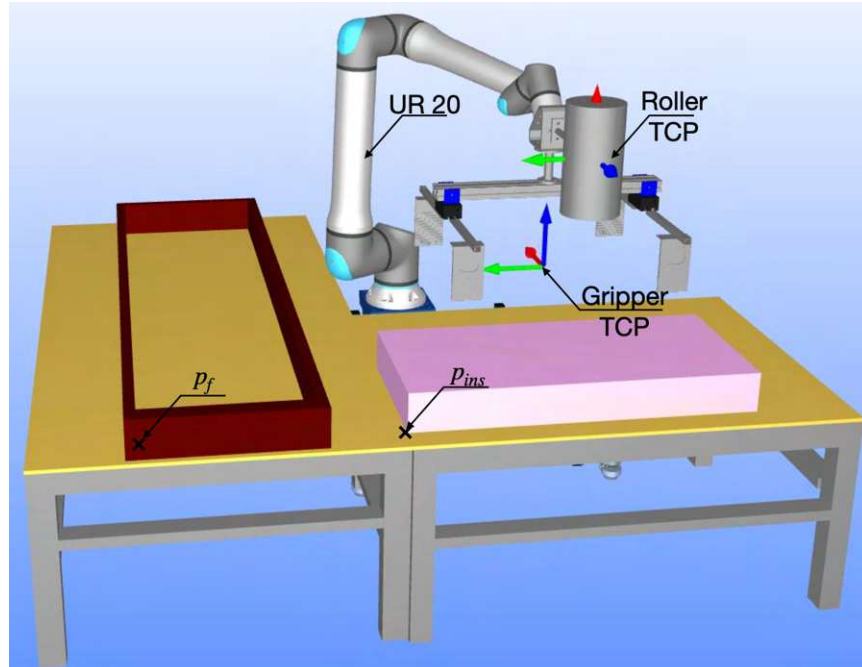


Figure 3.7: RoboDK robotic cell setup in isometric view (1<sup>st</sup>) and top view (2<sup>nd</sup>)

Algorithm 1 shows the calculation of all the target points. The pick-and-place subprocess aligns each insulation's center point with the wood frame's longitudinal center axis. The grasp

point ( $p_{grasp}$ ) for each insulation is set above the table to allow clearance for the grippers. Placement point coordinates ( $p_{place}$ ) are calculated by adding its mid-length to the cumulative lengths of previously placed insulations. Additionally, an intermediate point ( $p_{inter}$ ) in the toolpath is explicitly specified to avoid collisions during the movement of insulation. For the insertion subprocess, pressing and rolling steps are set along both longitudinal edges of the frame, categorized into ‘rear’ and ‘near’ press points, as well as ‘rear’, ‘mid’, and ‘near’ rolling points. The pressing point ( $p_{press}$ ) and rolling point ( $p_{roll}$ ) are determined by the roller’s radius, frame dimensions, and various parameters as outlined in Subsection 3.1.5. When multiple insulations are inserted into one frame cavity, precise pressing at joint points is required to ensure proper alignment. Each target point has an associated approach/departure point ( $p_{app\_}$ ), which elevates the end-effector to a designated height to prevent collisions and ensure smooth operational flow.

*Algorithm 1: target\_points\_calculation*

---

Input:

$I = (I_w, I_l, I_t)$ : list of insulation, insulation width, length, thickness

$(F_w, F_l, F_t)$ : frame cavity width, length, thickness

$p_{ins} = (p_{ins_x}, p_{ins_y}, 0)$ : origin of the insulation relative to the world frame

$p_f = (p_{f_x}, p_{f_y}, 0)$ : origin of the frame relative to the world frame

$(R_\phi, R_l)$ : roller diameter, length

$h$ : height increment for approaching and departing from the target point

$a$ : clearance between gripper fingers and the table or frame

parameters that identified in the Section 4.2

Output:

$p$ : list of target points

---

1: # calculate target points for pick-and-place task

2: **for each** insulation in  $I$  **do**

3:  $p_{grasp} = p_{ins} + (\frac{I_l}{2}, \frac{I_w}{2}, a)$

4:  $p_{app\_grasp} = p_{grasp} + (0, 0, h)$

```

5:   $p_{inter} = p_{app\_grasp} + \left( \frac{p_{insx} - p_{fx}}{2}, \frac{p_{insy} - p_{fy}}{2}, 0 \right)$ 
6:   $p_{place} = p_f + \left( \frac{F_w}{2}, \sum_{j=1}^l I_{lj} + \frac{I_l}{2}, F_t + a \right)$ 
7:   $p_{app\_place} = p_{place} + (0, 0, h)$ 
8:  end for
9:  # calculate target points for insertion task
10:  $\Delta_{x\_press} = \{ 'rear': p_{fx} + \left( \frac{\sqrt{R_l^2 + R_\phi^2}}{2} \right) * \cos \left[ \tan^{-1} \left( \frac{R_\phi}{R_l} \right) + \varphi \right] + c_s,$ 
     $'near': p_{fx} + F_w - \left( \frac{\sqrt{R_l^2 + R_\phi^2}}{2} \right) * \cos \left[ \tan^{-1} \left( \frac{R_\phi}{R_l} \right) + \varphi \right] - c_s \}$ 
11:  $\Delta_y = \{ 'top': p_{fy} + \left( \frac{R_\phi}{2} + c_{tb} \right), 'bottom': p_{fy} + F_l - \left( \frac{R_\phi}{2} + c_{tb} \right) \}$ 
12:  $\Delta_{z\_press} = F_t - d_p + \left( \frac{\sqrt{R_l^2 + R_\phi^2}}{2} \right) * \sin \left[ \tan^{-1} \left( \frac{R_\phi}{R_l} \right) + \varphi \right]$ 
13:  $roty = \{ 'rear': \varphi, 'near': -\varphi \}$ 
14: for each name in  $\Delta_{x\_press}$  do
15:   $p_{press\_y\_value} = \Delta_{y\_top}$ 
16:   $m == 1$ 
17:  while  $p_{press\_y\_value} < \Delta_{y\_bottom}$ 
18:     $p_{press\_y\_m} = p_{press\_y\_value}$ 
19:     $p_{press_{[\Delta_{x\_press\_name}]_m}} = [p_f + (\Delta_{x\_press}[\Delta_{x\_press\_name}], p_{press\_y\_m}, \Delta_{z\_press})] *$ 
     $roty_{name}$ 
20:     $p_{app\_press_{[\Delta_{x\_roll\_name}]_m}} = p_{press_{[\Delta_{x\_press\_name}]_m}} + (0, 0, h)$ 
21:     $p_{press\_y\_value} += i$ 
22:    if  $\sum_{j=1}^l I_{lj} < p_{press\_y\_value} \leq \sum_{j=1}^l I_{lj} + i$ 
23:       $p_{press\_y\_value} = \sum_{j=1}^l I_{lj}$ 
24:       $m += 1$ 
25:    if  $p_{press\_y\_value} \neq \Delta_{y\_bottom}$ 
26:       $p_{press_{[\Delta_{x\_press\_name}]_m}} = p_f + (\Delta_{x\_press}[\Delta_{x\_press\_name}], \Delta_{y\_bottom}, \Delta_{z\_press})$ 

```

```

27:    $p_{app\_press[\Delta x\_press\_name].m} = p_{press[\Delta x\_press\_name].m} + (0,0,h)$ 
28: end for
29:  $\Delta_{x\_roll} = \{ 'rear': p_{fx} + (\frac{R_l}{2} + c_s), 'mid': p_{fx} + \frac{F_w}{2}, 'near': p_{fx} + F_w - (\frac{R_l}{2} + c_s) \}$ 
30:  $\Delta_{z\_roll} = F_t - d_r + \frac{R_l}{2}$ 
31: for each  $\Delta_{x\_roll\_name}$  do
32:   for each  $\Delta_{y\_name}$  do
33:      $p_{roll[\Delta_{x\_roll\_name}][\Delta_{y\_name}]} = p_f + (\Delta_{x\_roll}[\Delta_{x\_roll\_name}], \Delta_y[\Delta_{y\_name}], \Delta_{z\_roll})$ 
34:      $p_{app\_roll[\Delta_{x\_roll\_name}][\Delta_{y\_name}]} = p_{roll[\Delta_{x\_roll\_name}][\Delta_{y\_name}]} + (0,0,h)$ 
35:   end for
36: end for
37:  $p = p_{grasp} + p_{app\_grasp} + p_{inter} + p_{place} + p_{app\_place} + p_{press} + p_{app\_press} + p_{roll}$ 
    $+ p_{app\_roll}$ 
38: return  $p$ 

```

---

Algorithm 2 outlines the toolpath for the H-GLPPR process. Initially, it sets the dual gripper assembly as the active tool with collision detection enabled to ensure that no collisions occur during the pick-and-place subprocess. For the insertion subprocess, it switches the active tool to the roller assembly with collision detection disabled, as the simulation does not model insulation deformation, which could lead to false collision signals. The specifically designed parameters that is discussed in Subsection 3.1.5 mitigate the need for collision detection in the digital twin environment, ensuring that no collisions occur in the actual robot operation.

The toolpath is generated from the defined target points, employing point-to-point motion (*MoveJ*) for transitions where the exact path of the end-effector is less critical. This approach is time-efficient, such as in movement from the home position to the approach grasp point ( $p_{app\_grasp}$ ). Meanwhile, linear motion (*MoveL*) is utilized when the end-effector must follow a precise linear path, especially near fixed objects. Here, precise path control is crucial to avoid collisions and ensure the success of the task, such as when moving from the approach grasp point ( $p_{app\_grasp}$ ) to the grasp point ( $p_{grasp}$ ) and then returning to the approach grasp point ( $p_{app\_grasp}$ ). For the pressing step, the toolpath is generated by sequentially pressing target points ( $p_{press}$ ) from the bottom to the top of both the rear and near sides of the wood frames. Similarly,

the toolpath for the rolling step involves rolling from the bottom to the top of the frame. The number of the rolling paths depends on the ratio of the frame cavity width to the roller length. If this ratio equals 1, rolling occurs only from the center longitudinal axis of the frame. If the ratio exceeds 1, rolling is required along the rear and near sides.

*Algorithm 2: toolpath\_generation*

---

Input:

*target\_points\_calculation*: inputs, output and variables from Algorithm 1

Output:

*T*: H-GLPPR toolpath

---

- 1: # toolpath of pick-and-place task
- 2: set gripper as tool
- 3: set grippers open
- 4: set collision detection on
- 5: start from Home position
- 6: **for each** *I* **do**
- 7:   *MoveJ* ( $p_{app\_grasp}$ )
- 8:   *MoveL* ( $p_{grasp}$ )
- 9:   set grippers close
- 10:   *MoveL* ( $p_{app\_grasp}$ )
- 11:   *MoveJ* ( $p_{inter}$ )
- 12:   *MoveJ* ( $p_{app\_place}$ )
- 13:   *MoveL* ( $p_{place}$ )
- 14:   set grippers open
- 15:   *MoveL* ( $p_{app\_place}$ )
- 16: **end for**
- 17: # toolpath of pressing step
- 18: set roller as tool
- 19: *MoveJ* ( $p_{app\_press_{rear.m}}$ )
- 20: set collision detection off

```

21: for each name in  $\Delta_{x\_press}$ 
22: for  $n = 0,1 \dots m-1$  do
23:   MoveL ( $p_{app\_press[\Delta_{x\_press\_name}].(m-n)}$ )
24:   MoveL ( $p_{press[\Delta_{x\_press\_name}].(m-n)}$ )
25:   MoveL ( $p_{app\_press[\Delta_{x\_press\_name}].(m-n)}$ )
26: end for
27: end for
28: # toolpath of rolling step
29: Ratio between roller length and frame cavity width =  $\frac{F_w - 2 * c_s}{R_l}$ 
30: if Ratio between roller length and frame cavity width = 1:
31:    $\Delta_{x\_roll\_name} = \{ 'mid' \}$ 
32: if Ratio between roller length and frame cavity width > 1:
33:    $\Delta_{x\_roll\_name} = \{ 'rear', 'mid', 'near' \}$ 
34: for each  $\Delta_{x\_roll\_name}$  do
35:   MoveL ( $p_{app\_roll[\Delta_{x\_roll\_name}].[\Delta_{y\_bottom}]}$ )
36:   MoveL ( $p_{roll[\Delta_{x\_roll\_name}].[\Delta_{y\_bottom}]}$ )
37:   MoveL ( $p_{roll[\Delta_{x\_roll\_name}].[\Delta_{y\_top}]}$ )
38:   MoveL ( $p_{roll[\Delta_{x\_roll\_name}].[\Delta_{y\_bottom}]}$ )
39:   MoveL ( $p_{app\_roll[\Delta_{x\_roll\_name}].[\Delta_{y\_bottom}]}$ )
40: end for
41: set collision detection on
42: MoveJ to Home position
43: return T

```

---

These two algorithms simulate the H-GLPPR process and synchronize the various operations for different insulation pieces. This setup in digital twin environment facilitates a seamless transfer of commands from the robot simulation to the actual robot controller for installing the insulation into the wood frame.

## 3.2 Validation

The designed H-GLPPR process was validated using the parameters values selected in Subsection 3.1.5 and summarized in Table 3.9. Tests were conducted on both mineral wool and fiberglass batt insulations at the robot arm’s maximum linear speed of 78.7 in/s (2000 mm/s). These tests included five trials for each insulation configuration under three distinct scenarios. Each test used new insulation to simulate representative construction circumstances, accounting for the fact that insulation does not retain the same stiffness and shape after being used. Prior to the test, the simulation model and the actual robotic cell were calibrated using the reference datums on the table. This calibration significantly improved the accuracy of the installation process.

*Table 3.9: A list of obtained parameter results*

Parameter	Value
Grasp location ( $x_g$ )	22% from each end
Gripper closure ( $l_c$ )	Refer to Table 3.3
Side clearance ( $c_s$ )	1 in (25.4 mm)
Top-bottom clearance ( $c_{tb}$ )	0.5 in (12.7 mm)
Rolling depth ( $d_r$ )	0.75 in (19.1 mm)
Pressing depth ( $d_p$ )	1 in (25.4 mm)
Pressing tilt angle ( $\varphi$ )	15°
Pressing interval ( $i$ )	10 in (254 mm)

### 3.2.1 Overview

The experiment involved four wood frame specimens, each 8 feet (2438 mm) in length, featuring a total of eight cavity configurations. These frames were constructed with 2-by-4 and 2-by-6 SPF dimensional lumbers, including both 16 inches (406 mm) and 24 inches (610 mm) on-center stud spacing. The dimensions and stud spacings represent the four most common types of walls used in the building construction. It should be emphasized that based on the fiberglass insulation product installation guide [65], which recommends that the fiberglass overall length be half an inch longer than the frame cavity, this specification was applied to the last piece in each scenario involving fiberglass batt.

Three scenarios were designed to simulate actual configurations encountered in construction (illustrated in Figure 3.8):

Scenario 1 (S1): A single piece of insulation filled the entire 46-1/2 inches (1181 mm) length of the frame cavity, contacting all four sides of the wood frame. This setup provided insights into the frictional interactions in a fully constrained wall cavity.

Scenario 2 (S2): Two pieces of insulation were used in tandem to fill a 92-5/8 inches (2353 mm) frame cavity.

S2.1: The first piece contacted three sides of the wood frame, leaving one side free.

S2.2: The second piece contacted three sides of the wood frame and the free side of the previous piece.

Scenario 3 (S3): Similar to S2 but with an additional piece, three pieces of insulation filled a 92-5/8 inches (2353 mm) frame cavity:

S3.1: The first piece contacted three sides of the wood frame, leaving one side free.

S3.2: Then a middle piece contacted two sides of the wood frame, one side of the first piece of insulation, with one side remaining free.

S3.3: The last piece contacted three sides of the wood frame and the free side of the middle piece.

These scenarios provided a comprehensive coverage of the dynamic interactions and challenges involved in the robotic installation of batt insulation, emphasizing the system's adaptability to various construction configurations.

Detailed specifications of these frames and insulations were listed in Table 3.10 and Table 3.11.

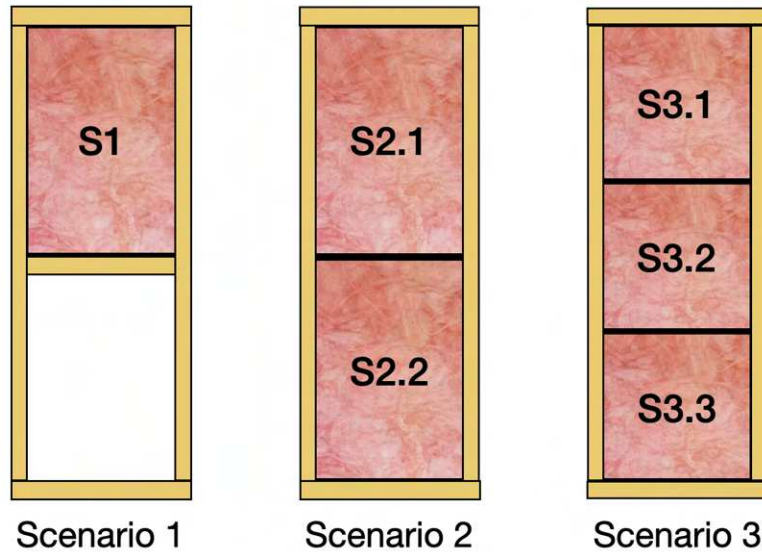


Figure 3.8: Three scenarios

Table 3.10: Specification of wall frames

Cavity (W x L x T) [in (mm)]	Lumber [in (mm)]	On-center Stud Spacing [in (mm)]	Scenarios	Insulation Size (W x T) [in (mm)]
14-1/2 x 46-1/2 x 3-1/2 (368 x 1181 x 89)	2x4 (51 x 102)	16 (406)	S1	15 x 3.5 (381 x 89)
14-1/2 x 92-5/8 x 3-1/2 (368 x 2353 x 89)	2x4 (51 x 102)	16 (406)	S2, S3	15 x 3.5 (381 x 89)
22-1/2 x 46-1/2 x 3-1/2 (572 x 1181 x 89)	2x4 (51 x 102)	24 (610)	S1	23 x 3.5 (584 x 89)
22-1/2 x 92-5/8 x 3-1/2 (572 x 2353 x 89)	2x4 (51 x 102)	24 (610)	S2, S3	23 x 3.5 (584 x 89)
14-1/2 x 46-1/2 x 5-1/2 (368 x 1181 x 140)	2x6 (51 x 152)	16 (406)	S1	15 x 5.5 (381 x 140)
14-1/2 x 92-5/8 x 5-1/2 (368 x 2353 x 140)	2x6 (51 x 152)	16 (406)	S2, S3	15 x 5.5 (381 x 140)
22-1/2 x 46-1/2 x 5-1/2 (572 x 1181 x 140)	2x6 (51 x 152)	24 (610)	S1	23 x 5.5 (584 x 140)
22-1/2 x 92-5/8 x 5-1/2 (572 x 2353 x 140)	2x6 (51 x 152)	24 (610)	S2, S3	23 x 5.5 (584 x 140)

Table 3.11: Insulation length for each scenario

Scenario	Fiberglass Insulation Length	Mineral Wool Insulation Length
	[in (mm)]	[in (mm)]
S1	47 (1194)	46-1/2 (1181)
S2.1	47 (1194)	47 (1194)
S2.2	46-1/8 (1172)	45-5/8 (1159)
S3.1	30-7/8 (784)	30-7/8 (784)
S3.2	30-7/8 (784)	30-7/8 (784)
S3.3	31-3/8 (797)	30-7/8 (784)

### 3.2.2 Results and Discussion

Table 3.12 summarizes the success rates for installing various types and sizes of batt insulation using the H-GLPPR process. Figure 3.9 and Figure 3.10 illustrate examples of the entire H-GLPPR process, showing the S1 experiment with 15 x 5.5-inch (381 x 140 mm) fiberglass insulation and the S2 experiment with 15 x 3.5-inch (381 x 89 mm) mineral wool insulation. Additional experiment figures are detailed in Appendix D.

Table 3.12: Experiment results for entire H-GLPPR process

Batt Insulation	Insulation Size	S1	S2	S3
Type	(W x T) [in (mm)]	Success Rate	Success Rate	Success Rate
Mineral Wool	15 x 3.5 (381 x 89)	5/5	5/5	5/5
Mineral Wool	15 x 5.5 (381 x 140)	5/5	5/5	5/5
Mineral Wool	23 x 3.5 (584 x 89)	5/5	5/5	5/5
Mineral Wool	23 x 5.5 (584 x 140)	5/5	5/5	5/5
Fiberglass	15 x 3.5 (381 x 89)	5/5	5/5	5/5
Fiberglass	15 x 5.5 (381 x 140)	5/5	5/5	5/5
Fiberglass	23 x 3.5 (584 x 89)	4/5	2/5	0/5
Fiberglass	23 x 5.5 (584 x 140)	5/5	5/5	5/5

As demonstrated, the overall success rate stands at 92.5%. All sizes of mineral wool achieved a perfect 100% success rate across all five trials in all three scenarios, proving the process's robustness in handling mineral wool insulation regardless of its dimensions.

Similarly, fiberglass insulation generally exhibited high success rates across most scenarios and sizes, except for 23 by 3.5 inches (584 by 89 mm) fiberglass insulation. This size encountered issues during the lifting step. The insulation often slipped from the gripper fingers, due to its comparatively higher width-to-thickness ratio compared to other fiberglass specimens, and reduced the rigidity compare to same sized mineral wool, making it easy to distort. Specifically, the zero success in S3 was attributed to the shorter length compared to S1 and S2, which led to a reduced second moment of area, impairing the insulation’s ability to resist bending. Consequently, when using the same gripper closure value coupled with the inertial forces during lifting, the insulation distorted more significantly and fell from the gripper fingers more easily. To address this, we implemented two independent modifications, each proving successful on its own. First, we adjusted the lifting linear speed from 78.7 in/s (2000 mm/s) to 9.84 in/s (250 mm/s), reducing the inertial forces and consequently the friction force required, as shown in Figure 3.11 for the S3 experiment. Second, we elevate the insulation by 1.5 inches (38.1 mm) from the table, positioning the insulation higher within the gripper fingers and enhancing the ribbed texture’s effectiveness in preventing slippage. Both modifications achieved a 100% success rate in subsequent trials.





*Figure 3.9: H-GLPPR process and completion with 15 x 5.5-inch (381 x 140 mm) fiberglass insulation size for Scenario 1 (Grasp 1st piece, Lift 1st piece, Place 1st piece, Press, Roll, Completion)*

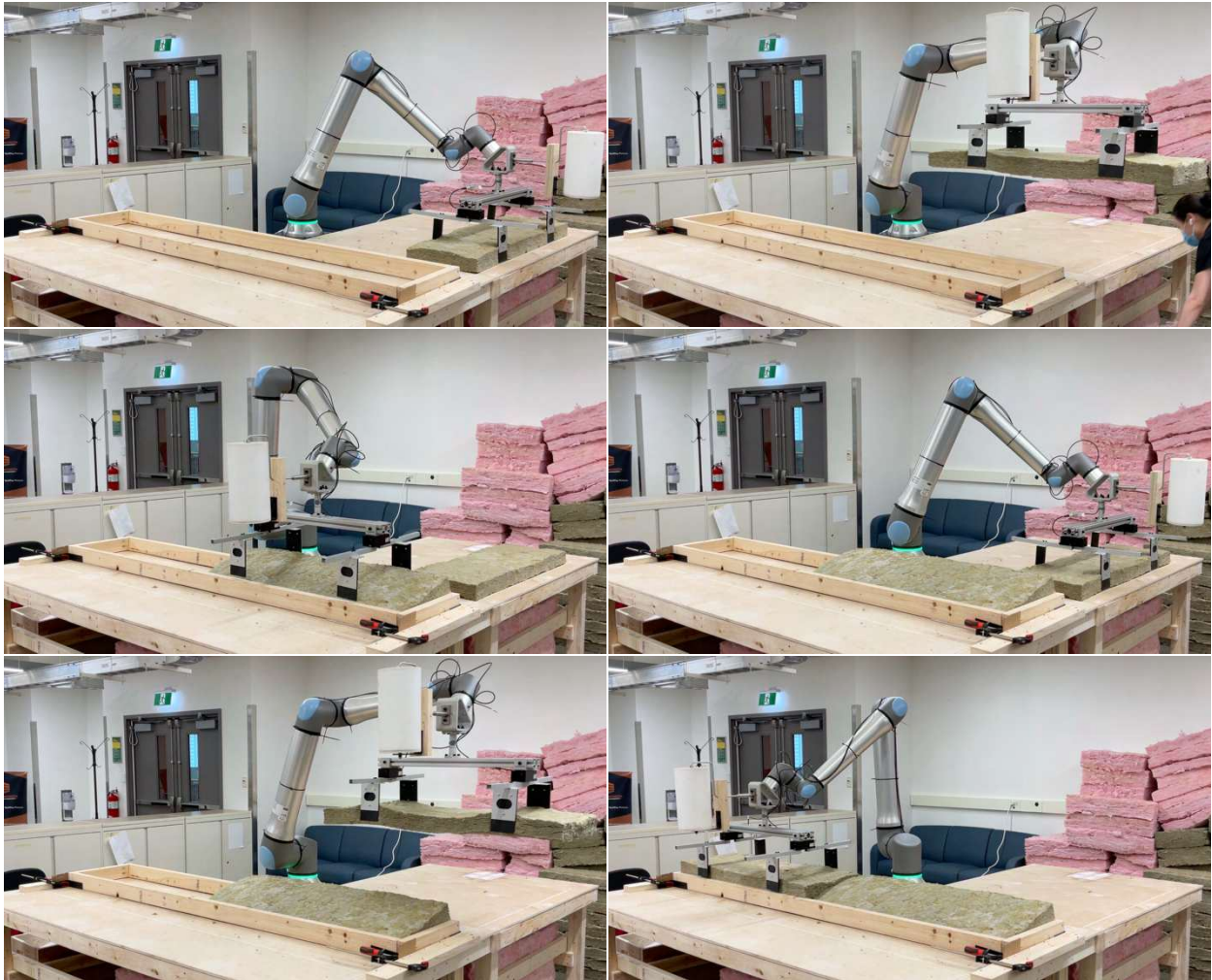




*Figure 3.10: H-GLPPR process and completion with 15 x 3.5-inch (381 x 89 mm) mineral wool insulation size for Scenario 2 (Grasp 1st piece, Lift 1st piece, Place 1st piece, Grasp 2nd piece, Lift 2nd piece, Place 2nd piece, Press, Roll, Completion)*



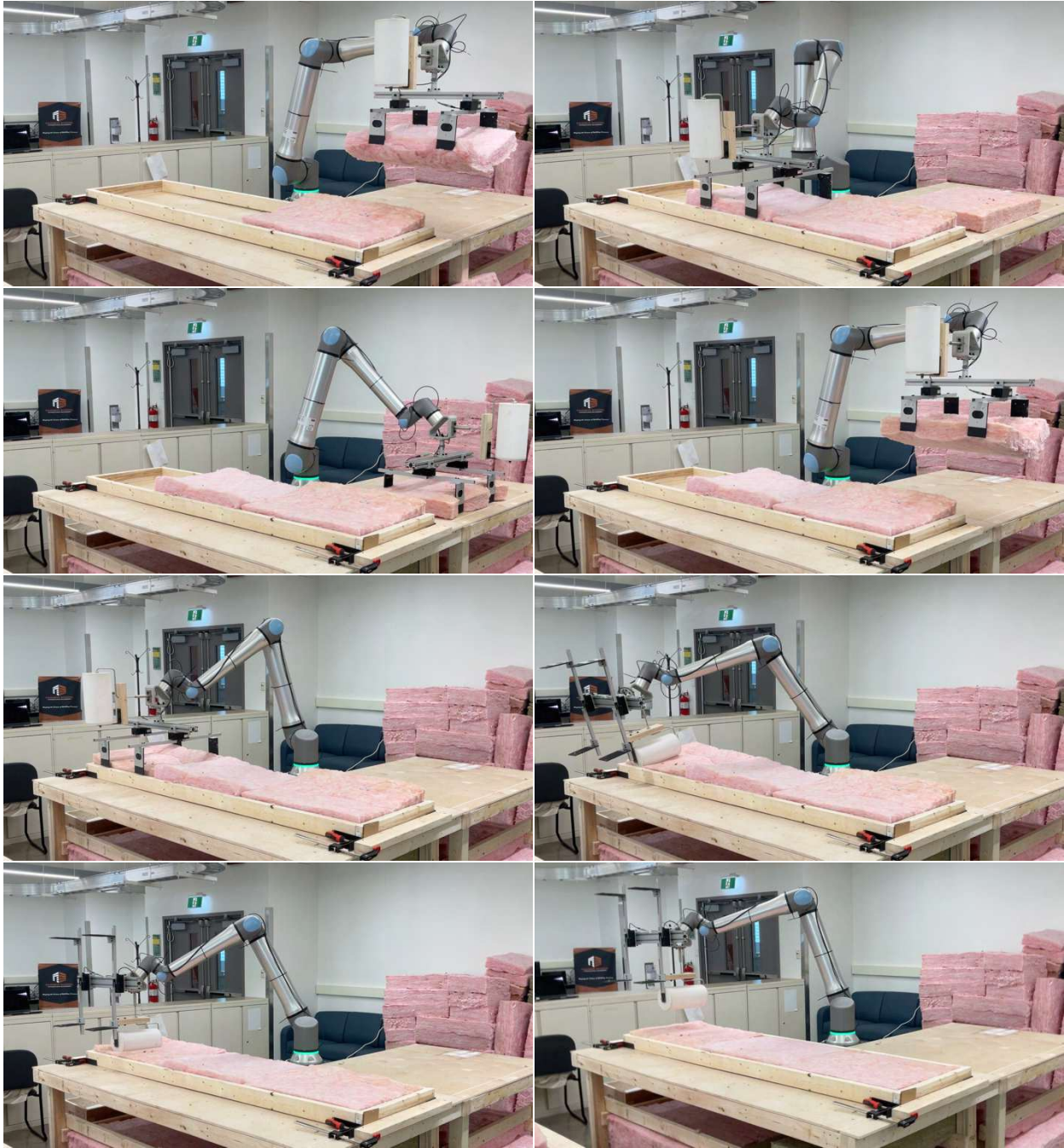


*Figure 3.11: H-GLPPR process and completion after modifying the lifting speed with 23 x 3.5-inch (584 x 89 mm) fiberglass insulation size for Scenario 3 (Grasp 1<sup>st</sup> piece, Lift 1<sup>st</sup> piece, Place 1<sup>st</sup> piece, Grasp 2<sup>nd</sup> piece, Lift 2<sup>nd</sup> piece, Place 2<sup>nd</sup> piece, Grasp 3<sup>rd</sup> piece, Lift 3<sup>rd</sup> piece, Place 3<sup>rd</sup> piece, Press, Roll, Completion)*

### 3.3 Chapter Conclusion

The initial design requirements, as outlined in the research objective and beginning of this chapter, included utilizing a single robot arm and the capability to insert batt insulation

initialized from the horizontal configuration. These criteria have been successfully met, as evidenced by the high success rates of 92.5%. The H-GLPPR process effectively mitigates the negative effects of deformation and uncertainties in mechanical properties, as well as avoids complexities associated with deformable object modeling and simulation. This is achieved through the integration of individual parameter identification into a cohesive and continuous process. The custom-built end-effector has enabled seamless and repeatable operations, demonstrating that deformable insulation can be manipulated during the pick-and-place subprocess to accurately achieve high precision positioning. The pressing step crucially facilitates the insertion of the insulations' edges first, minimizes uncertainties, which sets more favourable conditions for the final rolling step. The subsequent rolling ensures the insulation fits tightly within the frame cavity, leaving no noticeable deficiencies and gap.

A notable advantage of the H-GLPPR process is its adaptability to various common insulation sizes and wood stud dimensions without necessitating modifications to the end-effector hardware. Furthermore, the ability to use only a single robot arm that can be directly integrated with other prefabrication robotic processes streamline operations within the existing wood-frame wall panel prefabrication production line. The dimensions extracted from the CAD model feed into the algorithms outlined in Subsection 3.1.6, allowing for automatic calculation of target points and robotic trajectories. Therefore, for prefabrication production lines already utilizing robot arms, by only changing the end-effector, our H-GLPPR method can be employed. This reduces investment cost and compatibility issues, enhancing the efficiency and versatility of prefabrication automation.

## **Chapter 4 : Conclusion and Future Work**

### **4.1 Conclusion**

Motivated by the growing demands for light-frame construction and the need to enhance efficiency and worker health and safety, the integration of building prefabrication with robot arms offers a promising solution. In wood-frame building prefabrication, processes such as cutting and assembling rigid components like wood studs, drywall, and sheathing have already been streamlined through robot arm solutions. Established robotic solutions also exist for spray foam and blow-in insulation. However, spray foam insulation is more expensive compared to other types of insulation, and blow-in insulation technique has cross-compatibility issues and high investment costs. However, batt insulation remains the most commonly used insulation material for wood-frame wall in Canada, but there is no automated solution for installing it. This represents a significant gap in the field of automated building prefabrication.

The contributions of this thesis included the successful development and demonstration of two robotic methods, V-GLITPP and H-GLPPR, using a single robot arm to install batt insulation into typical straight wall frames. The V-GLITPP method involved picking up the insulation in its vertical configuration and contained a sequence of six major steps: Grasp, Lift, Insert, Tilt, Push, and Press, with accompanied parameter identification and selection. The Tilt, Push and Press steps specifically addressed the challenges of manipulating deformable objects. The designed end-effector utilized a two-finger parallel gripper equipped with custom-built textured gripping fingers to enhance gripping friction, ensuring reliable handling of batt insulation. Conversely, the H-GLPPR method picked up the insulation in its horizontal configuration and was structured around two subprocess: pick-and-place and insertion, with accompanied parameter identification and selection. The pick-and-place subprocess included the steps of grasping, lifting and placing each piece of insulation, ensuring reliable transfer. The insertion subprocess involved pressing and rolling steps where the Press step helped to properly constrain and position the insulation within the cavity, and the Roll step inserted and smoothed out the insulation into the frame, ensuring the uniformity of the installed insulation. The dedicated multi-purposed end-effector consists of two robotic tools, a dual parallel gripper set used during the pick-and-place subprocess, and a roller set for the insertion subprocess. Offline programming, in the digital twin environment, was used to develop an automatic algorithm to

calculate a series of target points for the entire process, which were critical for the generation of the robotic toolpath. This fully automated the robotic installation process by just inputting the frame dimensions and obtained process parameters values.

The V-GLITPP method achieved a high success rate of 93.3% in installing both fiberglass and mineral wool batt insulation into a scaled wall frame, thus, demonstrating the effectiveness and viability of robotic installation of batt insulation. The H-GLPPR was proven robust, capable of installing both types of insulation across four common full-scale wood frame sizes with 100% success rate. For different batt insulation manufacturers, sizes, and potentially material, the parameter selection in this thesis may serve as a baseline for parameter tuning specific to builders' circumstances.

Given V-GLITPP's advantage in handling smaller pieces of insulation and H-GLPPR's capacity for full-size installation, the two methods could be combined to facilitate robotic insulation installation for more complex wall configurations. For instance, such as employing the V-GLITPP method for insulation installation around doors, windows, and other intricate features of the wall that generally present smaller cavities, while employing the H-GLPPR method for larger cavities generally between full studs.

This thesis also contributes to the field of robotics in construction by providing practical solutions to streamline the building prefabrication automation process, enhancing efficiency, reducing labor intensity, and minimizing health risks associated with manual insulation installation methods. Additionally, it demonstrates that manipulating deformable objects with a robot arm, without sensor feedback, and without the need for extensive modeling and simulating of their actual deformation is viable.

## **4.2 Future Work**

Given the outcomes of this research, several promising directions for future work to facilitate smoother adoption within the industrial have been identified. They are:

1. As can be seen in the Chapter 3, it has difficulty to securely grasp the 23 by 3.5 inches (584 by 89 mm) fiberglass insulation. Therefore, it would be beneficial to increase the friction of the gripper fingers to ensure that all types of insulations are reliably held. This adjustment aims

to reduce slippage and improve handling precision, without compromising installation speed or needing additional setups for grasp locations.

2. In Chapter 3, automating the movement of the grippers on the T-slot frame and the gripper fingers on the gripping rails would eliminate the need for manual adjustments, thereby accommodating various insulation sizes more efficiently while facilitating more autonomous operations.

3. Incorporating computer vision could supervise the installation process by providing real-time feedback on the installation and condition of the insulation, rejecting damaged insulation prior to installation, and replacing the need for manual checks.

4. Including a robotic quick-change device into the end-effector to streamline integration into prefabrication production line and facilitate fast repurposing of the robot arm to where efforts are needed.

These enhancements would not only refine the existing capabilities but also extend the system's functionality, paving the way for broader industrial applications and innovations in robotic prefabrication construction.

## Bibliography

- [1] T. Gunawardena, P. Mendis, Prefabricated Building Systems—Design and Construction, *Encyclopedia 2* (2022) 70–95. <https://doi.org/10.3390/encyclopedia2010006>.
- [2] C.P. Chea, Y. Bai, X. Pan, M. Arashpour, Y. Xie, An integrated review of automation and robotic technologies for structural prefabrication and construction, *Transp. Saf. Environ.* 2 (2020) 81–96. <https://doi.org/10.1093/tse/tdaa007>.
- [3] L. Jaillon, C.S. Poon, Sustainable construction aspects of using prefabrication in dense urban environment: a Hong Kong case study, *Constr. Manag. Econ.* 26 (2008) 953–966. <https://doi.org/10.1080/01446190802259043>.
- [4] L. Jaillon, C.S. Poon, Y.H. Chiang, Quantifying the waste reduction potential of using prefabrication in building construction in Hong Kong, *Waste Manag.* 29 (2009) 309–320. <https://doi.org/10.1016/j.wasman.2008.02.015>.
- [5] J. Zhou, Y. Li, D. Ren, Quantitative study on external benefits of prefabricated buildings: From perspectives of economy, environment, and society, *Sustain. Cities Soc.* 86 (2022) 104132. <https://doi.org/10.1016/j.scs.2022.104132>.
- [6] K. Orłowski, Automated manufacturing for timber-based panelised wall systems, *Autom. Constr.* 109 (2020) 102988. <https://doi.org/10.1016/j.autcon.2019.102988>.
- [7] E. Lachance, N. Lehoux, P. Blanchet, Automated and robotized processes in the timber-frame prefabrication construction industry: A state of the art, in: *2022 IEEE 6th Int. Conf. Logist. Oper. Manag. GOL, IEEE, Strasbourg, France, 2022: pp. 1–10*. <https://doi.org/10.1109/GOL53975.2022.9820541>.
- [8] Light-frame timber construction - Comparison of four national design documents, *ISO/TR 12910:2010(E)*, (2010). [https://ewb.ihs.com/tmp\\_stamp/00011404795/JEXLQCAAAAAAAAAAAAA.pdf?sess=00011404795&prod=SPECS4](https://ewb.ihs.com/tmp_stamp/00011404795/JEXLQCAAAAAAAAAAAAA.pdf?sess=00011404795&prod=SPECS4) (accessed June 27, 2024).
- [9] S.C. Government of Canada, More workers are building housing in Canada, but labour shortages remain, (2024). <https://www.statcan.gc.ca/o1/en/plus/5661-more-workers-are-building-housing-canada-labour-shortages-remain> (accessed July 21, 2024).

- [10] P. Adekunle, C. Aigbavboa, O.K. Otasowie, S. Adekunle, Benefits of Robotic Utilization in the Prefabricated Construction Industry, in: Lille, France, 2023: pp. 746–754. <https://doi.org/10.24928/2023/0134>.
- [11] Y. Kim, H. Kim, R. Murphy, S. Lee, C.R. Ahn, Delegation or Collaboration: Understanding Different Construction Stakeholders' Perceptions of Robotization, *J. Manag. Eng.* 38 (2022) 04021084. [https://doi.org/10.1061/\(ASCE\)ME.1943-5479.0000994](https://doi.org/10.1061/(ASCE)ME.1943-5479.0000994).
- [12] H. Chai, H.J. Wagner, Z. Guo, Y. Qi, A. Menges, P.F. Yuan, Computational design and on-site mobile robotic construction of an adaptive reinforcement beam network for cross-laminated timber slab panels, *Autom. Constr.* 142 (2022) 104536. <https://doi.org/10.1016/j.autcon.2022.104536>.
- [13] J. Koerner-Al-Rawi, K.E. Park, T.K. Phillips, M. Pickoff, N. Tortorici, Robotic timber assembly, *Constr. Robot.* 4 (2020) 175–185. <https://doi.org/10.1007/s41693-020-00045-6>.
- [14] A. Menges, T. Schwinn, Manufacturing Reciprocities, *Archit. Des.* 82 (2012) 118–125. <https://doi.org/10.1002/ad.1388>.
- [15] G. Stricot-Tarboton, Robotic Arm Prefab Panels: A Proof of Concept, (2019). <http://researcharchive.vuw.ac.nz/handle/10063/8414> (accessed January 11, 2023).
- [16] Built Offsite, Robots poised to deliver innovation to prefabrication and construction industry, (2021). <https://builtoffsite.com.au/news/construction-industry-robots/> (accessed April 18, 2024).
- [17] House of Design, Automated Panel Framing, (n.d.). <https://thehouseofdesign.com/automation-products/panel-framing/> (accessed April 18, 2024).
- [18] Randek, ZeroLabor Robotic System, (n.d.). <https://www.randek.com/en/wall-floor-and-roof-production-lines/zerolabor> (accessed April 18, 2024).
- [19] U.S. Department of Energy, Types of Insulation, (n.d.). <https://www.energy.gov/energysaver/types-insulation> (accessed May 14, 2024).
- [20] Building Science.com Corporation, Info-501: Installation of Cavity Insulation, (n.d.). <https://buildingscience.com/documents/information-sheets/installation-of-cavity-insulation> (accessed July 19, 2024).
- [21] N.O. BREUM, T. SCHNEIDER, O. JØRGENSEN, T. VALDBJØRN RASMUSSEN, S. SKIBSTRUP ERIKSEN, Cellulosic Building Insulation versus Mineral Wool, Fiberglass or

- Perlite: Installer's Exposure by Inhalation of Fibers, Dust, Endotoxin and Fire-retardant Additives, *Ann. Occup. Hyg.* 47 (2003) 653–669. <https://doi.org/10.1093/annhyg/meg090>.
- [22] M. Kupczewska-Dobecka, K. Konieczko, S. Czerczak, Occupational risk resulting from exposure to mineral wool when installing insulation in buildings, *Int. J. Occup. Med. Environ. Health* 33 (2020) 757–769. <https://doi.org/10.13075/ijomeh.1896.01637>.
- [23] X. Li, S. Han, M. Gül, M. Al-Hussein, Automated post-3D visualization ergonomic analysis system for rapid workplace design in modular construction, *Autom. Constr.* 98 (2019) 160–174. <https://doi.org/10.1016/j.autcon.2018.11.012>.
- [24] K. Orłowski, Assessment of Manufacturing Processes for Automated Timber-Based Panelised Prefabrication, *Buildings* 9 (2019) 125. <https://doi.org/10.3390/buildings9050125>.
- [25] N. Mehrotra, M. Syal, M. Hastak, Manufactured Housing Production Layout Design: Journal of Architectural Engineering, *J. Archit. Eng.* 11 (2005) 25–34. [https://doi.org/10.1061/\(ASCE\)1076-0431\(2005\)11:1\(25\)](https://doi.org/10.1061/(ASCE)1076-0431(2005)11:1(25)).
- [26] Modular Building Automation, X-Combi - Complete Assembly Machine for Timber Frame Construction, (n.d.). <https://www.modularbuildingautomation.eu/x-combi> (accessed April 18, 2024).
- [27] M.S. Altaf, A. Bouferguene, H. Liu, M. Al-Hussein, H. Yu, Integrated production planning and control system for a panelized home prefabrication facility using simulation and RFID, *Autom. Constr.* 85 (2018) 369–383. <https://doi.org/10.1016/j.autcon.2017.09.009>.
- [28] O. Neumann, D. Schmidt, Innovative CNC Timber Framing — Technology and Cultural Expression, *Int. J. Archit. Comput.* 5 (2007) 469–486. <https://doi.org/10.1260/147807707782581774>.
- [29] B. M. Tehrani, S. BuHamdan, A. Alwisy, Robotics in assembly-based industrialized construction: a narrative review and a look forward, *Int. J. Intell. Robot. Appl.* 7 (2023) 556–574. <https://doi.org/10.1007/s41315-022-00257-9>.
- [30] H.J. Wagner, M. Alvarez, O. Kyjanek, Z. Bhiri, M. Buck, A. Menges, Flexible and transportable robotic timber construction platform – TIM, *Autom. Constr.* 120 (2020) 103400. <https://doi.org/10.1016/j.autcon.2020.103400>.

- [31] J. Willmann, M. Knauss, T. Bonwetsch, A.A. Apolinarska, F. Gramazio, M. Kohler, Robotic timber construction — Expanding additive fabrication to new dimensions, *Autom. Constr.* 61 (2016) 16–23. <https://doi.org/10.1016/j.autcon.2015.09.011>.
- [32] A. Thoma, A. Adel, M. Helmreich, T. Wehrle, F. Gramazio, M. Kohler, Robotic Fabrication of Bespoke Timber Frame Modules, in: J. Willmann, P. Block, M. Hutter, K. Byrne, T. Schork (Eds.), *Robot. Fabr. Archit. Art Des.* 2018, Springer International Publishing, Cham, 2019: pp. 447–458. [https://doi.org/10.1007/978-3-319-92294-2\\_34](https://doi.org/10.1007/978-3-319-92294-2_34).
- [33] T. Bock, T. Linner, *Robotic Industrialization: Automation and Robotic Technologies for Customized Component, Module, and Building Prefabrication*, 1st ed., Cambridge University Press, 2015. <https://doi.org/10.1017/CBO9781139924153>.
- [34] M. Holloway, M. Julia, P. Childs, A robot for spray applied insulation in underfloor voids, in: *Proc. ISR 2016 47st Int. Symp. Robot.*, 2016: pp. 1–7. <https://ieeexplore.ieee.org/document/7559133/?arnumber=7559133> (accessed July 30, 2024).
- [35] Spray-R, 4-in1 insulation installed with a touch of a button, (n.d.). <https://www.spray-r.com> (accessed July 25, 2023).
- [36] SprayWorks, Spraybot - Automated Spray Foam Machines, (n.d.). <https://sprayworksequipment.com/products/spray-robots/spraybot/> (accessed July 26, 2023).
- [37] Randek, House Production Technologies - Robotic blow-in insulation cell, (n.d.). <https://www.randek.com/en/news/robotic-blow-in-insulation-cell#> (accessed April 18, 2024).
- [38] HOMAG, Multifunction Bridge WALLTEQ M-300/M-500 insuFill, (n.d.). <https://www.homag.com/en/product-detail/machines/house-construction/weinmann-multifunction-bridge/multifunction-bridge-wallteq-m-300m-500-insufill> (accessed April 18, 2024).
- [39] J. Su, R. Li, H. Qiao, J. Xu, Q. Ai, J. Zhu, Study on dual peg-in-hole insertion using of constraints formed in the environment, *Ind. Robot Int. J.* 44 (2017) 730–740. <https://doi.org/10.1108/IR-07-2016-0186>.

- [40] C.H. Kim, J. Seo, Shallow-Depth Insertion: Peg in Shallow Hole Through Robotic In-Hand Manipulation, *IEEE Robot. Autom. Lett.* 4 (2019) 383–390. <https://doi.org/10.1109/LRA.2018.2890449>.
- [41] J. Xu, Z. Hou, Z. Liu, H. Qiao, Compare Contact Model-based Control and Contact Model-free Learning: A Survey of Robotic Peg-in-hole Assembly Strategies, (2019). <http://arxiv.org/abs/1904.05240> (accessed March 11, 2024).
- [42] Y.C. Hou, K.S.M. Sahari, D.N.T. How, A review on modeling of flexible deformable object for dexterous robotic manipulation, *Int. J. Adv. Robot. Syst.* 16 (2019) 1729881419848894. <https://doi.org/10.1177/1729881419848894>.
- [43] H. Lipson, Challenges and Opportunities for Design, Simulation, and Fabrication of Soft Robots, *Soft Robot.* 1 (2014) 21–27. <https://doi.org/10.1089/soro.2013.0007>.
- [44] P. Jiménez, Survey on model-based manipulation planning of deformable objects, *Robot. Comput.-Integr. Manuf.* 28 (2012) 154–163. <https://doi.org/10.1016/j.rcim.2011.08.002>.
- [45] J. Sanchez, J.A. Corrales Ramon, B.C. BOUZGARROU, Y. Mezouar, Robotic Manipulation and Sensing of Deformable Objects in Domestic and Industrial Applications: A Survey, *Int. J. Robot. Res.* 37 (2018) 688–716. <https://doi.org/10.1177/0278364918779698>.
- [46] F. F., P. Payeur, Dexterous Robotic Manipulation of Deformable Objects with Multi-Sensory Feedback - a Review, in: A. Jimenez, B.M. Al Hadithi (Eds.), *Robot Manip. Trends Dev., InTech*, 2010. <https://doi.org/10.5772/9183>.
- [47] P. Boonvisut, M.C. Çavuşoğlu, Identification and active exploration of deformable object boundary constraints through robotic manipulation, *Int. J. Robot. Res.* 33 (2014) 1446–1461. <https://doi.org/10.1177/0278364914536939>.
- [48] V.E. Arriola-Rios, P. Guler, F. Ficuciello, D. Kragic, B. Siciliano, J.L. Wyatt, Modeling of Deformable Objects for Robotic Manipulation: A Tutorial and Review, *Front. Robot. AI* 7 (2020) 82. <https://doi.org/10.3389/frobt.2020.00082>.
- [49] S. Makris, F. Dietrich, K. Kellens, S.J. Hu, Automated assembly of non-rigid objects, *CIRP Ann.* 72 (2023) 513–539. <https://doi.org/10.1016/j.cirp.2023.05.003>.
- [50] V.E. Arriola-Rios, J.L. Wyatt, A Multimodal Model of Object Deformation Under Robotic Pushing, *IEEE Trans. Cogn. Dev. Syst.* 9 (2017) 153–169. <https://doi.org/10.1109/TCDS.2017.2664058>.

- [51] I.G. Ramirez-Alpizar, K. Harada, E. Yoshida, A simple assembly planner for the insertion of ring-shaped deformable objects, *Assem. Autom.* 38 (2018) 182–194. <https://doi.org/10.1108/AA-12-2016-181>.
- [52] W. Wang, D. Berenson, D. Balkcom, An online method for tight-tolerance insertion tasks for string and rope, in: 2015 IEEE Int. Conf. Robot. Autom. ICRA, IEEE, Seattle, WA, USA, 2015: pp. 2488–2495. <https://doi.org/10.1109/ICRA.2015.7139532>.
- [53] X. Li, J. Liu, X. Fan, J. Qin, R. Zhang, R. Cao, P. Wang, X. Huo, Simulating Study on Mechanical Properties of Rock Wool Board for Thermal Insulation on External Walls, *Adv. Mater. Sci. Eng.* 2020 (2020) e4028941. <https://doi.org/10.1155/2020/4028941>.
- [54] L. Chapelle, P. Brondsted, Y. Kusano, M.R. Foldschack, D. Lybye, M. Levesque, Characterization and modelling of the mechanical properties of mineral wool, (2016). <https://core.ac.uk/download/pdf/84000246.pdf> (accessed June 11, 2023)
- [55] A. Buska, R. Mačiulaitis, The compressive strength properties of mineral wool slabs: Influence of structure anisotropy and methodical factors, *J. Civ. Eng. Manag.* 13 (2007) 97–106. <https://doi.org/10.3846/13923730.2007.9636425>.
- [56] L.Y. Chen, B. Shi, D. Seita, R. Cheng, T. Kollar, D. Held, K. Goldberg, AutoBag: Learning to Open Plastic Bags and Insert Objects, in: 2023 IEEE Int. Conf. Robot. Autom. ICRA, IEEE, London, United Kingdom, 2023: pp. 3918–3925. <https://doi.org/10.1109/ICRA48891.2023.10161402>.
- [57] S. Caro, C. Chevallereau, A. Remus, Manipulating Deformable Objects with a Dual-arm Robot, in: Proc. 2nd Int. Conf. Robot. Comput. Vis. Intell. Syst., SCITEPRESS - Science and Technology Publications, Online Streaming, --- Select a Country ---, 2021: pp. 48–56. <https://doi.org/10.5220/0010707600003061>.
- [58] G. Papadopoulos, D. Andronas, E. Kampourakis, N. Theodoropoulos, P.S. Kotsaris, S. Makris, On deformable object handling: multi-tool end-effector for robotized manipulation and layup of fabrics and composites, *Int. J. Adv. Manuf. Technol.* 128 (2023) 1675–1687. <https://doi.org/10.1007/s00170-023-11914-z>.
- [59] Z. Zoller, P. Zentay, Á. Meggyes, G. Arz, Robotical Handling of Polyurethane Foams with Needle Grippers, *Period. Polytech. Mech. Eng.* 43 (1999) 229–238.

- [60] E. Glorieux, P. Franciosa, D. Ceglarek, End-effector design optimisation and multi-robot motion planning for handling compliant parts, *Struct. Multidiscip. Optim.* 57 (2018) 1377–1390. <https://doi.org/10.1007/s00158-017-1798-x>.
- [61] Z. Wang, Y. Makiyama, S. Hirai, Ritsumeikan University 1-1-1 Noji-higashi, Kusatsu, Shiga 525-8577, Japan, A Soft Needle Gripper Capable of Grasping and Piercing for Handling Food Materials, *J. Robot. Mechatron.* 33 (2021) 935–943. <https://doi.org/10.20965/jrm.2021.p0935>.
- [62] J. Gafford, Y. Ding, A. Harris, T. McKenna, P. Polygerinos, D. Holland, C. Walsh, A. Moser, Shape Deposition Manufacturing of a Soft, Atraumatic, and Deployable Surgical Grasper, *J. Mech. Robot.* 7 (2015) 021006. <https://doi.org/10.1115/1.4029493>.
- [63] D. Mira, A. Delgado, C.M. Mateo, S.T. Puente, F.A. Candelas, F. Torres, Study of dexterous robotic grasping for deformable objects manipulation, in: 2015 23rd Mediterr. Conf. Control Autom. MED, IEEE, Torremolinos, Malaga, Spain, 2015: pp. 262–266. <https://doi.org/10.1109/MED.2015.7158760>.
- [64] D. Andronas, Z. Arkouli, N. Zacharaki, G. Michalos, A. Sardelis, G. Papanikolopoulos, S. Makris, On the perception and handling of deformable objects – A robotic cell for white goods industry, *Robot. Comput.-Integr. Manuf.* 77 (2022) 102358. <https://doi.org/10.1016/j.rcim.2022.102358>.
- [65] PINK Next Gen Fiberglas Insulation Installation Instructions & Guidelines, Owens Corning (2023). <https://dcpd6wotaa0mb.cloudfront.net/mdms/dms/Residential%20Insulation/10024604/10024604-PINK-Next-Gen-Fiberglas-Insulation-Installation-Instructions-and-Guidelines.pdf?v=1712161356000> (accessed May 21, 2024).
- [66] ROCKWOOL Comfortbatt - Residential Installation Guide, ROCKWOOL (2023). <https://www.rockwool.com/syssiteassets/o2-rockwool/documentation/technical-guides/residential/comfortbatt-residential-installation-guide.pdf?f=20230815123042> (accessed May 21, 2024).
- [67] National Building Code of Canada 2020, NBC2020, National Research Council Canada, 2020.
- [68] CanmetENERGY, Prefabricated Exterior Energy Retrofit (PEER) Project Guide, Natural Resources Canada (2023). <https://natural->

[resources.canada.ca/sites/nrcan/files/pdf/PEER%20Guide\\_EN\\_FINAL.pdf](https://resources.canada.ca/sites/nrcan/files/pdf/PEER%20Guide_EN_FINAL.pdf) (accessed July 19, 2024).

[69] National Energy Code of Canada for Buildings 2020, NECB2020, National Research Council Canada, 2020.

## Appendix A

In this appendix, it provides the fire requirement for exterior wall panel with wood components for combustible and non-combustible constructions in National Building Code (NBC) 2020 [67].

For combustible construction, not less than 90% of the exterior cladding on each building's exterior wall shall consist of non-combustible material. Otherwise, the wall assembly must satisfy the CAN/ULC-S134 standard, which specifies that flaming on or in the wall assembly does not spread more than 5 m above the opening and that the heat flux during the flame exposure on the wall assembly is no more than 35 kW/m<sup>2</sup> measured at 3.5 m from the opening. Where a building is considered to be facing a street, it has the same requirement as above. Alternatively, a wall assembly including combustible cladding made of fire-retardant-treated wood shall be tested for fire exposure after the cladding has been subjected to the accelerated weathering test. If the building is not required to have a fire-resistance rating of more than 45 minutes, heavy timber construction is permitted. More specifics on the standard can be found in NBC 2020 Section 3.1.4.

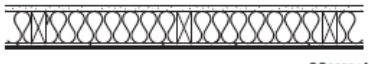
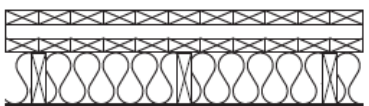
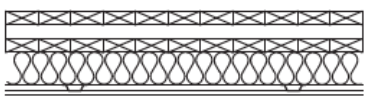
For non-combustible construction, some of the combustible components are permitted. For example, combustible cladding on exterior walls is permitted if the building is not more than three storeys high or is sprinklered throughout and the wall assembly satisfies the CAN/ULC-S134 standard and the details mentioned above. For factory-assembled panels containing foamed plastic insulation with a flame-spread rating not more than 500 is permitted to be used. If the building is sprinklered and not more than 18 m high, measured from grade to the underside of the roof, and does not contain Groups A, B, or C as major occupancy. More specifics on the standard can be found in NBC 2020 Section 3.1.5.

For encapsulated mass timber construction, the minimum thickness of exterior walls in encapsulated mass timber construction is 96 mm. Non-loadbearing wood elements permitted in non-combustible construction exterior walls do not need to conform to this. In general, not more than 10% of the combustible cladding is allowed on each exterior wall of each storey; up to 100% of the combustible cladding on exterior walls of the first storey; not exceed 5% of the combustible cladding on each exterior wall of each storey where the fire department arrival time

exceeds 10 mins. A wall assembly that includes fire-retardant-treated wood shall be tested for fire exposure (ASTM D2898). More specifics on the standard can be found in NBC 2020, Section 3.1.6.

The exterior wall assemblies illustrated below as Table D-6.1.1 and Notes to the Table D-6.1.1 of NBC 2020 are deemed to satisfy the criteria for the CAN/ULC-S134 standard. In the assembly, wood studs are filled with non-combustible insulation rock or slag fiber with gypsum sheathing and non-combustible exterior cladding or fire-retardant treated wood siding. The Wall number EXTW-1 shown below uses a 2x4 timber frame as a structural member and fits our project structural design concept. EXTW-1 is built with 2x4 wood studs 16 inches apart, rockwool insulation in the stud cavities, and 12-inch fire-retardant-treated plywood siding.

**Table D-6.1.1.**  
**Construction Specifications for Exterior Wall Assemblies that Are Deemed to Satisfy the Criteria of Clause 3.1.5.5.(1)(b) when Tested in Accordance with CAN/ULC-S134**

Wall Number	Structural Members	Absorptive Material	Sheathing	Cladding	Design
EXTW-1	38 mm x 89 mm wood studs spaced at 400 mm o.c. <sup>(1)(2)</sup>	89 mm thick rock or slag fibre in cavities formed by studs <sup>(3)(4)</sup>	—	12.7 mm thick fire-retardant-treated plywood siding <sup>(5)</sup>	 GG00531A
EXTW-2	38 mm x 140 mm wood studs spaced at 400 mm o.c. <sup>(1)(2)</sup>	140 mm thick rock or slag fibre in cavities formed by studs <sup>(3)(4)</sup>	Gypsum sheathing ≥ 12.7 mm thick	Noncombustible exterior cladding	 GG00530A
EXTW-3	38 mm x 140 mm wood studs spaced at 400 mm o.c. <sup>(1)(2)</sup>	140 mm thick rock or slag fibre in cavities formed by studs <sup>(3)(4)</sup>	15.9 mm thick fire-retardant-treated plywood <sup>(6)</sup>	Noncombustible exterior cladding	 GG00532A
EXTW-4	38 mm x 140 mm wood studs spaced at 600 mm o.c. <sup>(1)(7)</sup> attached to cross-laminated timber (CLT) wall panels ≥ 38 mm thick <sup>(8)</sup>	140 mm thick glass, rock or slag fibre in cavities formed by studs <sup>(3)</sup>	Gypsum sheathing ≥ 12.7 mm thick	Noncombustible exterior cladding	 GG00533A
EXTW-5	89 mm horizontal Z-bars spaced at 600 mm o.c. attached to CLT wall panels ≥ 105 mm thick <sup>(8)</sup>	89 mm thick rock or slag fibre in cavities formed by Z-bars <sup>(3)(4)</sup>	—	Noncombustible exterior cladding attached to 19 mm vertical hat channels spaced at 600 mm o.c.	 GG00534A

**Notes to Table D-6.1.1.:**

(1) The stated stud dimensions are maximum values. Where wood studs with a smaller depth are used, the thickness of the absorptive material in the cavities formed by the studs must be reduced accordingly.

**Table D-6.1.1. (Continued)**

- (2) Horizontal blocking between the vertical studs or horizontal stud plates must be installed at vertical intervals of not more than 2 324 mm, such that the maximum clear length between the horizontal blocking or stud plates is 2 286 mm.
- (3) The absorptive material must conform to CAN/ULC-S702.1, "Standard for Mineral Fibre Thermal Insulation for Buildings, Part 1: Material Specification."
- (4) The absorptive material must have a density not less than 32 kg/m<sup>3</sup>.
- (5) The fire-retardant-treated plywood siding must conform to the requirements of Article 3.1.4.5. and must have been conditioned in conformance with ASTM D2898, "Standard Practice for Accelerated Weathering of Fire-Retardant-Treated Wood for Fire Testing," before being tested in accordance with CAN/ULC-S102, "Standard Method of Test for Surface Burning Characteristics of Building Materials and Assemblies."
- (6) The fire-retardant-treated plywood must conform to the requirements of Article 3.1.4.5.
- (7) Horizontal blocking between the vertical studs or horizontal stud plates must be installed at vertical intervals of not more than 2 438 mm, such that the maximum clear length between the horizontal blocking or stud plates is 2 400 mm.
- (8) A water-resistant barrier is permitted to be attached to the face of the CLT wall panels.

Based on the code, using the timber framing panel for exterior retrofitting is viable, but it needs to be tested against the CAN/ULC-S134 standard if the design is outside the assemblies listed in Table D-6.1.1.

## Appendix B

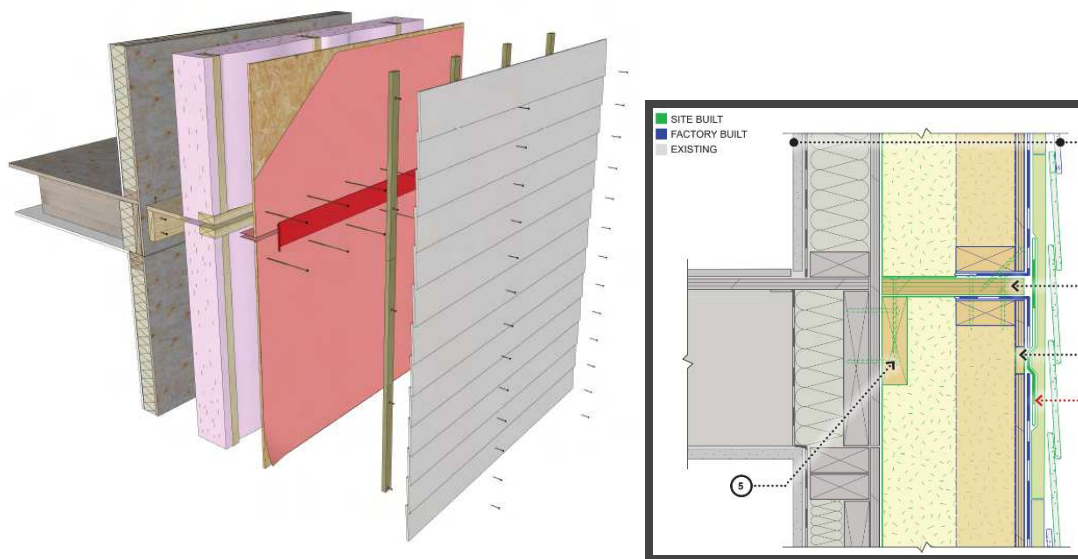
This appendix is dedicated to the design and verification of the insulation required for the wood-frame wall panel and connection proposed by RoBIM Technology for building energy retrofit proposes. It includes a case study of NRCan PEER Project, an overview of building code requirements, and detailed thermal and hygrothermal analysis. These analyses are conducted without considering cladding to focus purely on the performance of the insulation materials within the specified wall panel configurations.

### B.1 Case Study - NRCan PEER Project

We studied NRCan Prefabricated Xxterior Energy Retrofit (PEER) Project Guide [68]. As well as we performed hand calculations for the NRCan 2x4 framed panel, 2x6 framed panel, 2x8 framed panel and I-joist-framed panel wall systems.

#### B.1.1 PEER Wall – 2x4 Framed Panel Wall System

In the 2x4 Framed Panel Wall System, it contains 6 layers. They are 4 ½ inches backing with blown-in cellulose insulation installed on-site, 2x4 lumber (with 24” framing spacing) with blown-in cellulose insulation installed on-site, ½ inches OSB wall sheathing, self-adhered vapour permeable membrane, borate-treated strapping with air cavity, and cladding. The illustration is shown in Figure B.1.



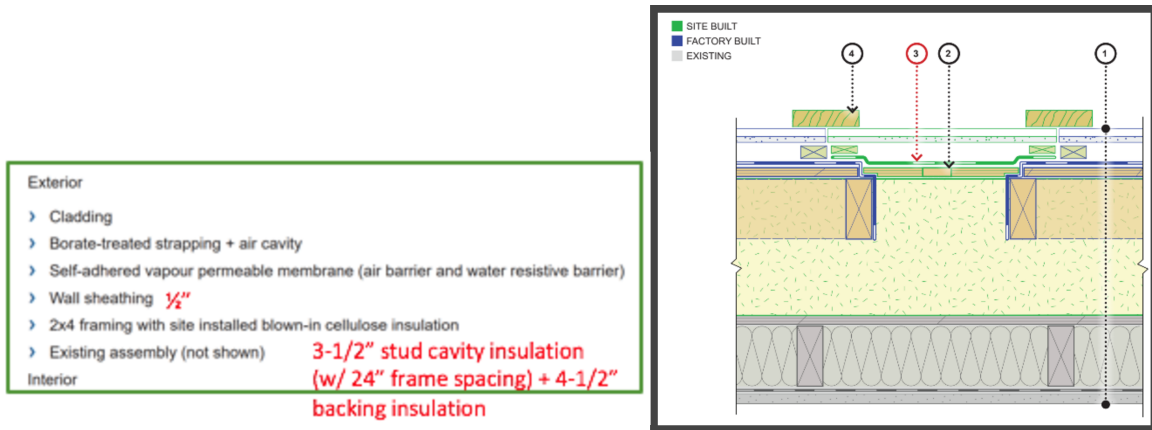


Figure B.1: Exploded view of partial retrofit light-framed panel components at floor line transition

We used isothermal and parallel path methods to calculate the effective R values of 2x4, 2x6 and 2x8 framed panels based on the approximate dimensions from the above illustration. The following tables show the results. As can be seen, with 5% deduction, a 2x4 framed panel is R-28.5, a 2x6 framed wall is R-33, and a 2x8 framed panel is R-38.

Assembly Effective RSI (m <sup>2</sup> K/W)			
Material	Thickness (mm)	RSI/mm	RSI
Exterior air film			0.03
Cladding on wood strapping			0
AB/WRB			0
OSB Sheathing	12.7	0.0098	0.12
Effective 2x4 Wood stud & Insulation			1.74
Insulation	114	0.029	3.306
		<b>Effective RSI</b>	<b>5.20</b>
		<b>Effective R</b>	<b>30</b>

$$2x4 \text{ Framed Panel Effective R} = 30 * (1 - 5\%) = 28.5$$

Assembly Effective RSI (m <sup>2</sup> K/W)			
Material	Thickness (mm)	RSI/mm	RSI
Exterior air film			0.03
Cladding on wood strapping			0
AB/WRB			0
OSB Sheathing	12.7	0.0098	0.12
Effective 2x6 Wood stud & Insulation			2.74
Insulation	114	0.029	3.306
		<b>Effective RSI</b>	<b>6.20</b>
		<b>Effective R</b>	<b>35</b>

$$2x6 \text{ Framed Panel Effective R} = 35 * (1 - 5\%) = 33.25$$

Assembly Effective RSI (m <sup>2</sup> K/W)			
Material	Thickness (mm)	RSI/mm	RSI
Exterior air film			0.03
Cladding on wood strapping			0
AB/WRB			0
OSB Sheathing	12.7	0.0098	0.12
Effective 2x8 Wood stud & Insulation			3.60
Insulation	114	0.029	3.306
		<b>Effective RSI</b>	<b>7.06</b>
		<b>Effective R</b>	<b>40</b>

$$2x8 \text{ Framed Panel Effective R} = 40 * (1 - 5\%) = 38$$

Shown below is a sample calculation for the 2x4 framed panel.

1.  $RSI_{\text{effective}} = RSI (\text{Exterior air film} + \text{cladding on wood stripping} + \text{AB/WRB} + \frac{1}{2}'' \text{ OSB sheathing} + \text{Effective 2x4 wood stud and insulation} + \text{Backing insulation})$

$$2. RSI_{\text{wood stud and insulation}} = RSI_{\text{parallel}} = \frac{100}{\frac{\% \text{ area of framing}}{RSI_f} + \frac{\% \text{ area of cavity}}{RSI_c}}$$

$$= \frac{100}{\frac{20}{0.76} + \frac{80}{2.58}} = 1.74$$

3.  $RSI = 0.03 + 0 + 0 + 0.12 + 1.74 + 3.31 = 5.20 \text{ m}^2\text{K/W}$

Table A-9.36.2.4.(1)-A  
Framing and Cavity Percentages for Typical Wood-frame Assemblies<sup>(1)</sup>

Wood-frame Assemblies	Frame Spacing, mm o.c.										
	304		406		488		610		1220		
	% Area Framing	% Area Cavity	% Area Framing	% Area Cavity	% Area Framing	% Area Cavity	% Area Framing	% Area Cavity	% Area Framing	% Area Cavity	
Floors	lumber joists	-	-	13	87	11.5	88.5	10	90	-	-
	I-joists and truss	-	-	9	91	7.5	92.5	6	94	-	-
Roofs/Ceilings	ceilings with typical trusses	-	-	14	86	12.5	87.5	11	89	-	-
	ceilings with raised heel trusses	-	-	10	90	8.5	91.5	7	93	-	-
	roofs with lumber rafters and ceilings with lumber joists	-	-	13	87	11.5	88.5	10	90	-	-
	roofs with I-joist rafters and ceilings with I-joists	-	-	9	91	7.5	92.5	6	94	-	-
roofs with structural insulated panels (SIPs)	-	-	-	-	-	-	-	-	9	91	
Walls	typical wood-frame	24.5	75.5	23	77	21.5	78.5	20	80	-	-
	advanced wood-frame with double top plate <sup>(2)</sup>	-	-	19	81	17.5	82.5	16	84	-	-
	SIPs	-	-	-	-	-	-	-	-	14	86
basement wood-frame inside concrete foundation wall	-	-	16	84	14.5	85.5	13	87	-	-	

NBC 2020

### B.1.2 PEER Wall – I-Joist Framed Panel Wall System

In the I-Joist Framed Panel Wall System, there are seven layers which are self-adhered air barrier, 1 ½ inches compressible mineral fiber gap fill insulation, I-joist framing (with 23 inches framing spacing) with 8 inches stud cavity batt insulation and retaining meshing, ½ inches OSB wall sheathing, self-adhered vapour permeable membrane, borate-treated strapping with air cavity, and cladding. The 1 ½ inches compressible insulation can accommodate the unevenness of the existing building’s exterior wall. The illustration is shown in Figure B.2.

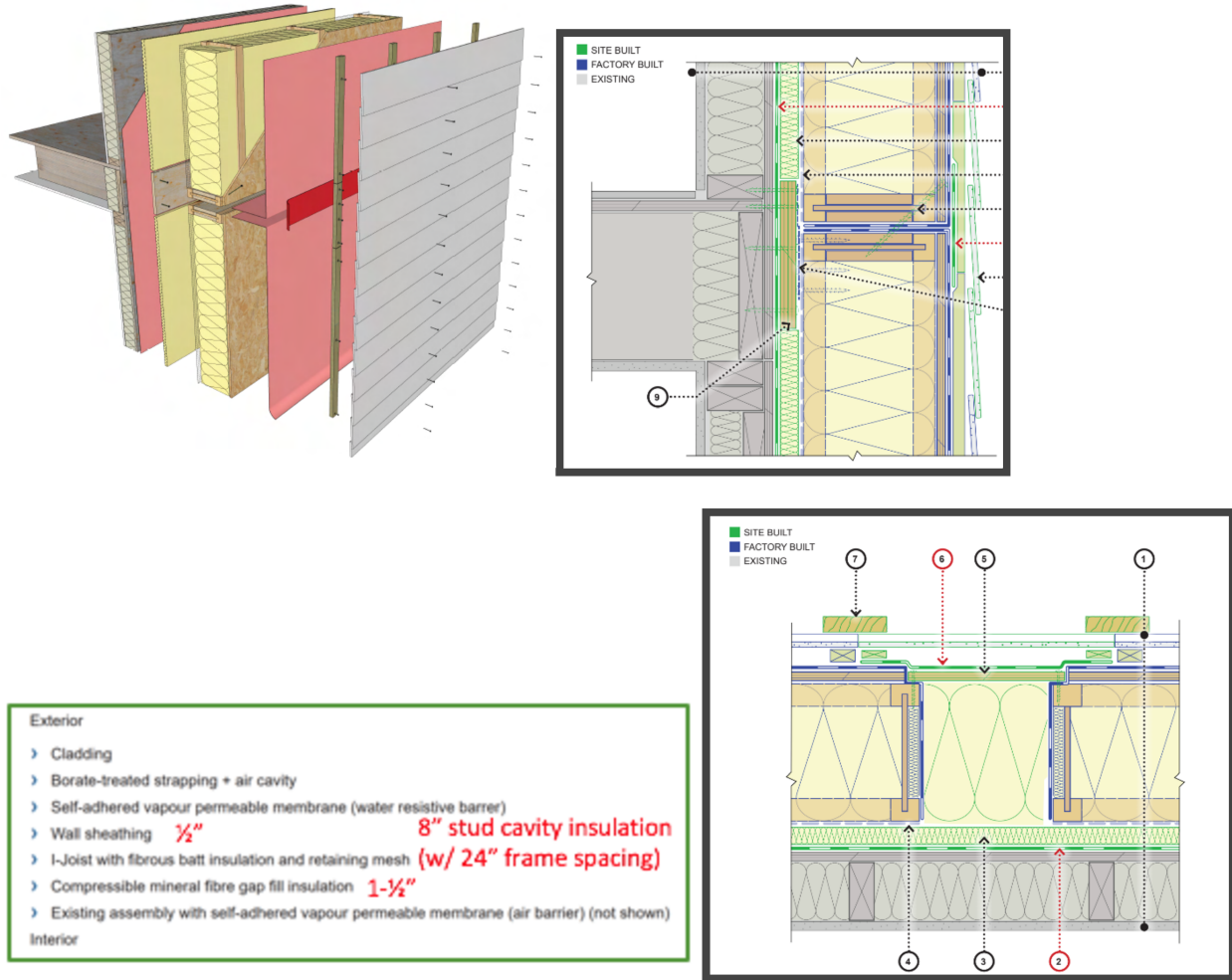


Figure B.2: Exploded view of partial retrofit I-joint framed panel components at floor line transition

We calculated the effective R value for the I-joint framed panel based on the approximate dimension from the above illustration by using the same method as the 2x4 framed panel. The calculations show that the panel has an effective R-35.

Assembly Effective RSI (m <sup>2</sup> K/W)			
Material	Thickness (mm)	RSI/mm	RSI
Exterior air film			0.03
Cladding on wood strapping			0
WRB			0
OSB Sheathing	12.7	0.0098	0.12
Effective I-Joist Wood stud & Insulation	203		5.20
Mineral Fibre Insulation	38	0.0294	1.12
		<b>Effective RSI</b>	<b>6.47</b>
		<b>Effective R</b>	<b>37</b>

$$1\text{-}3/4'' \times 8'' \text{ I-Joist Framed Panel Effective R} = 37 * (1 - 5\%) = 35$$

### B.1.3 Section Summary

Based on the RDH Building Science’s Thermal Modeling Report [7] for NRCAN PEER Project OCH PEER Panel, a comparison between the hand calculation and ANSYS 3D model’s calculations for a typical wood-framed wall panel was performed, and a 3% - 7% difference for R10 to R40 insulations was obtained. We found that, for simplified calculations, a 5% deduction in R value to account for thermal bridging is acceptable. Therefore, for 2x4 framed panel and I-joist-framed panel wall systems, we can apply a 5% deduction.

## B.2 Building Codes

The requirements for R value in NECB 2020 for Part 3 buildings (complex buildings) are shown in Table 3.2.2.2 [69]. For above-ground opaque building wall assembly in Edmonton, it requires R-26.4.

**Table 3.2.2.2.**  
Overall Thermal Transmittance of Above-ground Opaque Building Assemblies  
Forming Part of Sentences 3.2.2.2.(1) and (2)

Above-ground Opaque Building Assembly	Heating Degree-Days of Building Location, <sup>(1)</sup> in Celsius Degree-Days					
	Zone 4: <sup>(2)</sup> < 3000	Zone 5: <sup>(2)</sup> 3000 to 3999	Zone 6: <sup>(2)</sup> 4000 to 4999	Zone 7A: <sup>(2)</sup> 5000 to 5999	Zone 7B: <sup>(2)</sup> 6000 to 6999	Zone 8: <sup>(2)</sup> ≥ 7000
	Maximum Overall Thermal Transmittance, $W/m^2K$					
Walls	0.280	0.265	0.240	0.215	0.190	0.165
Roofs	0.164	0.156	0.138	0.121	0.117	0.110
Floors	0.193	0.175	0.156	0.138	0.121	0.117

R 26.4  
RSI 4.65

The requirements for R value in NBC 2020 for Part 9 buildings (simple buildings) are shown in Table 9.36.2.6.-A [67]. For above-ground opaque building wall assembly in Edmonton, it needs R-17.5 without HRV and R-17 with HRV.

**Table 9.36.2.6-A**  
**Effective Thermal Resistance of Above-ground Opaque Assemblies in Buildings without a Heat-Recovery Ventilator**  
 Forming Part of Sentence 9.36.2.6.(1)

Above-ground Opaque Building Assembly	Heating Degree-Days of Building Location, <sup>(1)</sup> in Celsius Degree-Days					
	Zone 4 < 3000	Zone 5 3000 to 3999	Zone 6 4000 to 4999	Zone 7A 5000 to 5999	Zone 7B 6000 to 6999	Zone 8 ≥ 7000
	Minimum Effective Thermal Resistance (RSI) (m <sup>2</sup> ·K)/W					
Ceilings below attics	6.91	8.67	8.67	10.43	10.43	10.43
Cathedral ceilings and flat roofs	4.67	4.67	4.67	5.02	5.02	5.02
Walls <sup>(2)</sup>	2.78	3.08	3.08	3.08	3.85	3.85
Floors over unheated spaces	4.67	4.67	4.67	5.02	5.02	5.02

R 17.5

**Table 9.36.2.6-B**  
**Effective Thermal Resistance of Above-ground Opaque Assemblies in Buildings with a Heat-Recovery Ventilator**  
 Forming Part of Sentence 9.36.2.6.(1)

Above-ground Opaque Building Assembly	Heating Degree-Days of Building Location, <sup>(1)</sup> in Celsius Degree-Days					
	Zone 4 < 3000	Zone 5 3000 to 3999	Zone 6 4000 to 4999	Zone 7A 5000 to 5999	Zone 7B 6000 to 6999	Zone 8 ≥ 7000
	Minimum Effective Thermal Resistance (RSI) (m <sup>2</sup> ·K)/W					
Ceilings below attics	6.91	6.91	8.67	8.67	10.43	10.43
Cathedral ceilings and flat roofs	4.67	4.67	4.67	5.02	5.02	5.02
Walls <sup>(2)</sup>	2.78	2.97	2.97	2.97	3.08	3.08
Floors over unheated spaces	4.67	4.67	4.67	5.02	5.02	5.02

R 17

Since the highest effective thermal resistance required by the building code is R-26.4 and the 2x4 framed panel from NRCan design has R-28.5, we decided to adopt the 2x4 framed panel concept. For Part 3 buildings in Edmonton, in order to meet the wall R value requirement, the minimum backing for continuous insulation needs to be 104 mm if other layers are not changed. This represents an extreme case, assuming a complete absence of insulation in the current structure. If there is already insulation present in the existing building, it is possible to decrease the thickness of the continuous insulation layer to meet the building code requirements.

Assembly Effective RSI (m <sup>2</sup> K/W)			
Material	Thickness (mm)	RSI/mm	RSI
Exterior air film			0.03
Cladding on wood strapping			0
AB/WRB			0
OSB Sheathing	12.7	0.0098	0.12
Effective 2x4 Wood stud & Insulation			1.74
Continuous Insulation	104	0.029	3.016
		<b>Effective RSI</b>	<b>4.91</b>
		<b>Effective R</b>	<b>27.9</b>

$$2x4 \text{ Framed Panel Effective R} = 27.9 \cdot (1 - 5\%) = 26.5$$

For Part 9 buildings in Edmonton, buildings without an HRV system require a slightly larger R value compared to buildings with an HRV system; therefore, we used the R value without an HRV system and got 47mm for the minimum backing of continuous insulation. Since Part 3 buildings have a higher R value requirement, we will use 104 mm continuous insulation (rigid mineral wool) for our preliminary design.

Assembly Effective RSI (m <sup>2</sup> K/W)			
Material	Thickness (mm)	RSI/mm	RSI
Exterior air film			0.03
Cladding on wood strapping			0
AB/WRB			0
OSB Sheathing	12.7	0.0098	0.12
Effective 2x4 Wood stud & Insulation			1.74
Continuous Insulation	47	0.029	1.363
Effective RSI			3.26
Effective R			18.5

$$2x4 \text{ Framed Panel Effective R} = 18.5 * (1 - 5\%) = 17.6$$

### B.3 Proposed Light-frame Panel Thermal Analysis

The overall effective thermal performance of the wall panel can be calculated using clear field thermal transmittance and thermal bridging, which can be seen from the following equation.

$$U_T = \frac{\Sigma(\Psi \cdot L) + \Sigma(\chi)}{A_{Total}} + U_o$$

Where:

- U<sub>T</sub> = total effective assembly thermal transmittance (Btu/hr-ft<sup>2</sup>-°F or W/m<sup>2</sup>K)
- U<sub>o</sub> = clear field thermal transmittance (Btu/hr-ft<sup>2</sup>-°F or W/m<sup>2</sup>K)
- A<sub>total</sub> = the total opaque wall area (ft<sup>2</sup> or m<sup>2</sup>)
- Ψ = heat flow from linear thermal bridge (Btu/hr-ft °F or W/mK)
- L = length of linear thermal bridge, i.e. slab width (ft or m)
- χ = heat flow from point thermal bridge (Btu/hr- °F or W/K)

#### B.3.1 Clear Field Thermal Performance

Based on the information provided in RoBIM proposed wood-frame wall panel, the clear field thermal performance of the primary design of the panel was estimated to be approximately RSI-4.91 (R-27.9). However, this panel does not include gypsum board, interior air film and

expanding foam tape between the panel joints. By incorporating these components, the resulting effective R value will be increased to RSI-5.11 (R-29).

Panel Effective RSI (m <sup>2</sup> K/W)			
Material	Thickness (mm)	RSI/mm	RSI
Exterior air film			0.03
Cladding on wood strapping			0.00
AB/WRB			0.00
OSB Sheathing	12.7	0.0098	0.12
Effective 2x4 Wood stud & Insulation			1.74
Gypsum board	12.7	0.00625	0.08
Continuous Insulation	104	0.029	3.02
Interior air film			0.12
		<b>Effective RSI</b>	<b>5.11</b>
		<b>Effective R</b>	<b>29.0</b>

In this section, a comprehensive 3D ANSYS model of the wall panel, excluding cladding, has been analyzed. The clear field R-value of the panel assembly is determined to be RSI-5.66 (R-32.1). The heat flux and temperature distribution are represented in Figure B.3.

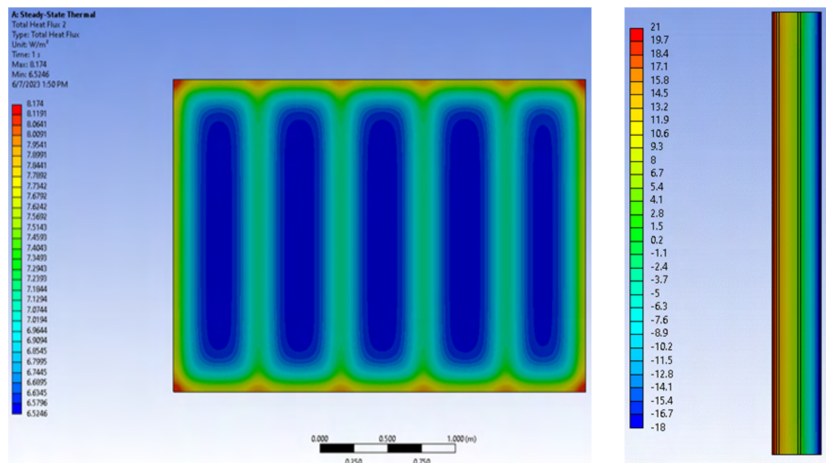


Figure B.3: Left: 3D modeling - Heat flux output of CW; Right: 3D modeling – Temperature output of CW

The calculation based on the isothermal plane method equations from NBC yields a more conservative estimate of the R-value compared to the ANSYS simulation. It may be impractical to create 3D models for all wall panels. Therefore, employing simplified hand calculations for panels would streamline the process while still ensuring compliance with the building codes’ thermal performance requirements.

### B.3.2 Thermal Bridges

In this section, the linear and point thermal transmittance are calculated based on the ANSYS simulation results.

#### Expanding Foam

The expanding foam (spray foam) is used to fill any gaps between the horizontal panel joints. The modeling of the horizontal panel joints with only Expanding foam was conducted using ANSYS, the results are shown in Figure B.4. The linear thermal transmittance ( $\Psi$ -value) of the expanding foam is  $-0.009$  W/mK. The expanding foam will provide more thermal resistance for the entire wall assembly, thus the linear thermal transmittance is negative.

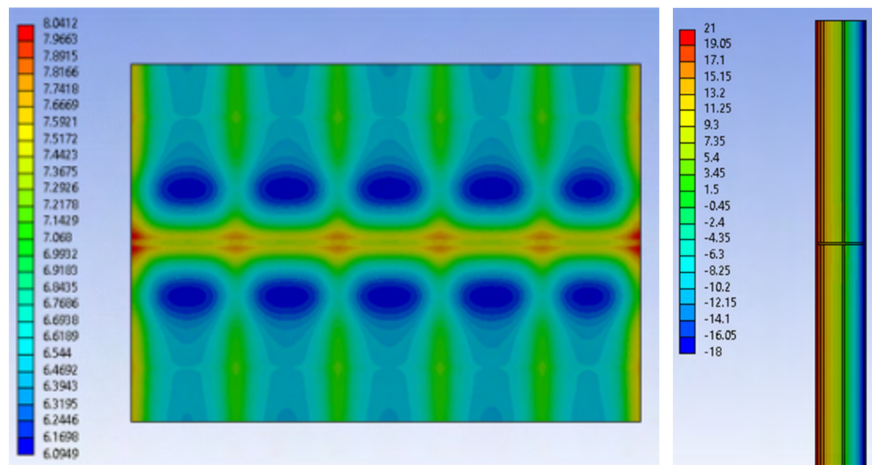


Figure B.4: Left: 3D modeling - Heat flux output of Expanding foam; Right: 3D modeling – Temperature output of Expanding foam

#### Upper Bracket

The horizontal panel joint comprises two upper brackets and expanding foam (spray foam) utilized to fill any gaps between joints. The modeling of the horizontal panel joints was conducted using ANSYS, the corresponding results are presented in Figure B.5. Based on the modeling outcomes, the point thermal transmittance (X-value) of each bracket is determined to be  $0.00034$  W/K. Considering the limited quantity of upper brackets used in the design, the thermal bridge created does not significantly diminish the effective thermal performance of the panel.

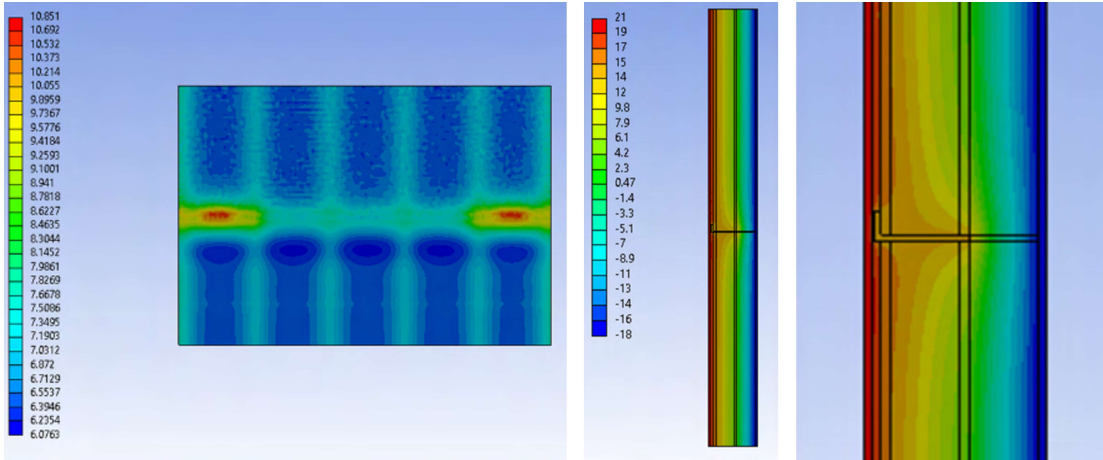
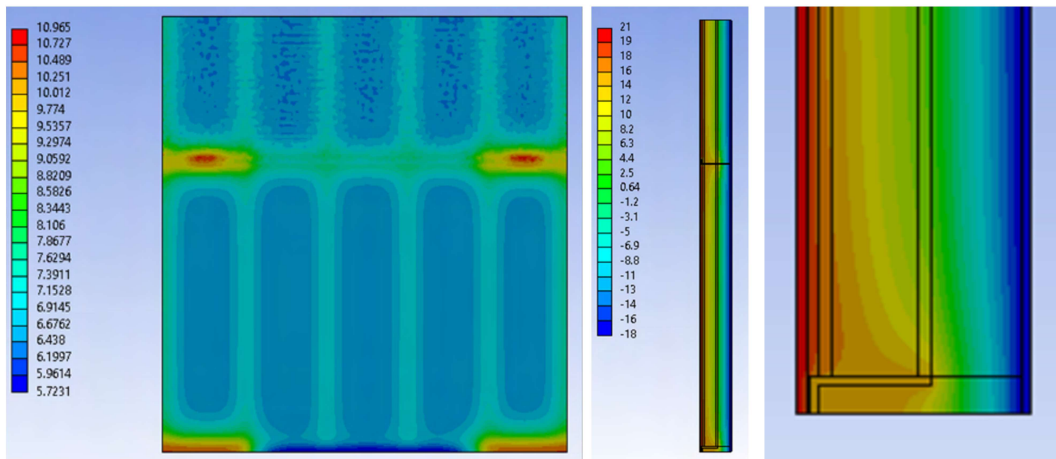


Figure B.5: Left: 3D modeling - Heat flux output of mid-level; Middle: 3D modeling – Temperature output of mid-level; Right: 3D modeling – Temperature output of Upper Bracket  
Detail view

### Bottom Bracket

The bottom brackets provide support to the panel assembly, positioned beneath the first layer of panels. Mineral wool insulation is used to cover gaps present between the bottom brackets and the panel. In ANSYS modeling, an adiabatic boundary condition is applied to the exploded surface of the bottom bracket, indicating that there is no heat transfer into or out of the system. This choice is made due to the current lack of information regarding the exact location of the bottom bracket. According to the ANSYS modeling results, as illustrated in Figure B.6, the X-value for the bottom bracket is determined to be 0.003 W/K. Considering the limited quantity of bottom brackets used in the design, the thermal bridge created does not significantly diminish the effective thermal performance of the panel.



*Figure B.6: Left: 3D modeling - Heat flux output of bottom-level; Middle: 3D modeling – Temperature output of bottom-level; Right: 3D modeling – Temperature output of Bottom Bracket Detail view*

### **B.3.3 Effective Thermal Performance of Proposed Panel**

Considering the clear field thermal performance of the panel and the thermal bridging values, the effective R-value of a 7ft by 10 ft panel section is RSI-5.659 (R-32.14), representing a slight 0.02% reduction compared to the clear field panel assembly RSI-5.660 (R-32.13). Therefore, the impact of the upper and bottom brackets on heat loss is negligible.

### **B.3.4 Dew Point of Proposed Panel**

Assuming an interior side temperature of 21°C and a relative humidity of 50%, the dew point is calculated to be 10.3°C. With the exterior temperature of the wall panel being -18°C, Figure B.7 shows the dew point location in bright yellow, indicating that it occurs within the wood frame area. In most summer conditions, the dew point also tends to occur within the wood frame area. To prevent moisture from permeating through to the wood frame area, a vapor barrier is positioned on the interior side of the wood frame.

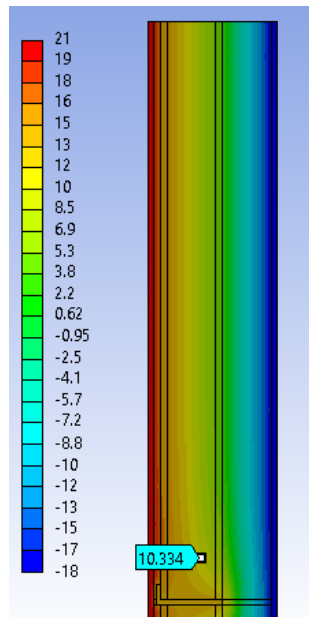


*Figure B.7: Illustration of dew point locations on the mid-level panel*

## Appendix C

This appendix includes the experimental figures not presented in Subsection 2.2.2. It features tests for V-GLITPP method, including Scenario 1 with fiberglass insulation (Figure C.1), as well as Scenario 2.1 (Figure C.2) and Scenario 2.2 (Figure C.3) with mineral wool insulation. Each figure contains eight pictures representing the V-GLITPP method steps: Grasp, Lift, Insert, Tilt, Push and Press, as well as front and back completion views.

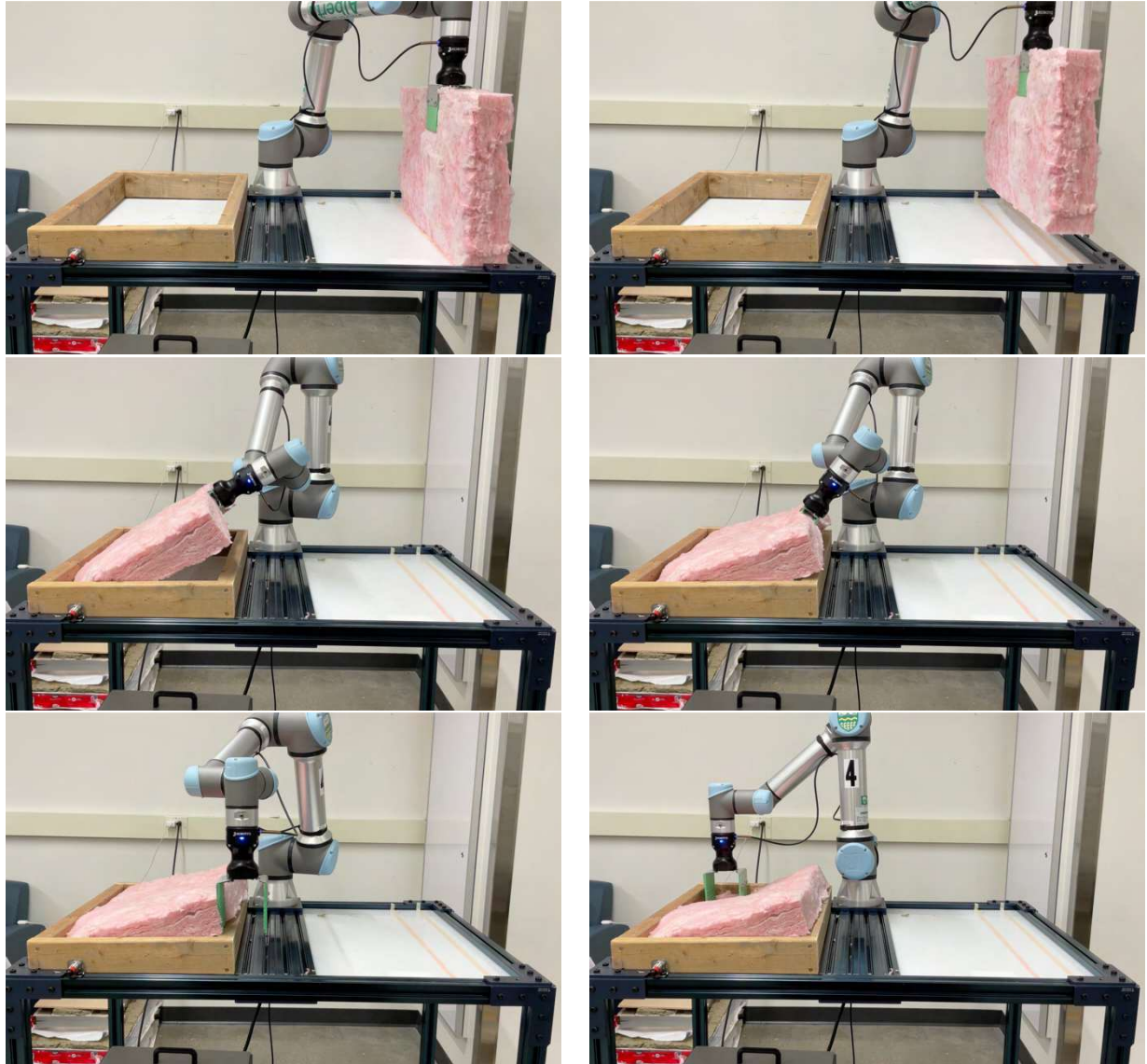




*Figure C.1: V-GLITPP process for Scenario 1 with fiberglass insulation*

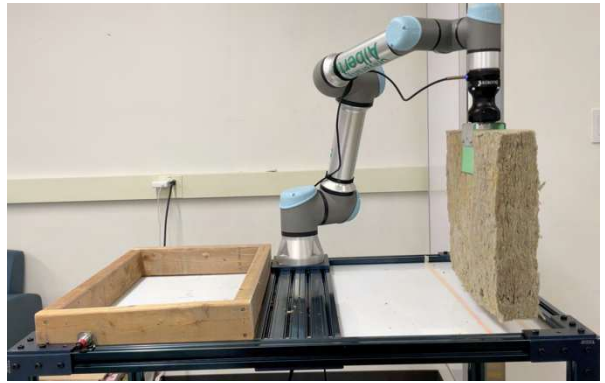
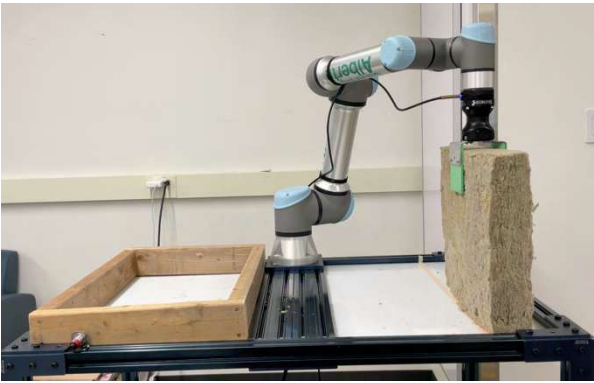




*Figure C.2: V-GLITPP process for Scenario 2.1 with mineral wool insulation*

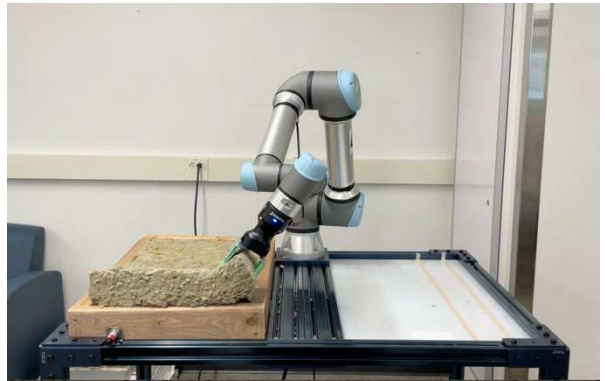




*Figure C.3: V-GLITPP process for Scenario 2.2 with mineral wool insulation*

## Appendix D

This appendix includes the experimental figures not presented in Subsection 3.2.2, featuring the H-GLPPR method. It covers tests with fiberglass and mineral wool insulation in various sizes and scenarios:

- 15 x 3.5-inch (381 x 89 mm): Fiberglass (Scenario 1, Figure D.1; Scenario 2, Figure D.2; Scenario 3, Figure D.3); Mineral wool (Scenario 1, Figure D.4; Scenario 3, Figure D.5)
- 23 x 3.5-inch (584 x 89 mm): Fiberglass (Scenario 1, Figure D.6; Scenario 2, Figure D.7); Mineral wool (Scenario 1, Figure D.8; Scenario 2, Figure D.9; Scenario 3, Figure D.10)
- 15 x 5.5-inch (381 x 140 mm) Fiberglass (Scenario 2, Figure D.11; Scenario 3, Figure D.12); Mineral wool (Scenario 1, Figure D.13; Scenario 2, Figure D.14; Scenario 3, Figure D.15)
- 23 x 5.5-inch (584 x 140 mm) Fiberglass (Scenario 1, Figure D.16; Scenario 2, Figure D.17; Scenario 3, Figure D.18); Mineral wool (Scenario 1, Figure D.19; Scenario 2, Figure D.20; Scenario 3, Figure D.21)

The picture sequences for each scenario follow the H-GLPPR method steps: Grasp, Lift, Place, Press, and Roll. The specific sequences are:

- Scenario 1: Grasp 1st piece, Lift 1st piece, Place 1st piece, Press, Roll, Completion.
- Scenario 2: Grasp 1st piece, Lift 1st piece, Place 1st piece, Grasp 2nd piece, Lift 2nd piece, Place 2nd piece, Press, Roll, Completion.
- Scenario 3: Grasp 1<sup>st</sup> piece, Lift 1<sup>st</sup> piece, Place 1<sup>st</sup> piece, Grasp 2<sup>nd</sup> piece, Lift 2<sup>nd</sup> piece, Place 2<sup>nd</sup> piece, Grasp 3<sup>rd</sup> piece, Lift 3<sup>rd</sup> piece, Place 3<sup>rd</sup> piece, Press, Roll, Completion.

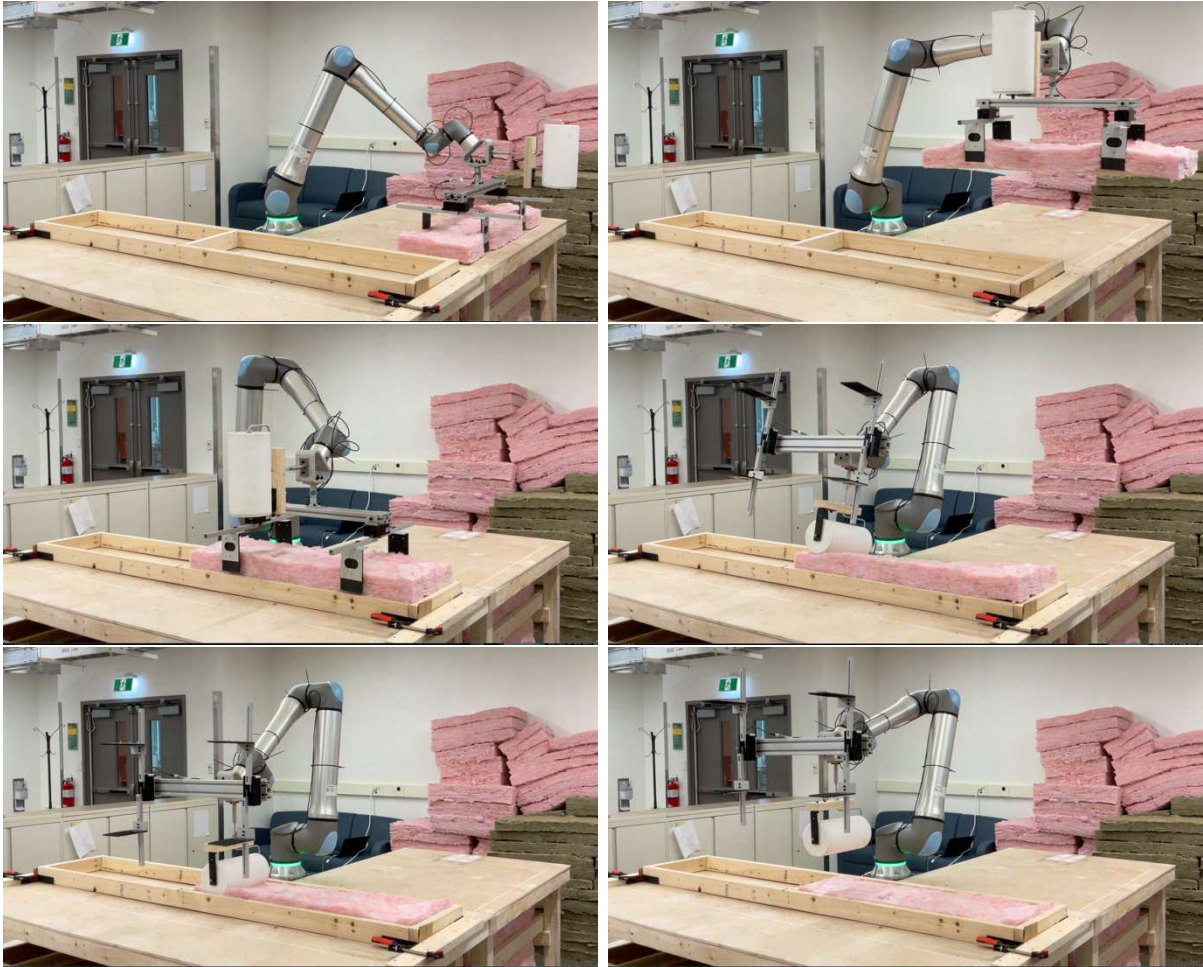


*Figure D.1: H-GLPPR process for Scenario 1 with 15 x 3.5-inch (381 x 89 mm) fiberglass insulation*



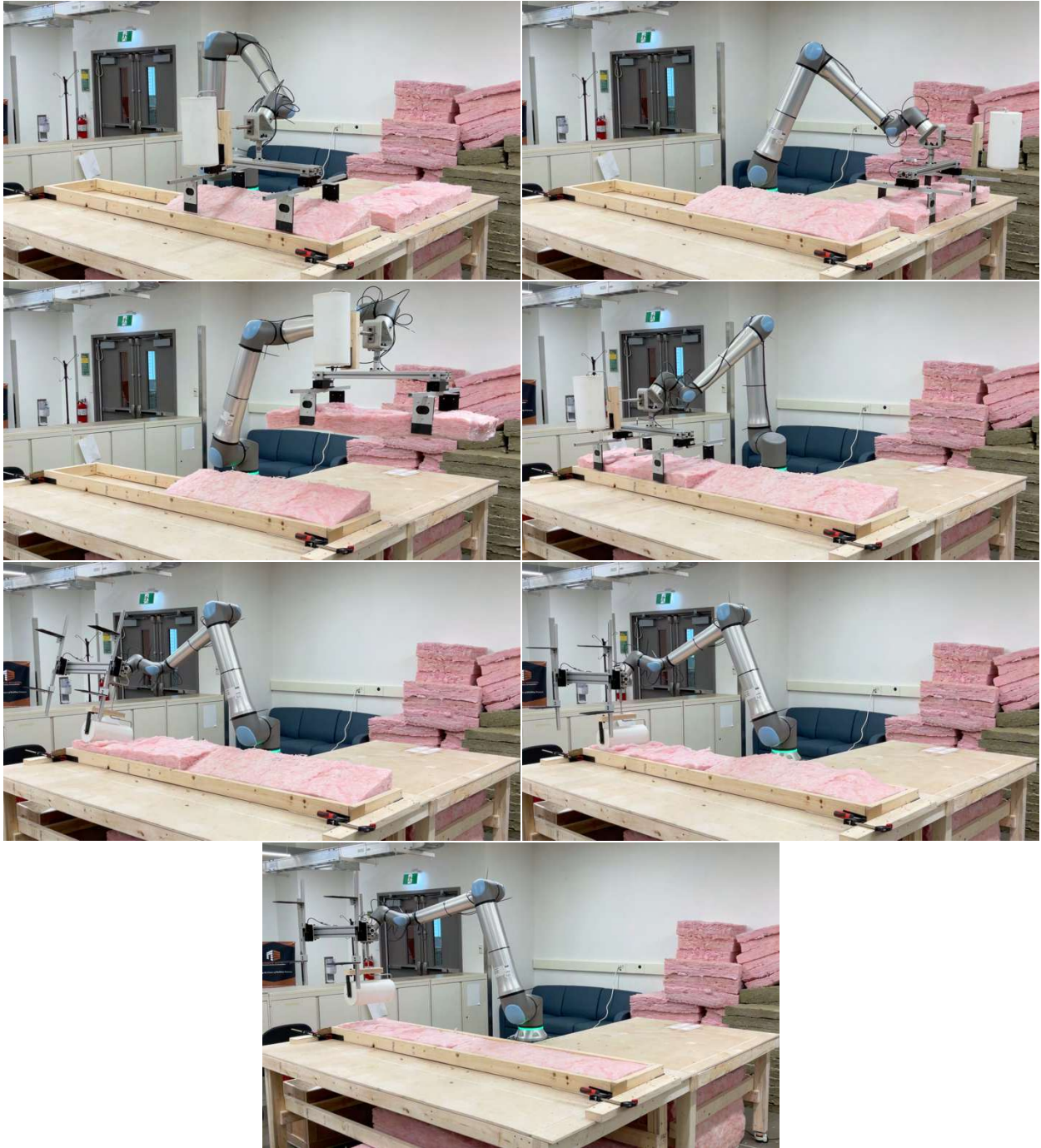


*Figure D.2: H-GLPPR process for Scenario 2 with 15 x 3.5-inch (381 x 89 mm) fiberglass insulation*

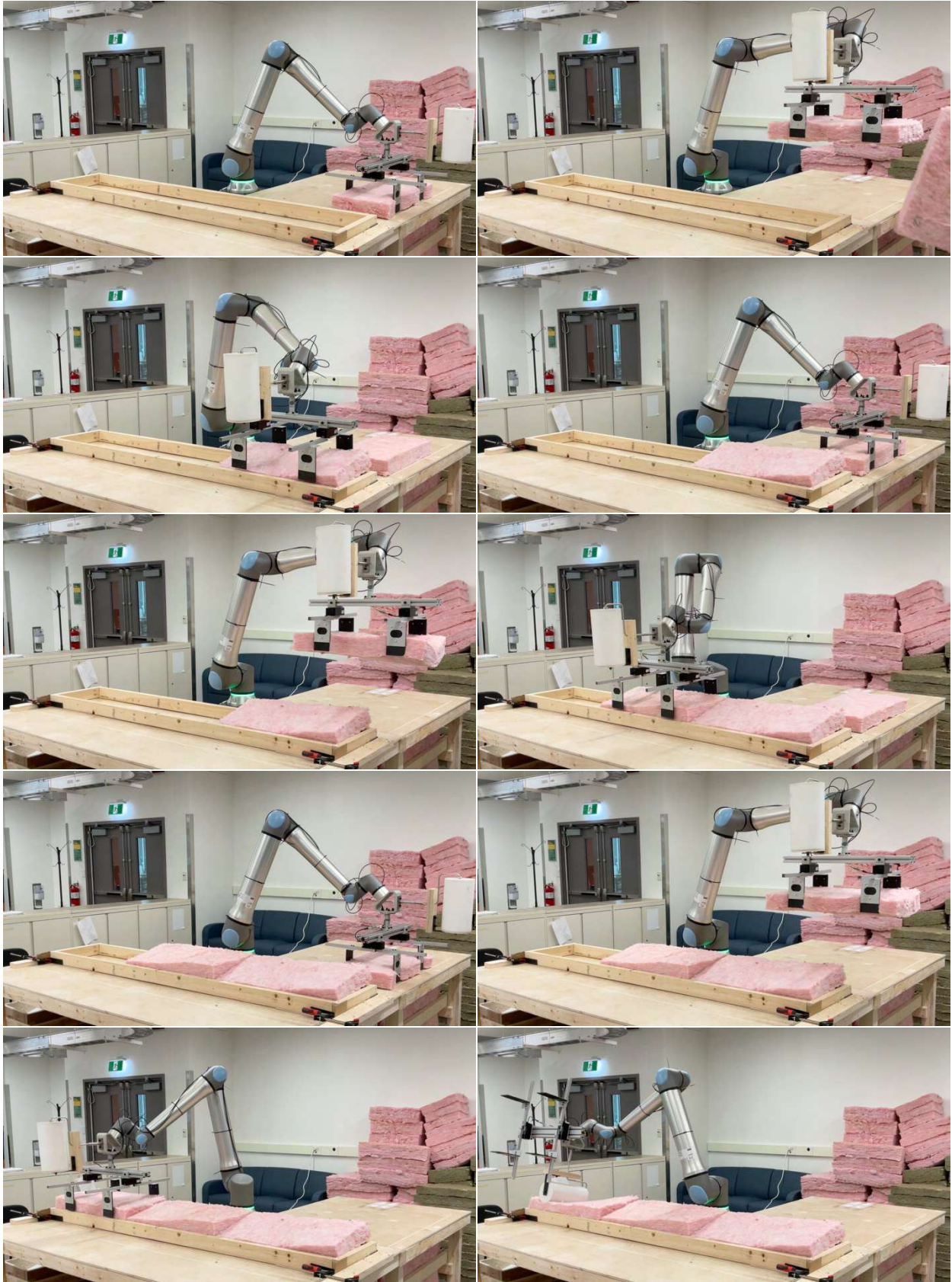




*Figure D.3: H-GLPPR process for Scenario 3 with 15 x 3.5-inch (381 x 89 mm) fiberglass insulation*



*Figure D.4: H-GLPPR process for Scenario 1 with 15 x 3.5-inch (381 x 89 mm) mineral wool insulation*

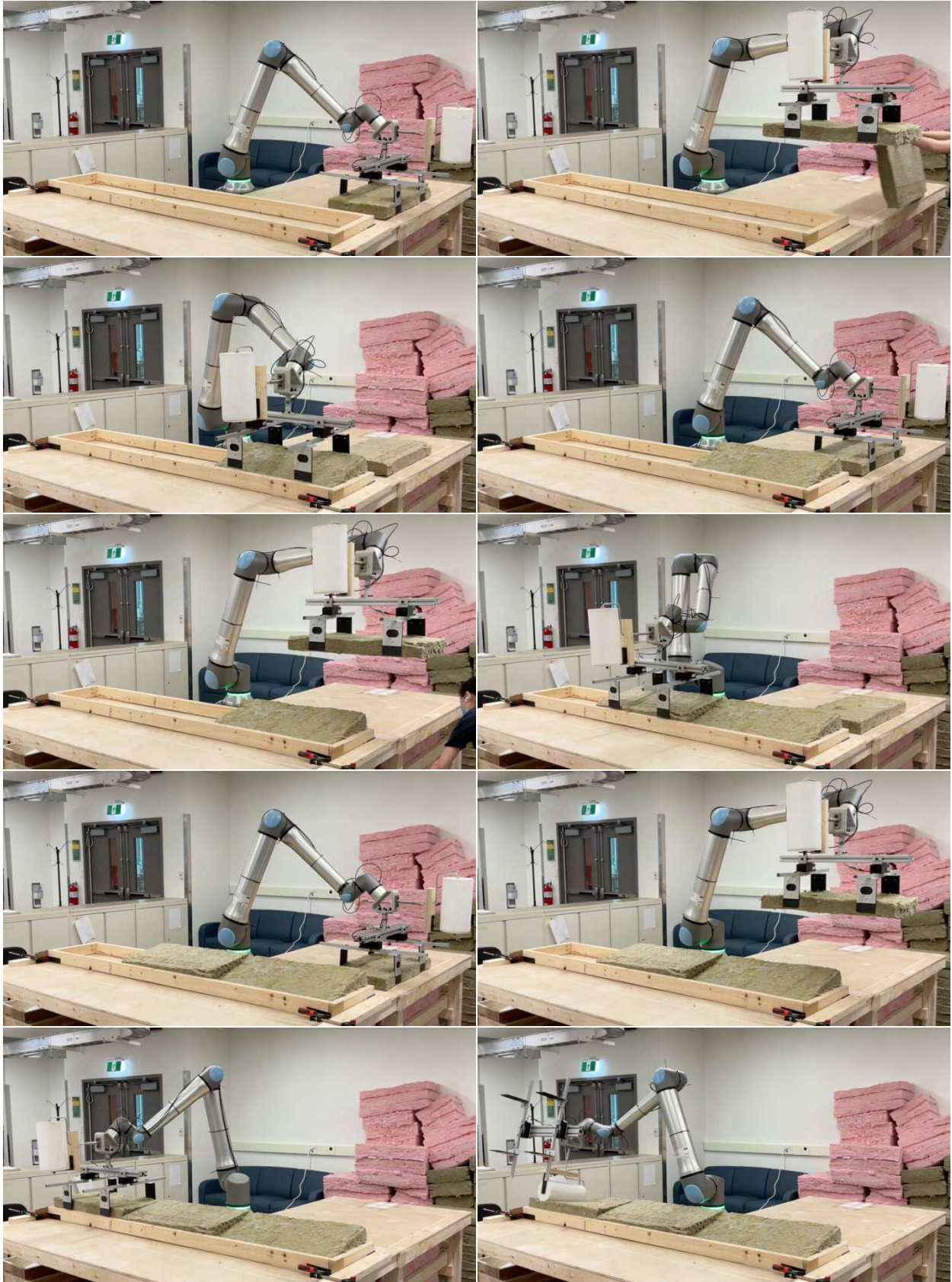




*Figure D.5: H-GLPPR process for Scenario 3 with 15 x 3.5-inch (381 x 89 mm) mineral wool insulation*

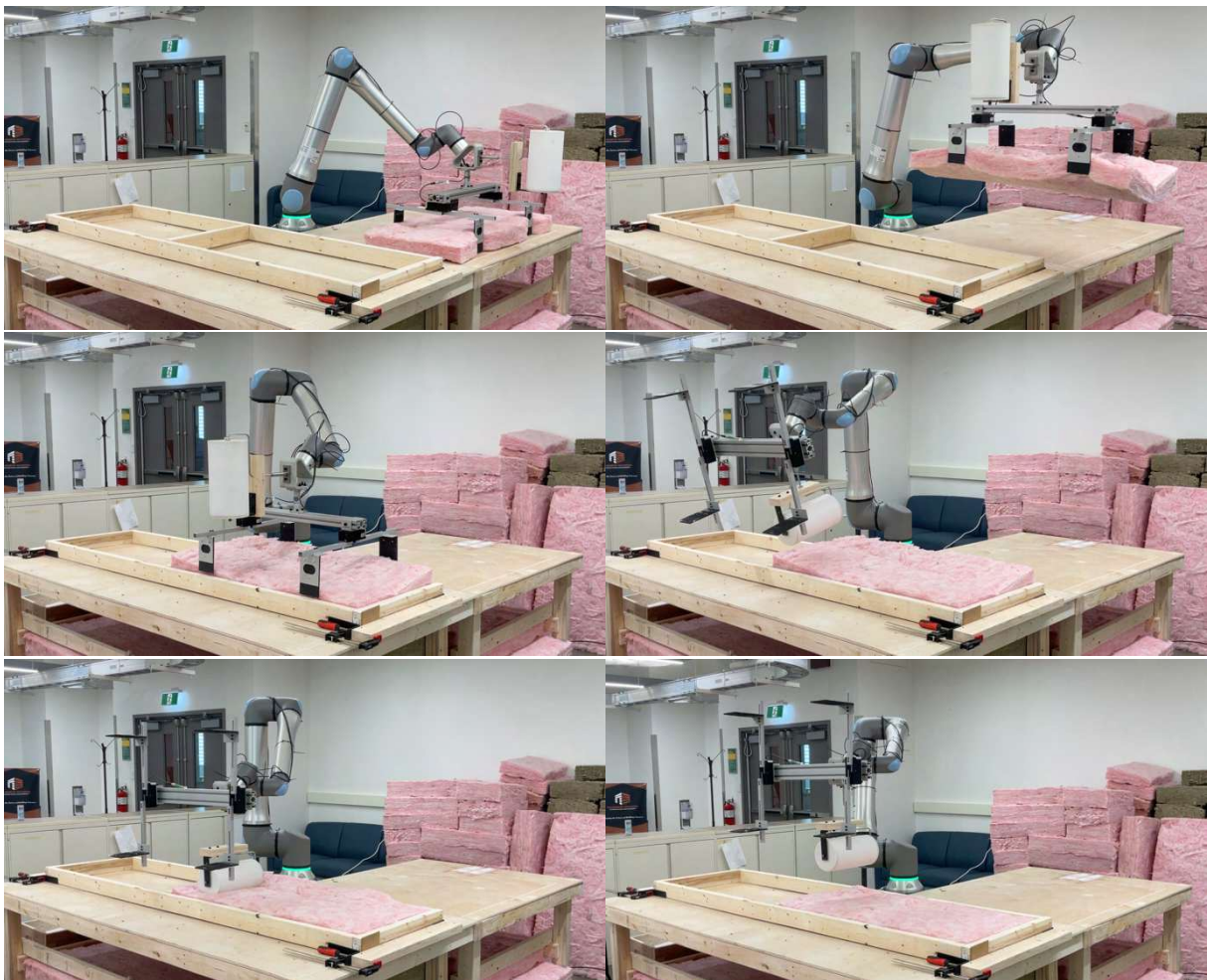


*Figure D.6: H-GLPPR process for Scenario 1 with 23 x 3.5-inch (584 x 89 mm) fiberglass insulation*

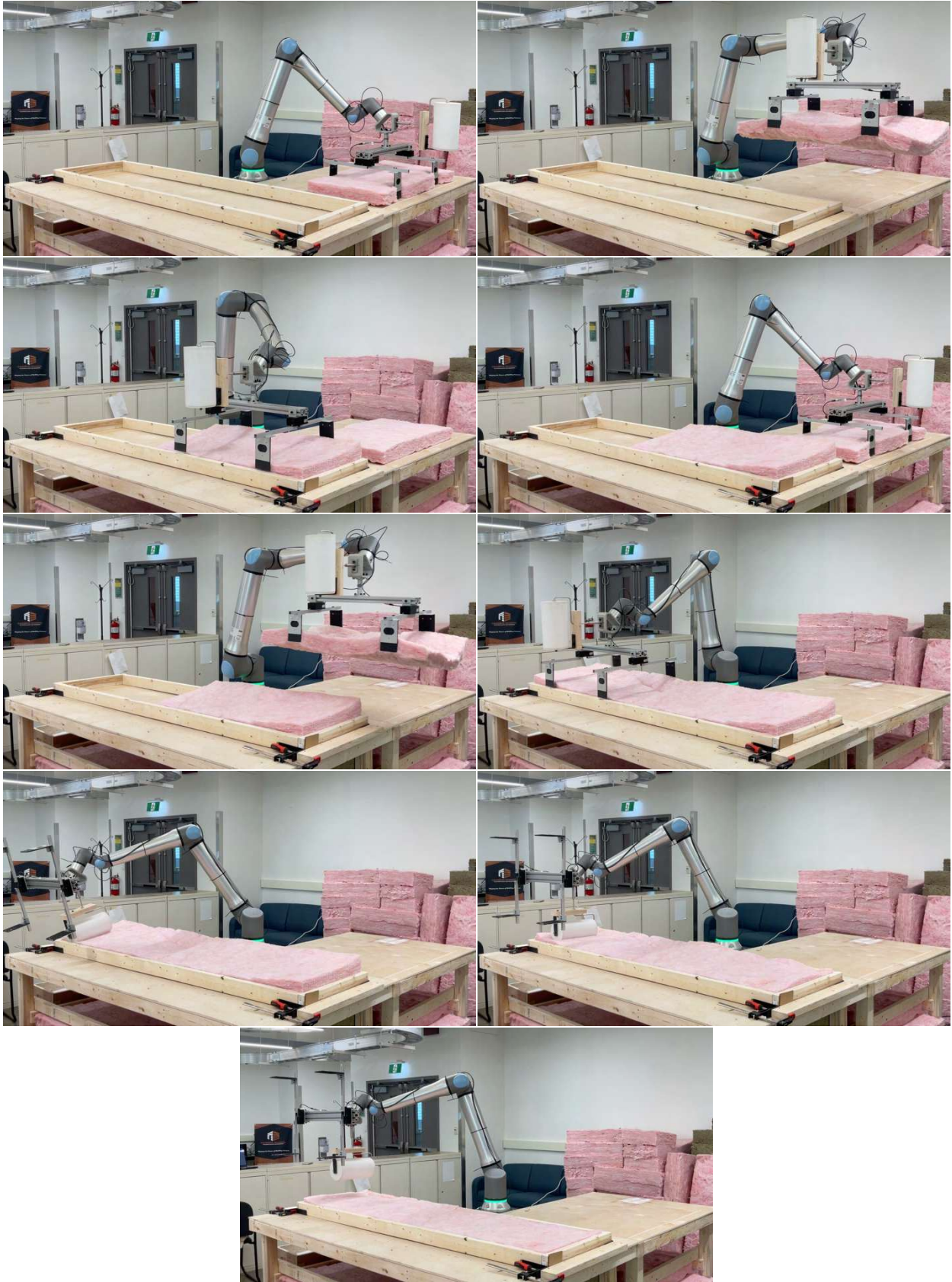


*Figure D.7: H-GLPPR process for Scenario 2 with 23 x 3.5-inch (584 x 89 mm) fiberglass insulation*



*Figure D.8: H-GLPPR process for Scenario 1 with 23 x 3.5-inch (584 x 89 mm) mineral wool insulation*



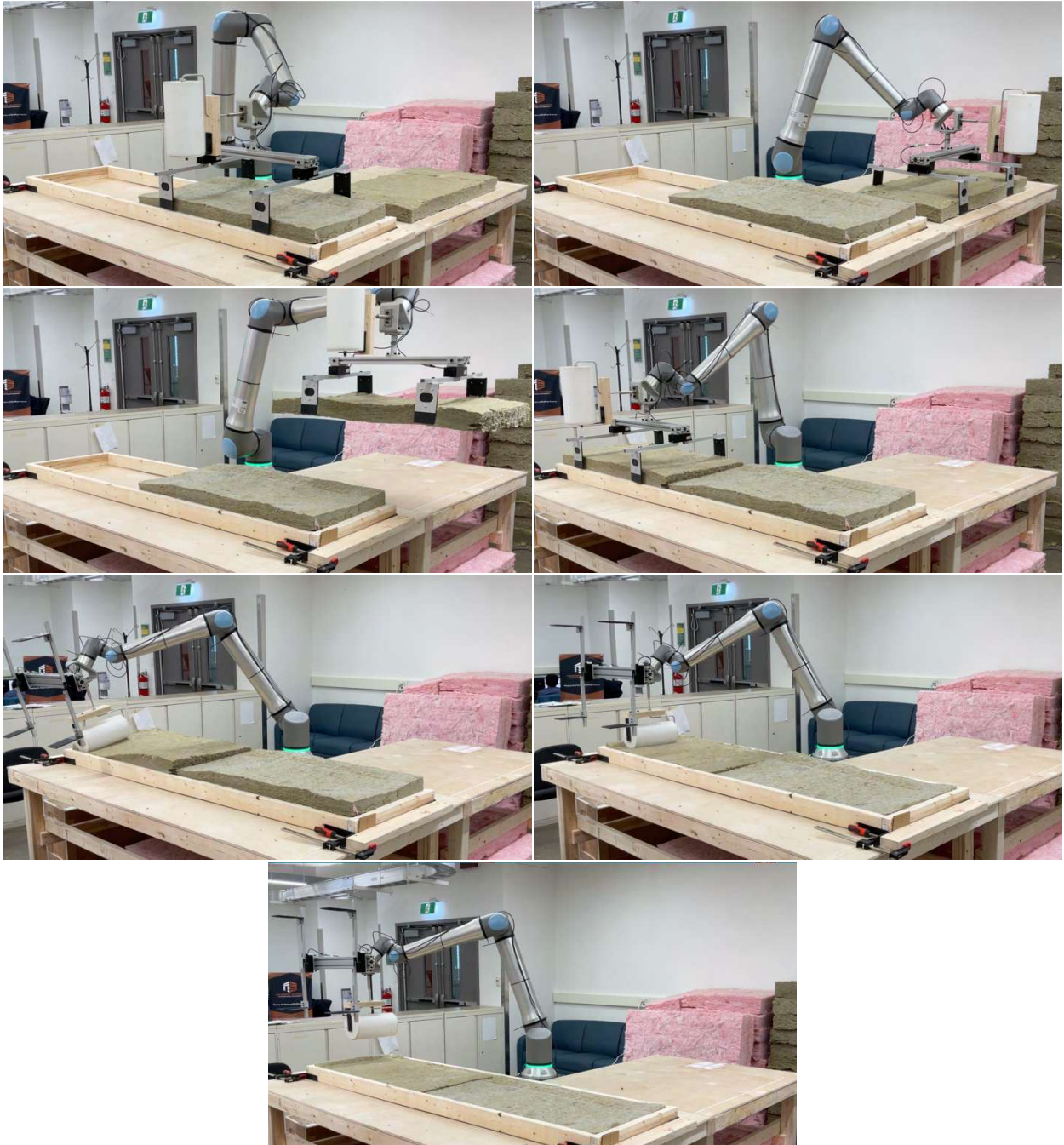
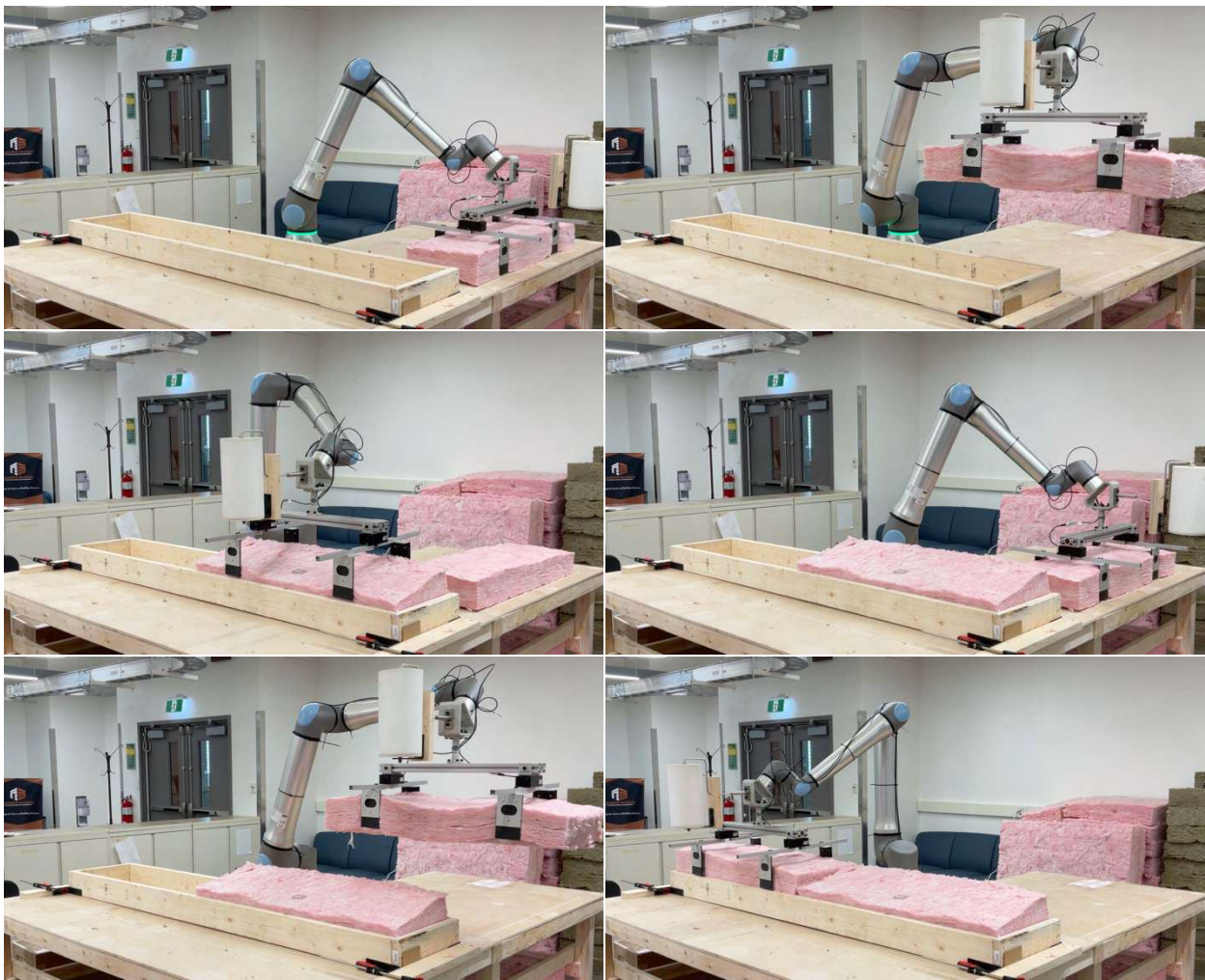


*Figure D.9: H-GLPPR process for Scenario 2 with 23 x 3.5-inch (584 x 89 mm) mineral wool insulation*



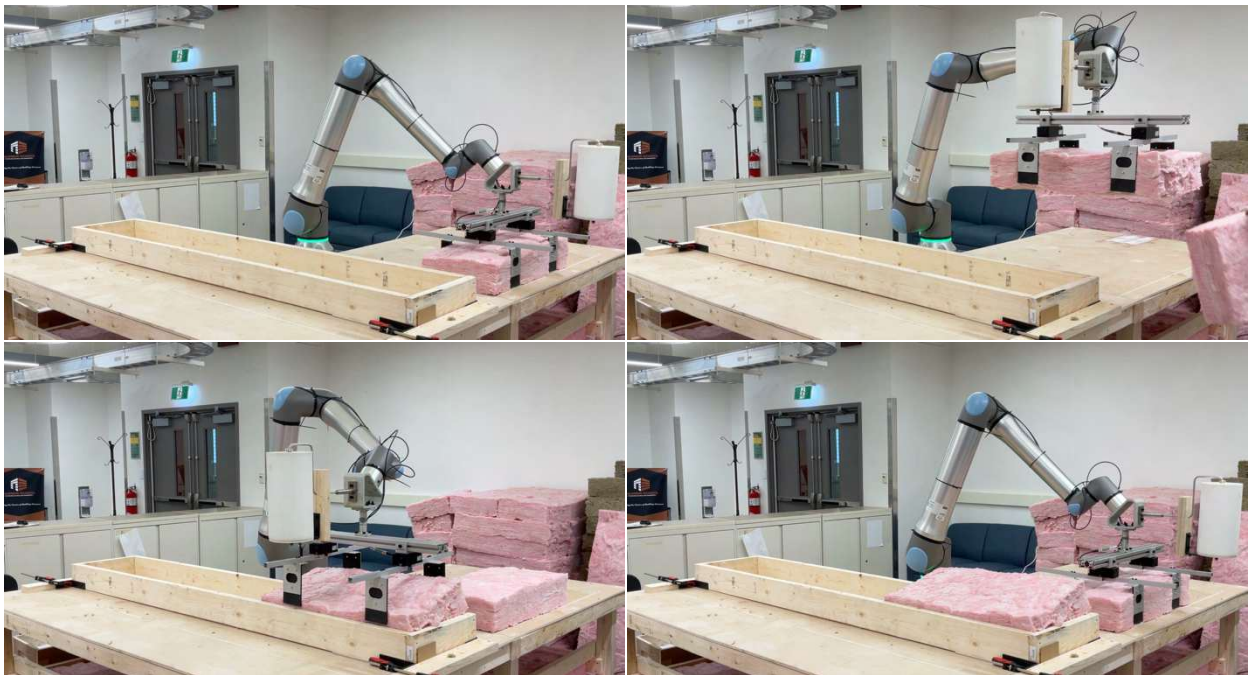


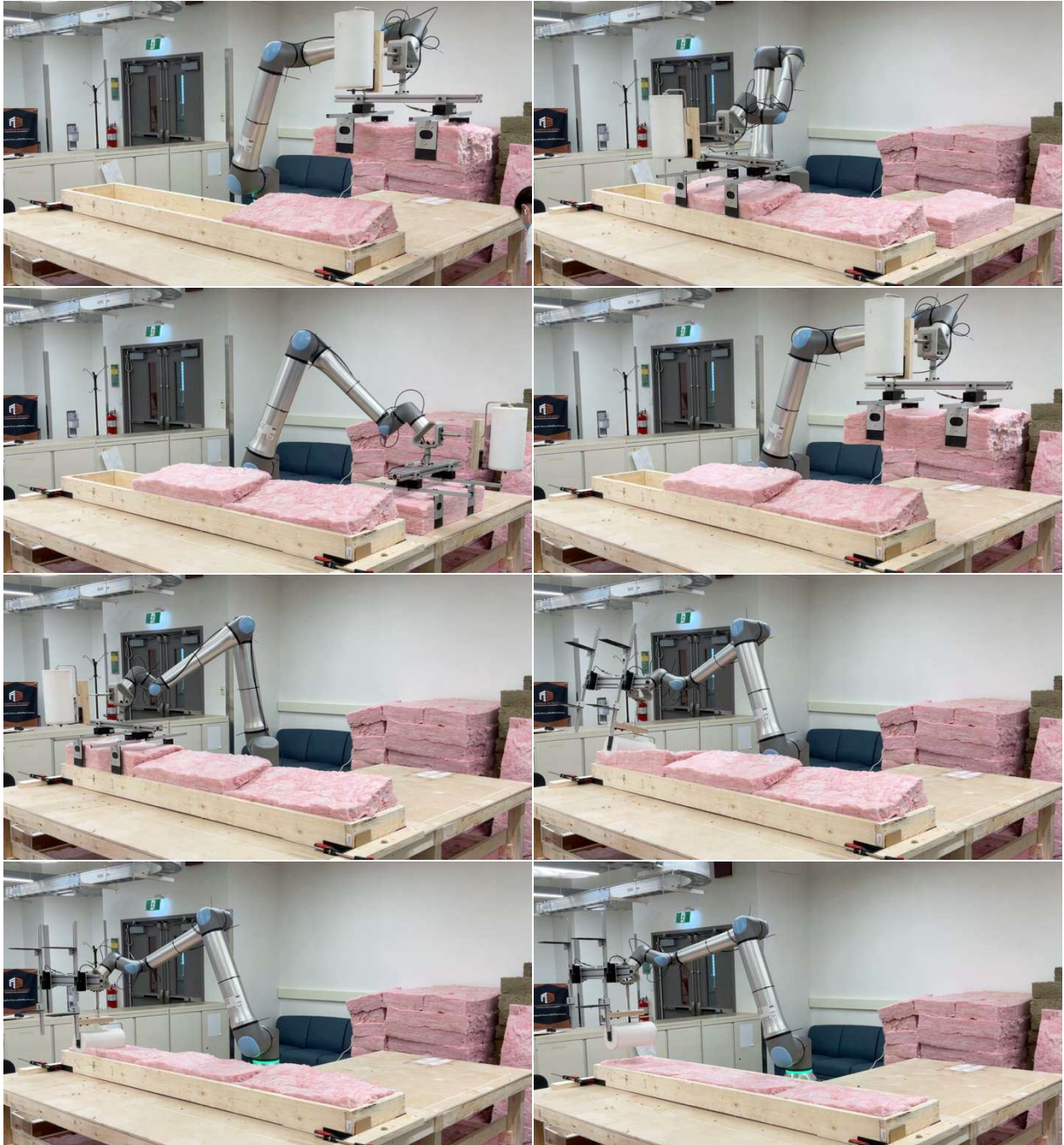
*Figure D.10: H-GLPPR process for Scenario 3 with 23 x 3.5-inch (584 x 89 mm) mineral wool insulation*



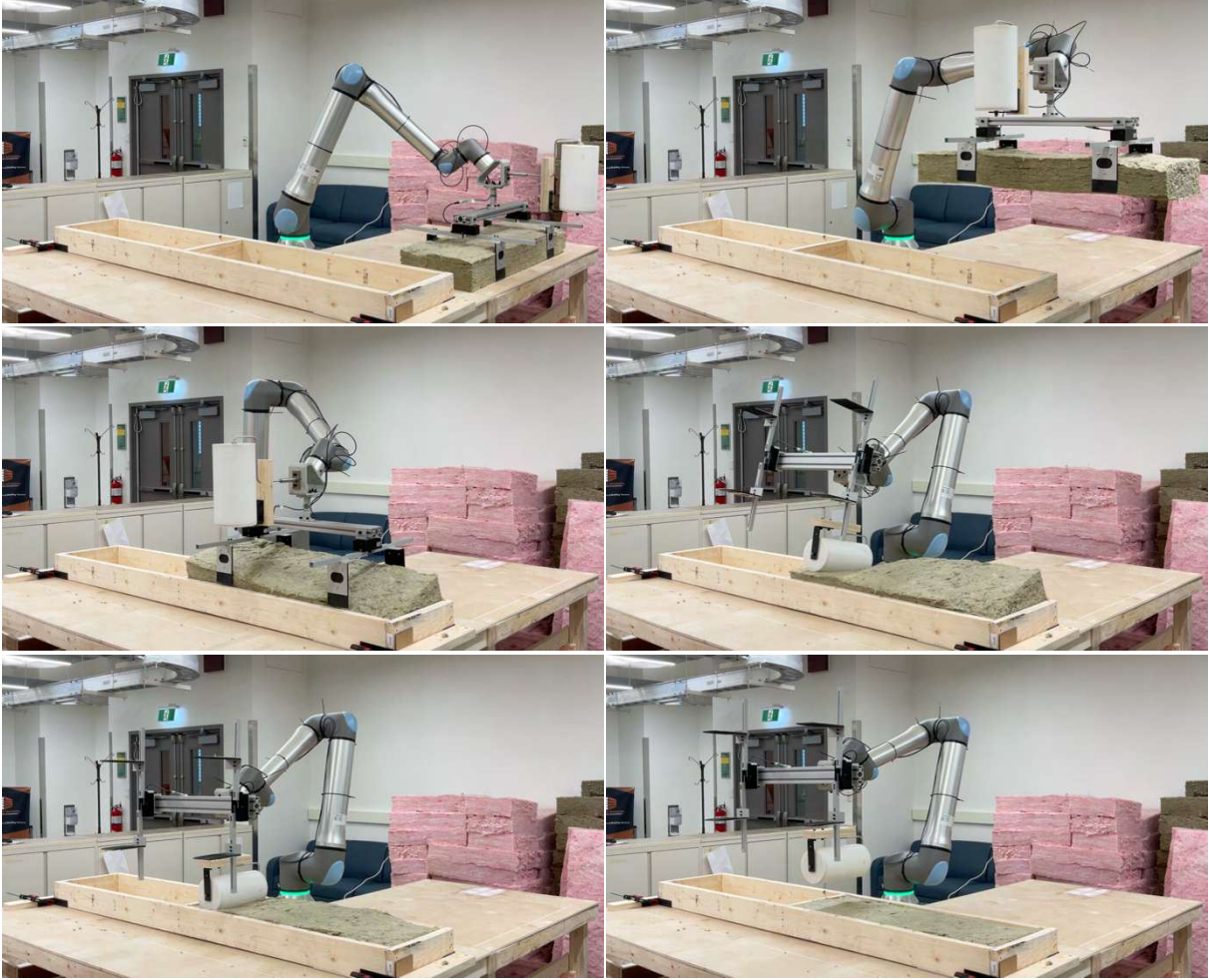


*Figure D.11: H-GLPPR process for Scenario 2 with 15 x 5.5-inch (381 x 140 mm) fiberglass insulation*



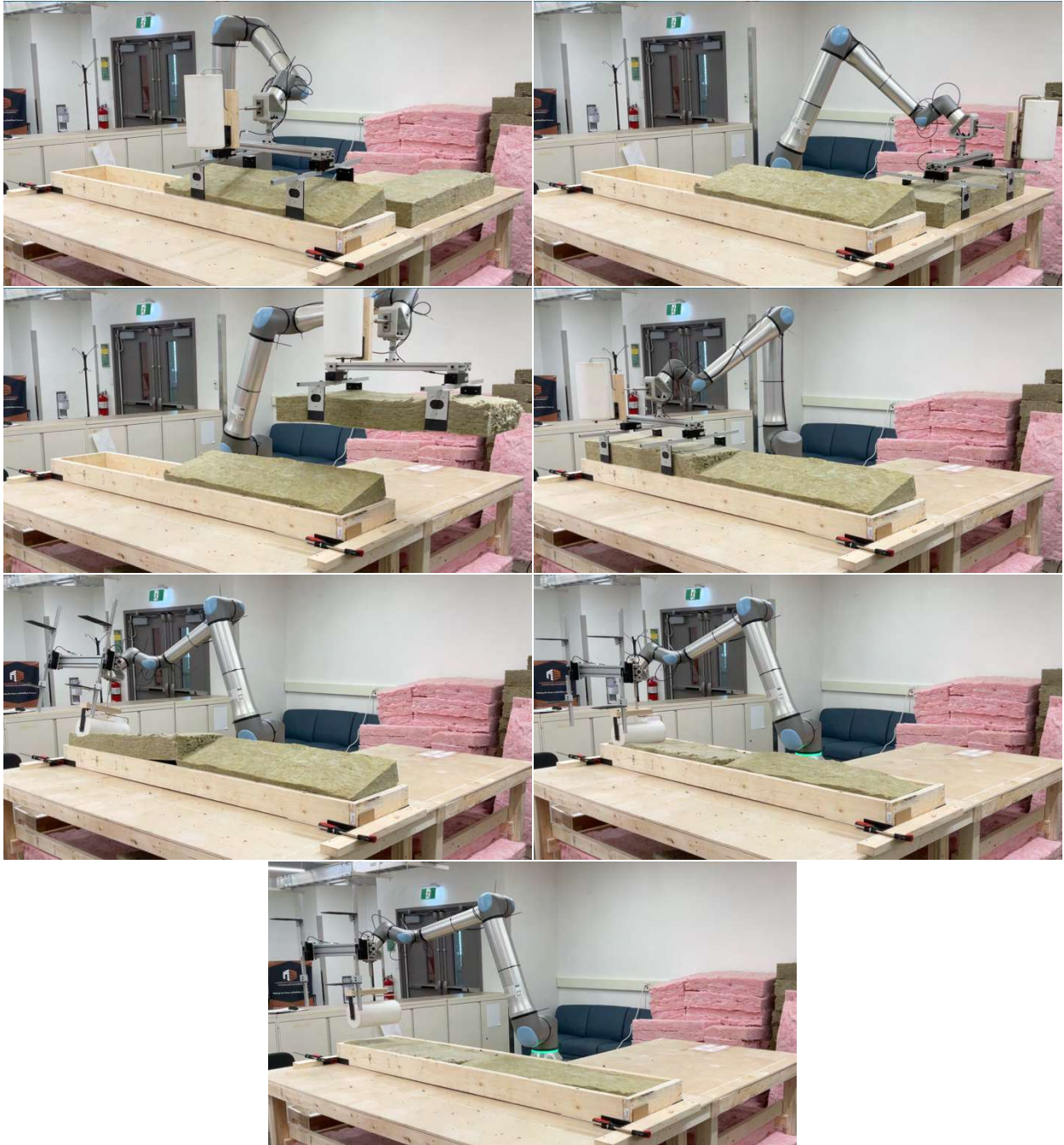


*Figure D.12: H-GLPPR process for Scenario 3 with 15 x 5.5-inch (381 x 140 mm) fiberglass insulation*

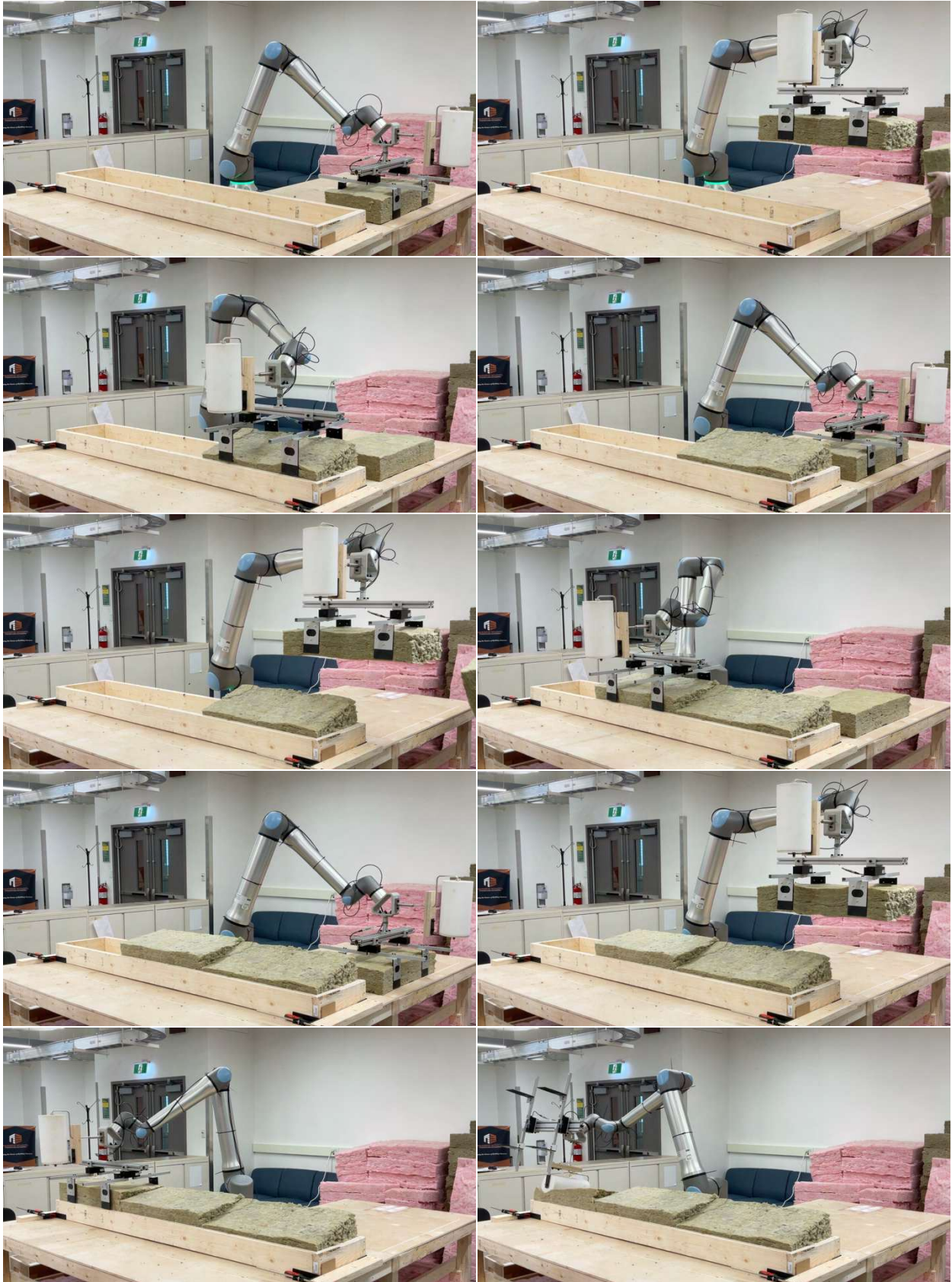


*Figure D.13: H-GLPPR process for Scenario 1 with 15 x 5.5-inch (381 x 140 mm) mineral wool insulation*



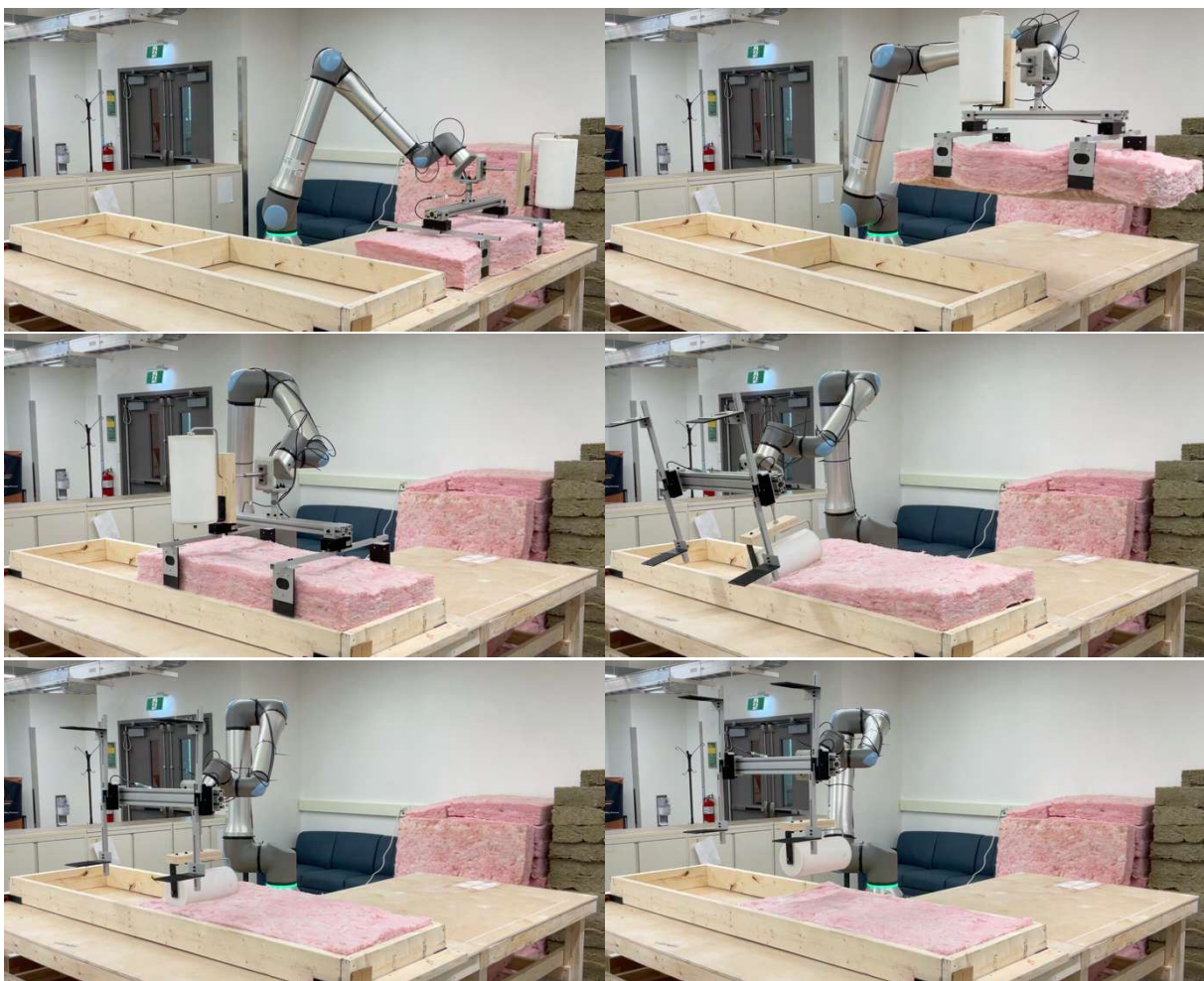


*Figure D.14: H-GLPPR process for Scenario 2 with 15 x 5.5-inch (381 x 140 mm) mineral wool insulation*

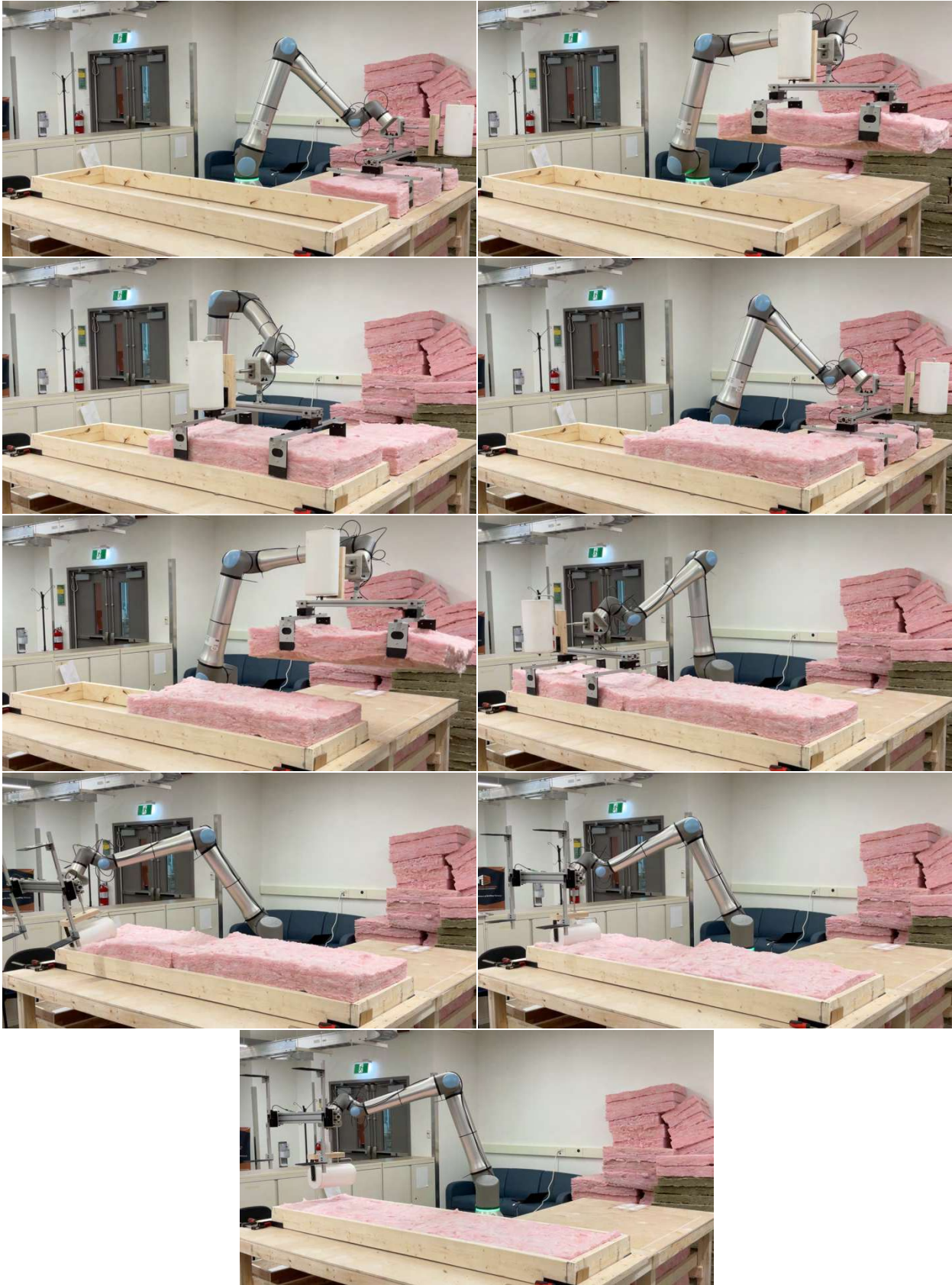




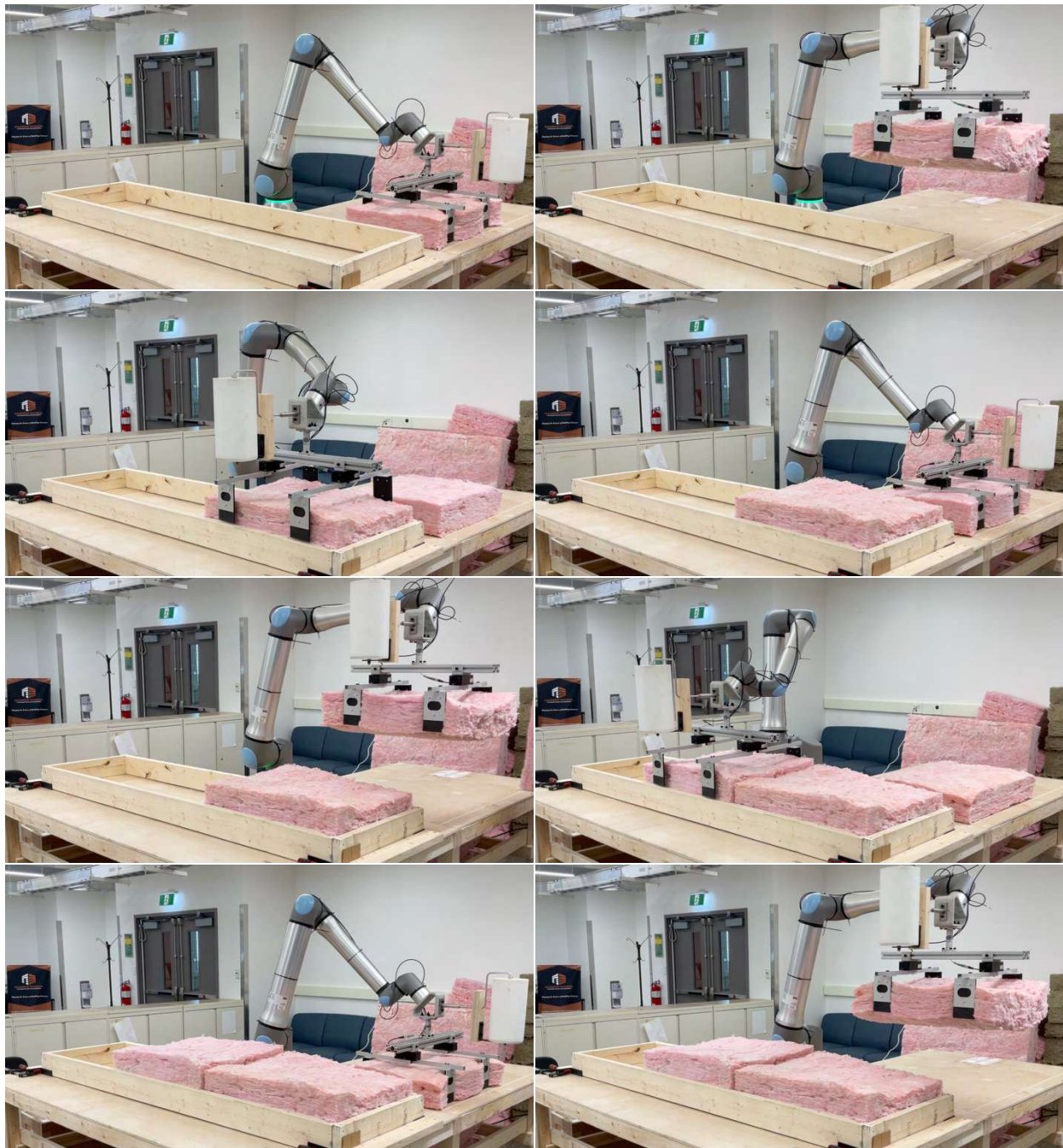
*Figure D.15: H-GLPPR process for Scenario 3 with 15 x 5.5-inch (381 x 140 mm) mineral wool insulation*

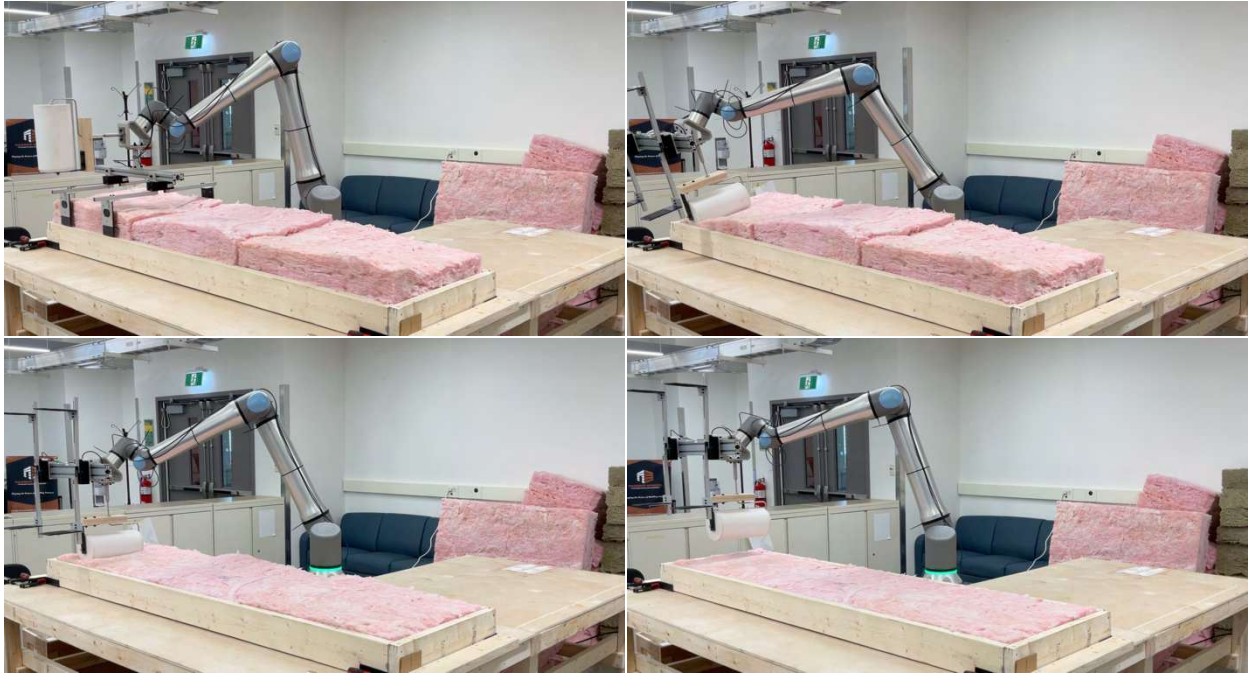


*Figure D.16: H-GLPPR process for Scenario 1 with 23 x 5.5-inch (584 x 140 mm) fiberglass insulation*



*Figure D.17: H-GLPPR process for Scenario 2 with 23 x 5.5-inch (584 x 140 mm) fiberglass insulation*



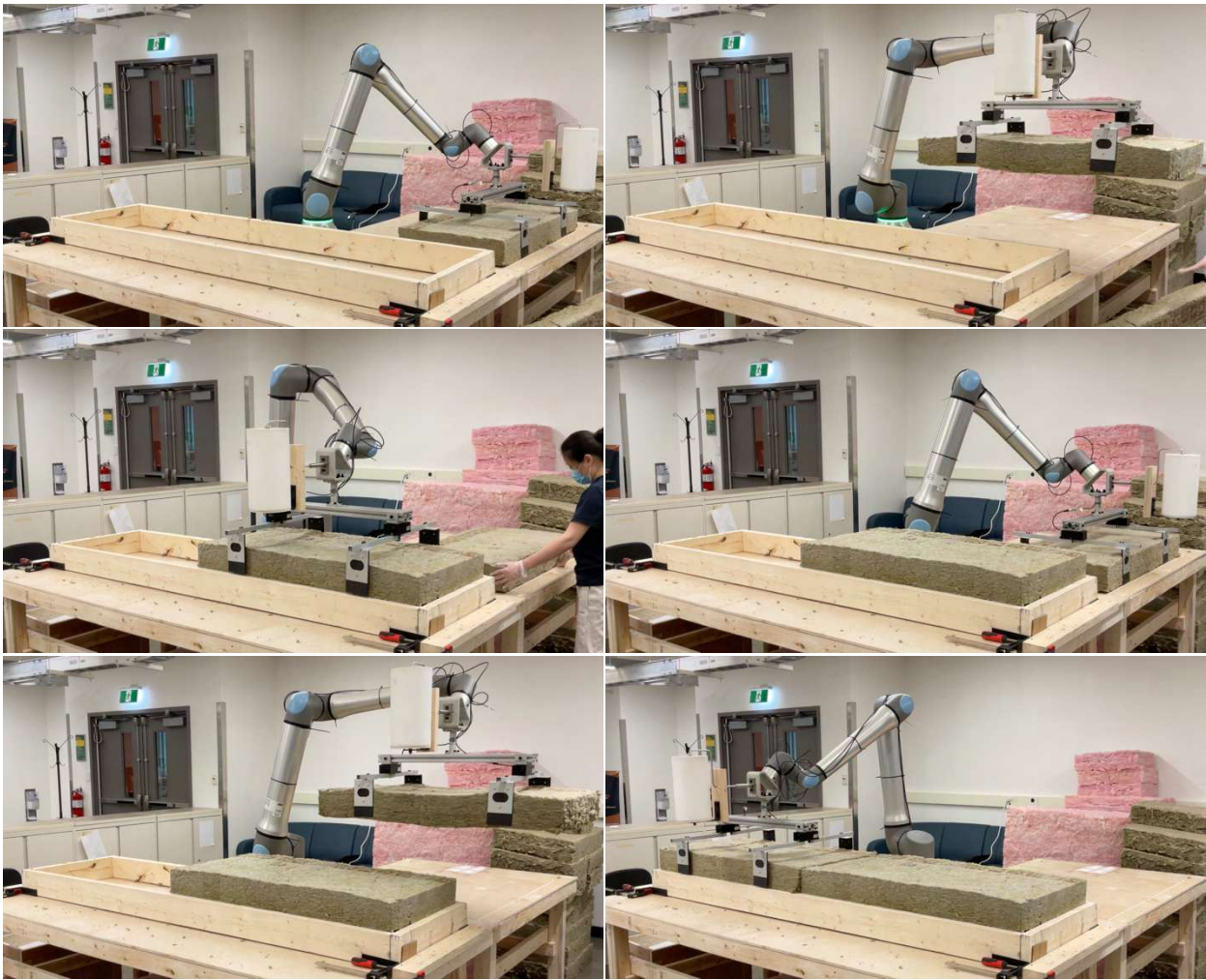


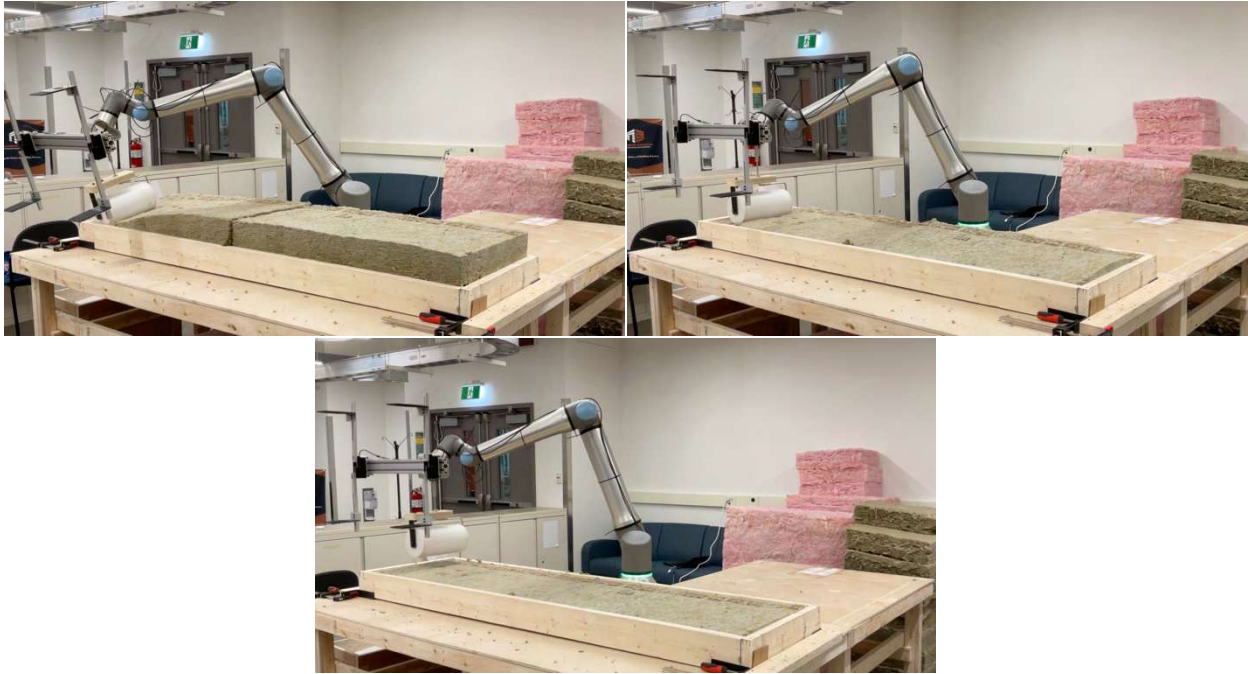
*Figure D.18: H-GLPPR process for Scenario 3 with 23 x 5.5-inch (584 x 140 mm) fiberglass insulation*





Figure D.19: H-GLPPR process for Scenario 1 with 23 x 5.5-inch (584 x 140 mm) mineral wool insulation





*Figure D.20: H-GLPPR process for Scenario 2 with 23 x 5.5-inch (584 x 140 mm) mineral wool insulation*





*Figure D.21: H-GLPPR process for Scenario 3 with 23 x 5.5-inch (584 x 140 mm) fiberglass insulation*